ANALYSIS OF A SPATIALLY-DISTRIBUTED WILSON-COWAN MODEL OF CORTEX

by

Jeremy D Harris

BS in Mathematics, University of Pittsburgh, 2011

Submitted to the Graduate Faculty of

the Kenneth P. Dietrich School of Arts and Sciences in partial

fulfillment

of the requirements for the degree of

Doctor of Philosophy

University of Pittsburgh

2017

UNIVERSITY OF PITTSBURGH

KENNETH P. DIETRICH SCHOOL OF ARTS AND SCIENCES

This dissertation was presented

by

Jeremy D Harris

It was defended on

April 13, 2017

and approved by

G. Bard Ermentrout, Distinguished University Professor, Mathematics

Jonathan Rubin, Professor, Co-undergraduate Director, Mathematics

Brent Doiron, Associate Professor, Mathematics

Nathan Urban, Professor and Vice Chair of Neurobiology

Dissertation Director: G. Bard Ermentrout, Distinguished University Professor, Mathematics

ANALYSIS OF A SPATIALLY-DISTRIBUTED WILSON-COWAN MODEL OF CORTEX

Jeremy D Harris, PhD

University of Pittsburgh, 2017

The Wilson-Cowan equations represent a model for the mean activities of localized excitatory and inhibitory populations in sensory cortex. In this document, we extend this model to include spatially-distributed connections in a 1D continuum model to study spatio-temporal patterns, such as traveling waves and doubly periodic patterns. We use bifurcation theory and continuation methods to understand how these organized patterns of activity arise in the network. In addition, we often simulate a (spatial) discretization of the network (to approximate the continuum) and compare these with our analytical theory to give evidence as to how these patterns may become unstable. In the later chapters, we make comparisons with a nonsmooth version of the model to understand the consequences of this approximation.

TABLE OF CONTENTS

LIST OF TABLES

LIST OF FIGURES

1.0 INTRODUCTION

1.1 THE FIRING RATE MODEL

In 1972, Wilson and Cowan derived a pair of nonlinear differential equations to model the mean activities of localized interacting excitatory and inhibitory neuronal populations [76]. They utilize a well-accepted law, known as Dale's principle, which states that an individual neuron in a population is excitatory (inhibitory) if when the cell spikes, it increases (decreases) the voltage potential of the post synaptic cells that it synapses onto. Hence, local populations of neurons may be separated into two subpopulations, excitatory and inhibitory, which is often a starting point of neuronal models. Wilson and Cowan suggest that the resulting excitatory-inhibitory circuit represents the mean statistics of some underlying random process in a localized region of cortex [76]. For our purposes, this system is the minimal model that captures some of the important features for studying traveling waves and spatio-temporal pattern formation in the spatially-extended continuum model.

Before we begin our discussion of the Wilson-Cowan (WC) model, we briefly describe the heuristic derivation of a general neuronal network model given by Ermentrout in [17, 19]. Consider a network in which the ith population has an average firing rate, $U_i(t)$, which is a function of membrane potential, $V_i(t)$ and writes $U_i(t) = F_i(V_i(t))$, where F_i is the population response function, which the authors of [17] refer to as the firing rate function. By making assumptions on the shape of the post synaptic potential and temporal properties of the membrane potentials, [17, 19] arrive at the first order dynamics of the activity-based model given by

$$\tau_i \frac{dU_i}{dt} + U_i = F_i\left(\sum_j a_{ij}\, U_j(t - \delta_{ij})\right) ,$$

where $U_i(t)$ are the average firing rates; a_{ij} are the average connection strengths from population j to population i; and δ_{ij} represent temporal delays due to the signal traveling down the axon. In [17], the authors refer to this set of equations as the rate model, though it is worth mentioning that $F_i\left(\sum_j a_{ij}U_j(t-\delta_{ij})\right)$ is the actual firing rate as a function of the synaptic drive. We will consider a simplified firing rate model by setting the delays, δ_{ij}, to zero.

Thus far, we have not mentioned the shape of the firing rate function, but there have been many derivations of the firing rate function which show that under certain assumptions it is monotonically increasing from 0 to 1 and has a sigmoidal shape, as in Fig. 1A. Although the specific firing rate function depends on the temporal variability within the network, we begin with a mean field theory which uses the logistic function:

$$F(u) = \frac{1}{(1+\exp(-\beta\, u))}\ ,$$

where β is the gain parameter that modulates the steepness of the curve. In Fig. 1A, we show the firing rate function for increasing values of the gain parameter, β; we note that as β increases, the firing rate function limits to the Heaviside step function, which will be relevant when we consider the nonsmooth system in Chapters 4 and 5. The reason for this choice of firing rate function is that there are several useful properties of the logistic function which we will use throughout our analysis.

Before introducing the excitatory-inhibitory system, we mention some of the previous phase plane results on the behavior of the two population firing rate model (not necessarily excitatory-inhibitory) given by

$$\begin{aligned}
\tau_1\frac{dU_1}{dt} &= -U_1 + F\left(a_{11}\,U_1 + a_{12}\,U_2 - \theta_1\right)\\
\tau_2\frac{dU_2}{dt} &= -U_2 + F\left(a_{21}\,U_1 + a_{22}\,U_2 - \theta_2\right)\ .
\end{aligned}$$

These equations have been the subject of a great deal of analysis, including an in-depth study by Beer [2] of the phase plane dynamics based on the different connectivity configurations of a_{jk} for $j,\, k \in \{1,2\}$. It was shown in Chapter 3 of [19] that if $a_{11}, a_{21} > 0$ and $a_{12} > 0$, then there can be no limit cycles in the system. Hence, when there is no negative feedback, limit cycles are impossible, which intuitively makes sense, since there is no mechanism to "turn

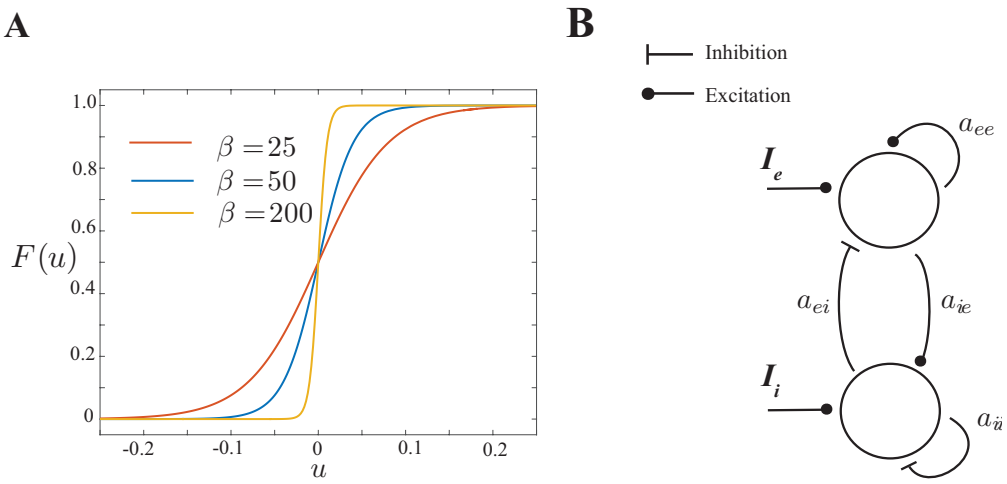

Figure 1: The firing rate function and connectivity diagram. (A) The sigmoidal firing rate function with increasing gain parameter: $\beta = [25, 50, 200]$. (B) The connectivity diagram for localized interacting excitatory-inhibitory populations.

off" activation. In addition to Beer's list, [19] considers the system in which the connection strengths satisfy: $a_{21}, a_{11} \geq 0$ $(a_{12}, a_{22} \leq 0)$. This corresponds to the excitatory-inhibitory system which is the case that is relevant to our study. Hence, we "hard code" the signs into the inhibitory connections so that all connection strengths, a_{kj} for k, $j \in \{e, i\}$, are positive and adopt the notation, $U_1 = u$ for excitation and $U_2 = v$ for inhibition.

1.2 THE EXCITATORY-INHIBITORY SYSTEM

Now that we have a general understanding of the firing rate model, we consider a model of interacting excitatory and inhibitory populations given by

$$\begin{aligned} u' &= -u + F(I_e + a_{ee}\, u - a_{ei}\, v - \theta_e) \\ \tau\, v' &= -v + F(I_i + a_{ie}\, u - a_{ii}\, v - \theta_i)\ , \end{aligned} \tag{1.1}$$

where $' = \frac{d}{dt}$ and $\tau = \tau_i/\tau_e$ is the relative time-scale of inhibition to excitation, θ_e and θ_i are

the thresholds, and I_e and I_i are the external inputs to the excitatory and inhibitory populations, respectively. In Fig. 1, we show the connectivity diagram for the localized excitatory and inhibitory populations. Since we can absorb constant inputs into the thresholds, θ_e and θ_i, we set $I_i = I_e = 0$. The nullcline structure and the phase plane will be discussed in more detail in the coming sections.

1.3 THE PHASE PLANE AND EQUILIBRIA

Next we study the phase plane of excitatory-inhibitory system in Eq. (1.1), which we will refer to in later Chapters as the "space-clamped" system. In our setup, we first consider a set of parameters so that there are three equilibria: $E_d := (\bar{u}_d, \bar{v}_d)$ is the down state; $E_s := (\bar{u}_s, \bar{v}_s)$ is a saddle point; and $E_m := (\bar{u}_m, \bar{v}_m)$, the up state. In the next section we will discuss in more detail the properties of the up state, which represents the active state of cortex. Neuroscience theorists often refer to this state as the inhibitory stabilized network (ISN) state [57, 74], since runaway activity in the excitatory population is prevented by strong inhibitory feedback. For the parameters of interest, the ISN will exist independent of whether there is a down state or saddle point. In Fig. 2A,B, we show the nullclines of the excitatory-inhibitory system in (1.1), which satisfy

$$\begin{aligned} (u\text{-nullcline}) \quad & 0 = -u + F(a_{ee}\, u - a_{ei}\, v - \theta_e) \\ (v\text{-nullcline}) \quad & 0 = -v + F(a_{ie}\, u - a_{ii}\, v - \theta_i)\ . \end{aligned} \tag{1.2}$$

The stability of the equilibria, $(\bar{u}, \bar{v})$, can be determined by looking at the linearization of (1.1) about each of them, which is given by the matrix,

$$A_0 = \begin{pmatrix} -1 + b_{ee} & -b_{ei} \\ b_{ie}/\tau & -(1 + b_{ii})/\tau \end{pmatrix}.$$

Here $b_{jk} = a_{jk} F'(a_{je}\bar{u} - a_{ji}\bar{v} - \theta_j)$ for $j, k \in \{e, i\}$, and since $F'(u) > 0$, then $b_{jk} > 0$. We

write the trace and determinant of A_0 as

$$T_0 = -1 + b_{ee} - (1 + b_{ii})/\tau$$
$$D_0 = \frac{1}{\tau}\left((1 - b_{ee})\,(1 + b_{ii}) + b_{ei}\,b_{ie}\right).$$

By knowing the sign of the derivative of the u-nullcline at the equilibria, we can deduce the sign of the trace and determinant to assess the stability of the different steady-states. We see from Fig. 2A that for the down state, E_d, the u-nullcline (orange) has negative slope. Hence, $\frac{-1+b_{ee}}{b_{ei}} < 0$, which implies that $-1 + b_{ee} < 0$, since $b_{ei} > 0$. Then the determinant is positive, the trace is negative, and the down state is unconditionally, asymptotically stable. The middle state, E_s, occurs at a point on the u-nullcline where the slope is positive and exceeds that of the v-nullcline (violet), so we have the inequality, $\frac{-1+b_{ee}}{b_{ei}} > \frac{b_{ie}}{1+b_{ii}}$. This implies that $D_0 < 0$, and hence, E_s is always a saddle point.

Lastly, the stability of the right-most fixed point, E_m, depends on the time constant, τ. Since the slope of the u-nullcline is positive, then $-1 + b_{ee} > 0$. Moreover, since it is less than the slope of the v-nullcline, then $D_0 > 0$, and the discriminant, $T_0^2 - 4\,D_0$, is negative, so E_m is always a spiral node. Then, the stability depends on the sign of the trace, which we see is negative for sufficiently small values of τ. As we increase $\tau > 0$, the trace increases through zero while the discriminant remains negative. Hence, the fixed point goes through a Hopf bifurcation at $\tau = \tau_{HB}$, where

$$\tau_{HB} = (1 + b_{ii})/(b_{ee} - 1) = (1 + a_{ii}\,\beta\,\bar{v}_m(1 - \bar{v}_m))/(\beta\,a_{ee}\,\bar{u}_m\,(1 - \bar{u}_m) - 1).$$

In Figures 2C,D, we show the bifurcation diagram of E_m as the time scale, $\tau = \tau_i/\tau_e$, varies. We remark that τ is convenient to use as a bifurcation parameter of the system, since it affects the phase plane dynamics without changing the nullclines. As previously mentioned, at low values of τ, E_m is stable. Then as τ increases, it loses stability through the Hopf bifurcation. As shown in Fig. 2C,D, a branch of stable periodic orbits emerges from the Hopf bifurcation, and the green curves in Fig. 2A,B correspond to the periodic orbit at $\tau = 0.6$. The difference between the two columns in Fig. 2 is the number of equilibria: There are three equilibria in panels A,C ($\theta_e = 0.125$) and one equilibrium in panels B,D ($\theta_e = 0.08$). So when there is a down state, as in Fig. 2C, the limit cycles terminate on a homoclinic

orbit (which connects the unstable manifold to the stable manifold of the saddle point) as τ increases. This is shown with a blue dot in Fig. 2C, and the corresponding homoclinic orbit is the larger of the two closed curves (blue) in Fig. 2A. For θ_e small enough, E_m is the only equilibrium of the system, and if τ is small enough, it is stable; otherwise, there is a stable limit cycle like the one in Fig. 2B. In panel D, we show that the green curve of limit cycles that persist for all $\tau > \tau_{HB}$ when $\theta_e = 0.08$. To go from the phase plane in Fig. 2A to B, we decrease θ_e through a saddle-node bifurcation at which point the equilibria, E_d and E_s, come together.

In the presence of a down state, the stable manifold of the saddle point acts as a separatrix of the phase plane. That is, for small perturbations from the down state, E_d, the activity tends back to rest, but for sufficiently large perturbations (past the separatrix), the trajectory may go away from E_d. Hence, depending on the stability of the up state, E_m, the trajectory may tend to E_m, to a limit cycle surrounding E_m, or make an excursion around E_m and fall back to the rest state at E_d. We note that the up state, E_m, is on the middle branch of the cubic nullcline rather than on the right branch (not shown). In Chapter 11 of [17], the authors argue that this nullcline configuration (with a fixed point on the middle branch) is the only one that can explain the properties of up and down states to stimuli [64]. Moreover, this configuration has been used to explain the paradoxical effects of a sustained drive to the inhibitory population which decreases the firing rate of the excitatory *and* inhibitory populations [57, 74]. We describe this in more detail in the next section.

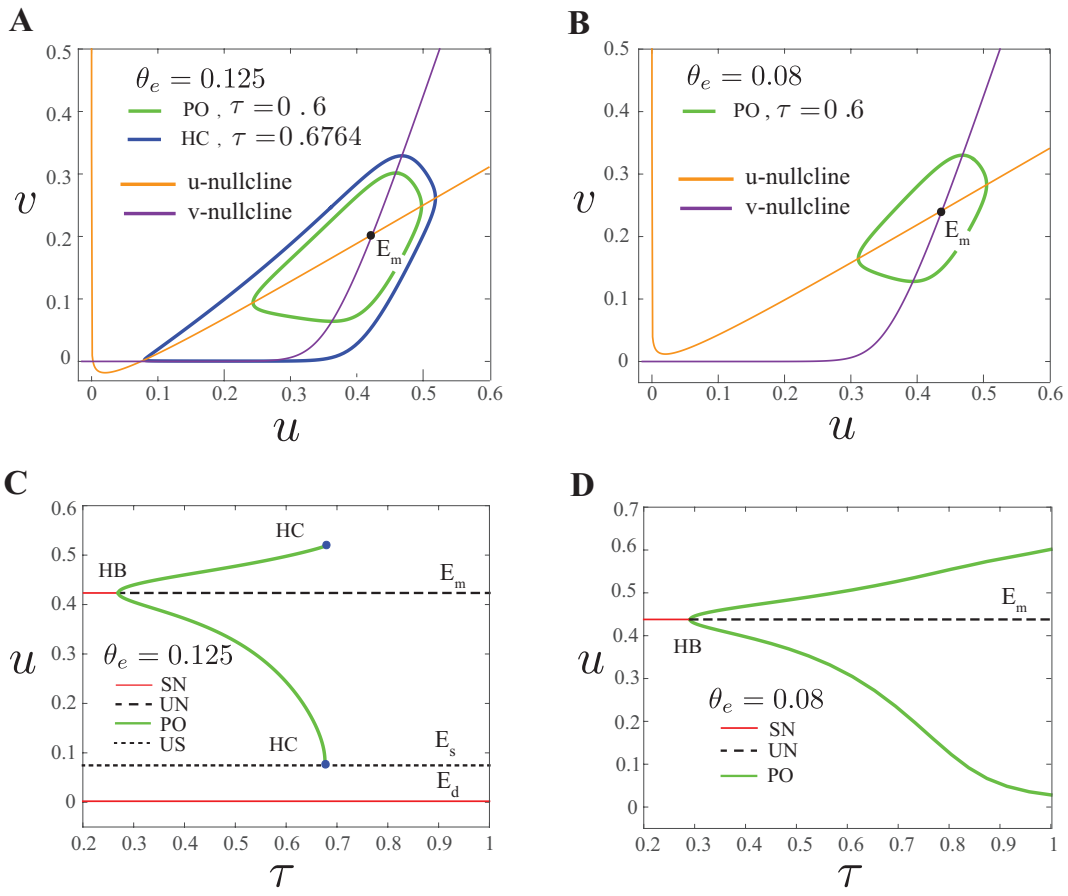

Figure 2: Phaseplane and bifurcation diagram of the ISN state. (A) Phaseplane for $\theta_e = 0.125$ with periodic orbit (PO), $\tau = 0.6$, and homoclinic (HC), $\tau = 0.6764$; (B) Phaseplane for $\theta_e = 0.08$. with PO, $\tau = 0.6$. (C) Bifurcation as τ increases when $\theta_e = 0.125$, showing three equilibria: The down state (E_d), saddle point (E_s) and up state (E_m). Stable PO's grow from a Hopf bifurcation (HB) and terminate at a homoclinic, HC; (D) Same as (C) but for $\theta_e = 0.08$ to show the PO's exist for all $\tau > \tau_{HB}$.

1.4 THE INHIBITORY STABILIZED NETWORK STATE

In Figure 2, we show the phase planes and bifurcation diagrams for the system in Eq. (1.2), corresponding to two different values of the threshold parameter, $\theta_e = 0.125$ and $\theta_e = 0.08$. These are on either side of a saddle-node bifurcation, so for $\theta_e = 0.125$, there are three equilibria, and for $\theta_e = 0.08$, there is one equilibrium. For all values θ_e of interest, there is an up state equilibrium, E_m, that occurs at the region of the u-nullcline where the slope is positive. Presumed to be the active state of the visual cortex, Ozeki et al. call this the inhibitory-stabilized network (ISN) state [57]. Ozeki et al. provide evidence for the ISN during stimulation of the cat visual cortex and show how the effect of surround stimulus on the ISN state transiently increases the inhibitory firing rate with the eventual decrease in firing rates for both excitatory and inhibitory populations (to rates lower than without surround stimulus). This behavior can be explained by looking at the nullcline structure in Fig. 3. An increase of input current to inhibitory neurons would translate the v-nullcline (violet) to the left (dash), and hence, the equilibrium would occur at a lower firing rate for both excitatory and inhibitory cells. As we have discussed, the ISN is stable for sufficiently small time constants of inhibition, and so, if the system starts at the ISN state, then a small change in synaptic input to inhibition would not change the stability of the equilibrium. Moreover, the inhibitory firing rates would initially increase as the excitatory firing rates would decrease until the rates pass through the v-nullcline. We see that trajectory spirals into the new equilibrium at lower firing rates.

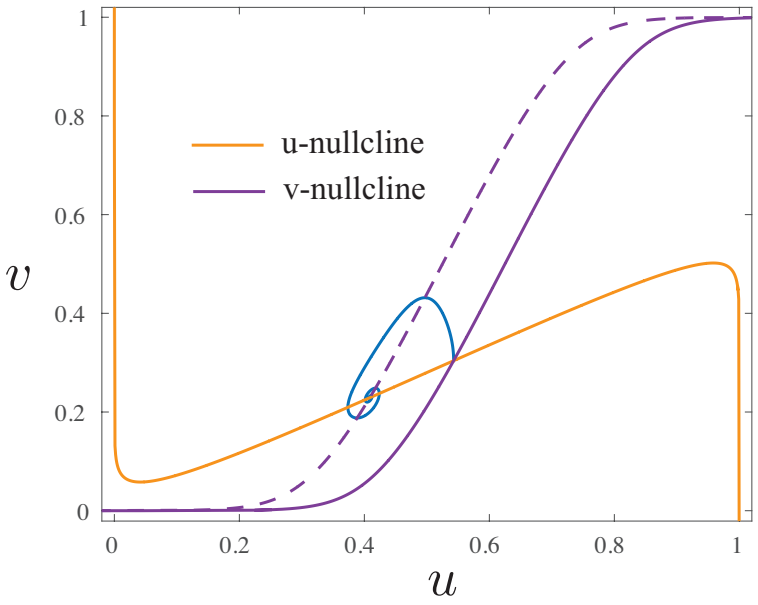

Figure 3: Phase plane to illustrate the ISN state. The excitatory nullcline (orange) and inhibitory nullcline (violet) for parameters: $a_{ee} = a_{ie} = 1$, $a_{ei} = 1.5$, $\theta_e = 0.08$, $\beta = 25$, $\tau = 0.2$, $\theta_i = 0.5$. We start the system at the intersection of these nullclines and apply a current $I_i = 0.1$, which shifts the v-nullcline to the left (dashed, violet), and the trajectory (blue) tends to a state with decreased firing rates.

1.5 THE SPATIALLY-DISTRIBUTED NETWORK OF WILSON-COWAN EQUATIONS

To extend the excitatory-inhibitory circuit to include spatially-dependent connections, we consider a continuum model and denote the excitatory (inhibitory) activities by $u(x,t)$ ($v(x,t)$) so that the rates now have both temporal and spatial components. We denote the spatial interaction function from population j to k by $K_{kj}(x)$ for $j,\, k \in \{e,\, i\}$. These interaction functions will appear in the model equations as spatial convolutions with the population activities, denoted by

$$(K_{kj}(x) \star u_j(x,t)) = \int_{\mathbb{R}} K_{kj}(x-y)\, u_j(y,t)\, dy \quad , \quad j,\, k \in \{e,\, i\}\,.$$

We will consider $K_{kj}(x) = K(x/\sigma_{kj})/\sigma_{kj}$, where σ_{kj} is the characteristic spatial length and make the following assumptions on $K(x)$:

1. The spatial profiles depend isotropically on the Euclidean distance.
2. The spatially-distributed connections have characteristic lengths that depend only on the presynaptic population so that $K_{kj}(x) = K_j(x)$ for $j \in \{e, i\}$.
3. The interaction functions monotonically decrease with distance from the origin, are integrable on the real line, and are normalized so that $\int_{\mathbb{R}} K_j(x)\, dx = 1$.

Using assumption 2, we illustrate the convolution in Fig. 4A by looking at the coupling between two spatial locations (for each population). Throughout this document, we show results for the exponential kernel that decays with distance, i.e. $K(x) = C\, \exp(-|x|)$ where C is some normalization constant. In the 1D spatial model, the kernels are given by

$$K_j(x) = \frac{1}{2\,\sigma_j}\, \exp\left(-\frac{|x|}{\sigma_j}\right) \quad , \quad j \in \{e,\, i\}\ .$$

For higher spatial dimensions, these kernels take a similar form but with a different prefactor, C. Though a Gaussian kernel may be used more often in these types of spatially-distributed networks, we choose the exponential (depicted in Fig. 4B,C) for purposes of mathematical analysis. Indeed, we will see in the coming sections that the convolutions of the interaction functions with the population activities may be written as second order partial differential equations.

With these preliminaries on the spatially-distributed connections, we now consider the spatially-extended Wilson-Cowan model:

$$\begin{aligned}\tau_e \frac{\partial u}{\partial t} &= -u + F(a_{ee} K_e(x) \star u - a_{ei} K_i(x) \star v - \theta_e) \\ \tau_i \frac{\partial v}{\partial t} &= -v + F(a_{ie} K_e(x) \star u - a_{ii} K_i(x) \star v - \theta_i) \ ,\end{aligned} \tag{1.3}$$

where $u = u(x,t)$, $v = v(x,t)$ are the activities of the excitatory and inhibitory populations, respectively; the parameters τ_j, $j \in \{e, i\}$ represent the time scales of the excitatory and inhibitory activities. Similar to the space-clamped system in Eq. (1.1), $F(u)$ is the nonlinear function representing the firing rate function, and θ_j are the thresholds. The parameters $a_{j\,k}$ are the (local) coupling strengths from population k to population j which modulate the amplitude of the spatially-distributed inputs. Since we are working on the entire real line, we may rescale the time and space variables so that we effectively have one time scale, $\tau := \tau_i/\tau_e$, and one spatial scale, $\sigma := \sigma_i/\sigma_e$, of the system. Hence,

$$K_e(x) = \frac{1}{2} \exp\left(-|x|\right) \ , \quad K_i(x) = \frac{1}{2\,\sigma} \exp\left(-\frac{|x|}{\sigma}\right) .$$

Thus, if $\sigma < 1$, then $\sigma_i < \sigma_e$, which is depicted in Fig. 4B for $\sigma = 0.5$. On the other hand, if $\sigma > 1$, then $\sigma_i > \sigma_e$, and we have the case of *lateral inhibition*, shown in Fig. 4C for $\sigma = 2.0$, which is the classical setup for pattern formation [1].

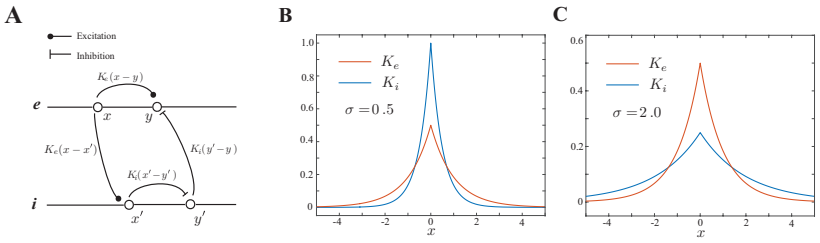

Figure 4: Connectivity diagram and spatial kernels. (A) Connectivity diagram in a one dimensional spatial model. (B) The excitatory (K_e) and Inhibitory (K_i) kernels without lateral inhibition: $\sigma < 1$. (C) Excitatory and Inhibitory kernels in the case of lateral inhibition $\sigma > 1$.

An important point to mention is that the spatially-homogeneous solutions of (1.3) coincide with solutions of the space-clamped system in (1.1), as long as the spatial kernels are normalized to one. Hence, solutions that are independent of x, such as bulk oscillations and fixed points, satisfy the WC equations, and we can use the phase plane analysis in Section 1.3 as a starting point for studying the spatially-distributed network. Throughout this document, we let $\beta = 50, a_{ee} = a_{ie} = 1, a_{ei} = 1.5, a_{ii} = 0.25$, $\theta_i = 0.4$, which are the parameter values for the space-clamped system shown in Fig. 2 and vary the remaining parameters: The threshold for excitation, θ_e, and the relative time and space constants, $\tau = \tau_i/\tau_e$ and $\sigma = \sigma_i/\sigma_e$.

1.6 OUTLINE

Here we give a brief "road map" of the thesis document: In each chapter, we begin with an introduction to the problem and end with a discussion of the results and how these compare with results from previous studies. Though each chapter may stand on its own, each contributes to the broader scope of the document which is to analyze spatio-temporal pattern formation and traveling waves in the model.

In Chapter 2, we study spatio-temporal pattern formation when the space-clamped system exhibits an oscillation around the up state (ISN state). This corresponds to a synchronous or bulk oscillation on the network level and the aim is to analyze the mechanism by which synchrony is broken. The patterns are similar to those found in Rule et. al. [63] with the difference being that there system included a periodic input while in our system the oscillation is intrinsic to the dynamics. Then in Chapter 3, we study the traveling wave solutions of the spatially-distributed network to better understand the transitions from traveling fronts to solitary pulses. We use our knowledge of the bifurcations in the space-clamped system along with the results of Chapter 2 in order to guide our analysis of these transitions. Interesting findings include a saltatory or lurching wave that arises as the spatial spread of inhibition increases as well as bistability between a front-like wave (that leaves doubly-periodic patterns in its wake) and a traveling solitary pulse.

Then in Chapter 4, we revisit the Wilson-Cowan equations when the firing rate function is the Heaviside step function. For the nonsmooth system, the middle branch equilibrium is a pseudo equilibrium in the sense that it falls within the inclusion of the Heaviside step function and is the solution of a system of (affine) linear equations. However, there is no linearization around the equilibrium state, and so, the stability requires a different approach. We perform a perturbation to show the stability of the up state and find that the system passes through a (pseudo) Hopf bifurcation for a value of τ that differs from the Hopf bifurcation for any system that limits to the piecewise defined system. The bifurcation analysis of the nonsmooth WC equations gives us a starting point for Chapter 5 wherein we study the traveling wave solutions to the nonsmooth spatially-distributed network.

2.0 SPATIO-TEMPORAL PATTERN FORMATION

This chapter is based on [32].

2.1 INTRODUCTION

Spontaneous symmetry breaking from a spatially uniform state is the most common mechanism for pattern formation in many physical systems [12, 37]. Typically, one starts with a spatially uniform constant solution and then performs a linear stability analysis to determine when there will be instability. Depending on the modes that become unstable, complex spatio-temporal patterns arise that include hexagons, stripes, of various orientations, and more complicated temporally varying patterns [66, 37]. In a biological or chemical setting, models for pattern formation begin with two species: an activator and inhibitor (or, excitatory and inhibitory components), and in order to get pattern formation, assume that the reach of the inhibitor is greater than that of the activator (so-called *lateral inhibition*). However, there are many systems where the negative (inhibitory) feedback does not spatially extend beyond the positive (activator) feedback. Furthermore, it may be that the spatially uniform state is not constant, but rather is oscillatory. Thus, it is of general interest to see whether or not lateral inhibition is necessary to get pattern formation in any homogeneous system and if not, how such patterns might arise.

In the nervous system, symmetry-breaking patterns have been associated with visual hallucinations, working memory, and feature maps. In each of the models that leads to pattern formation, there is an explicit assumption that the spatial spread of inhibition extends farther than that of excitation. However, it has been shown in certain areas of sensory

cortex that inhibition has slightly less or about the same spread as excitation. For instance, Levy and Reyes present distance-dependent connection profiles for data from primary auditory cortex in mouse and show that for two broad classes of interneurons, fast-spiking and non-fast-spiking cells, the synaptic connection profiles for inhibition to excitation is narrower than the reciprocal (excitation to inhibition) connection profile [48]. In this chapter, we show that a spatially extended two population model of cortex can exhibit spatio-temporal patterns without assuming lateral inhibition. We show that for some choices of parameters, it is possible to get symmetry breaking instabilities even when there is *no spread of inhibition*, that is when inhibition is only local.

2.2 PATTERN FORMATION IN THE UP STATE

2.2.1 Stationary Patterns

Before studying traveling wave solutions, we turn to the behavior of equation (1.1) near the up state since the waves join the down state to the up state, so at the very least, we want this state to be stable. In the previous section, we showed that the up state of the homogeneous (space-clamped) system was unstable once the inhibition time constant exceeded τ_{HB}. Here we examine the stability of the spatially extended network and show that there can be a Turing instability of the spatially homogeneous, constant steady-state. To determine whether a stationary pattern may form, we linearize around the ISN, which for the perturbation analysis we will denote $(\bar{u},\, \bar{v}) = (\bar{u}_3, \bar{v}_3)$. Consider a perturbation of the form

$$U(x,t) = \bar{u} + \varepsilon\, u(t)\, e^{i\,\omega\, x} \;\;,\;\; V(x) = \bar{v} + \varepsilon\, v(t)\, e^{i\,\omega\, x} \;\;,$$

so that

$$\begin{aligned} K_e(x) \star U(x,t) &= \bar{u} + \varepsilon\, \hat{K}_e(\omega)\, u(t)\, e^{i\omega\, x} \\ K_i(x) \star V(x,t) &= \bar{v} + \varepsilon\, \hat{K}_i(\omega)\, v(t)\, e^{i\omega\, x} \;\;, \end{aligned} \tag{2.1}$$

where $\hat{K}_j(\omega)$ are the Fourier transforms of $K_j(x)$. We can use the constant steady-state conditions in (1.2) and collect order ε terms to obtain a family of linear two-dimensional

ODEs parameterized by wavenumber, ω:

$$\begin{aligned} u_t &= -u + b_{ee}\hat{K}_e(\omega)u - b_{ei}\hat{K}_i(\omega)v \\ \tau\, v_t &= -v + b_{ie}\hat{K}_e(\omega)u - b_{ii}\hat{K}_i(\omega)v \ , \end{aligned} \tag{2.2}$$

where b_{jk} are constants $b_{jk} = a_{jk}\, F'(a_{j,e}\,\bar{u} - a_{j,i}\,\bar{v} - \theta_j)$ and $\tau = \tau_i/\tau_e$ is the time constant of inhibition relative to excitation. Then the linearization is a family of matrices which are parametrized by ω,

$$A(\omega) = \begin{pmatrix} -1 + b_{ee}\hat{K}_e(\omega) & -b_{ei}\hat{K}_i(\omega) \\ \left(b_{ie}\hat{K}_e(\omega)\right)/\tau & \left(-1 - b_{ii}\hat{K}_i(\omega)\right)/\tau \end{pmatrix} .$$

By the choice of firing rate function, F satisfies the logistic equation, $F' = \beta\, F\,(1-F)$. Now, since $(\bar{u}, \bar{v})$ satisfy (1.2), we obtain $b_{je} = a_{je}\,\beta\,\bar{u}\,(1-\bar{u})$ and $b_{ji} = a_{ji}\beta\,\bar{v}\,(1-\bar{v})$. Then the trace of $A(\omega)$ is $\mathrm{Tr}(\omega) = b_{ee}\hat{K}_e(\omega) - 1 - \left(1 + b_{ii}\hat{K}_i(\omega)\right)/\tau$. For the case that we study here, the trace is negative for small $\tau > 0$. Then the only way for an instability to occur is for the determinant to become negative for some positive value of ω and that the determinant be positive at $\omega = 0$. We consider $D(\omega) = \left(1 - b_{ee}\hat{K}_e(\omega)\right)\left(1 + b_{ii}\hat{K}_i(\omega)\right) + b_{ei}\, b_{ie}\, \hat{K}_i(\omega)\, \hat{K}_e(\omega)$, which is τ multiplied by the determinant of $A(\omega)$ and see that

$$\begin{aligned} D(0) &= (1 - b_{ee})\,(1 + b_{ii}) + b_{ei}\, b_{ie} \\ &= (1 - \beta\bar{u}(1-\bar{u}))\ (1 + a_{ii}\,\beta\bar{v}\,(1-\bar{v})) + a_{ei}\,\beta^2\,\bar{u}\,(1-\bar{u})\,\bar{v}\,(1-\bar{v}) \\ &= 1 + \beta\ (a_{ii}\,\bar{v}\,(1-\bar{v}) - \bar{u}\,(1-\bar{u})) + \beta^2\,(a_{ei} - a_{ii})\,\bar{u}\,(1-\bar{u})\,\bar{v}\,(1-\bar{v}) \ . \end{aligned}$$

Since the fixed point $(\bar{u}, \bar{v})$ depends on the parameter β, this is not simply a quadratic in β. However, if we treat it as such, we find that the discriminant is negative for all $\beta > 0$, so that $D(0) > 0$, as desired. In Fig. 5A, we graph the function $D(\omega)$ and find that $\sigma = \sigma_i/\sigma_e$ must be greater than one in order for the spatially-homogeneous constant solution to go unstable. In addition, we show the Turing stripes that can arise as a stationary pattern (Fig. 5B).

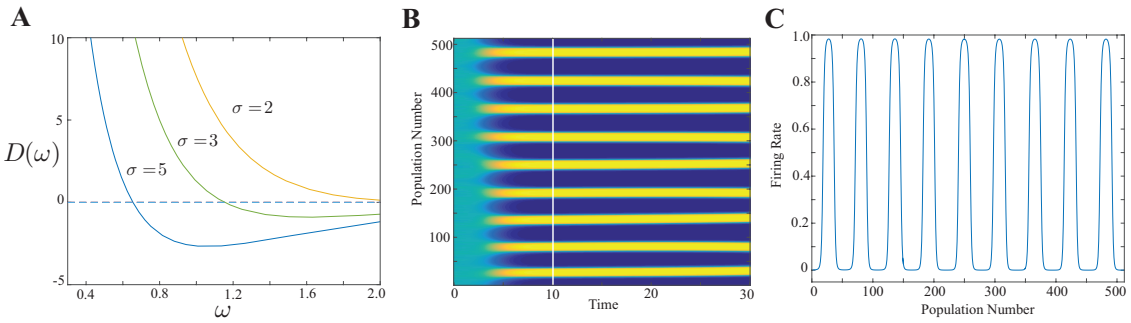

Figure 5: Stationary patterns. (A) The graph of $D(\omega)$ for three values: $\sigma = [2, 3, 5]$ to show the Turing-instability as the spatial spread of inhibition increases in the system. (B) Turing stripes of the excitatory population array for $N = 512$, when $\sigma = 3$ and $\tau = 0.1$. (C) A cross-section (vertical, white line) of the time-invariant stripes from the excitatory array in panel (B) at time $t = 10$.

2.2.2 Spatio-temporal Patterns from a Bulk Oscillation

For the spatially extended WC system, symmetry-breaking pattern formation can occur at the spatially homogeneous equilibrium, E, when there is lateral-inhibition ($\sigma_i > \sigma_e$) and τ is small enough so that there are no limit cycles in the homogeneous system [21]. Figure 6A depicts such a case in which we observe spatially periodic, time-invariant stripes. While it is possible to obtain pattern formation from a homogeneous equilibrium in the WC equations when $\sigma_e < \sigma_i$, the conditions require careful tuning of parameters and the difference between the two length scales is small (see Appendix A for calculations). However, since in most cortical circuits, the spatial extent of inhibition is generally less than that of excitation, we now let $\sigma_i = 6.67 < 10 = \sigma_e$, and increase $\tau = 0.4$ so that there is a bulk oscillation, i.e. a spatially homogeneous, temporally periodic solution, as shown in Fig. 6B. Further increasing $\tau = 0.6$ causes the spatially homogeneous oscillation to become unstable, which results in a pattern that is periodic in both space and time, as shown in Fig. 6C.

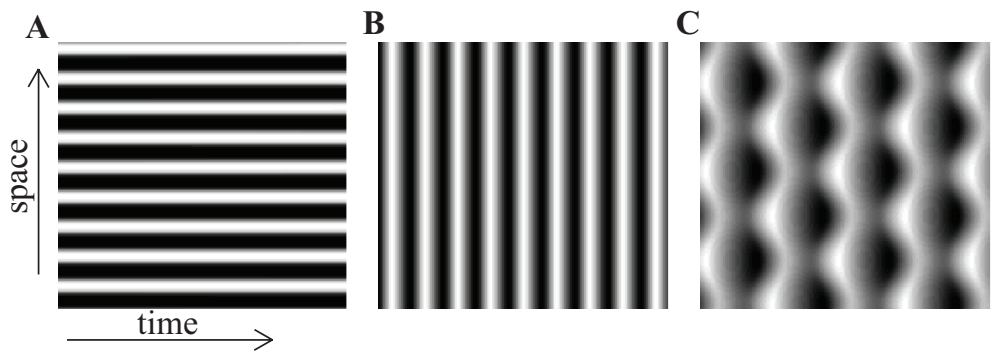

Figure 6: Simulations of a network ($N = 256$) of coupled WC neurons. (A) Classic Turing patterns from a steady state when $\theta_e = 0.08$, $\sigma_e = 10$, $\sigma_i = 20$, and $\tau = 0.2$. (B) Reducing σ_i to 6.67 and increasing $\tau = 0.4$ induces a spatially homogeneous periodic oscillation. (C) Further increasing $\tau = 0.6$ results in periodic spatio-temporal patterns.

2.2.3 Linear Stability Analysis

In order to investigate the bifurcation from a homogeneous constant state, we simply linearize and take the Fourier transform resulting in a family of 2×2 matrices whose eigenvalues are easy to compute (see Appendix A). However, in the present case (e.g. as in Fig. 6B,C), the spatially homogeneous solution is a periodic orbit, so we must take a different approach. We linearize Eq. (1.1) around the spatially homogeneous periodic solution, $(\bar{u}(t), \bar{v}(t))$, and perturb the solution with respect to spatial frequency ω. We take the perturbation to be of the form

$$U(x,t) = \bar{u}(t) + \varepsilon\, u(t)\, e^{i\,\omega\, x} \;\;,\;\; V(x,t) = \bar{v}(t) + \varepsilon\, v(t)\, e^{i\,\omega\, x} \;\;,$$

so that

$$\begin{aligned} K_e \star U(x,t) &= \bar{u}(t) + \varepsilon\, \hat{K}_e(\omega)\, u(t)\, e^{i\omega\, x} \\ K_i \star V(x,t) &= \bar{v}(t) + \varepsilon\, \hat{K}_i(\omega)\, v(t)\, e^{i\omega\, x} \;\;, \end{aligned} \tag{2.3}$$

where $\hat{K}_j(\omega)$ are the Fourier transforms of $K_j(x)$. After a Taylor expansion and collecting order ε terms, we obtain a family of linear two-dimensional equations, parameterized by

wavenumber, ω:

$$\begin{aligned} u_t &= -u + b_{ee}(t)\hat{K}_e(\omega)u - b_{ei}(t)\hat{K}_i(\omega)v \\ \tau v_t &= -v + b_{ie}(t)\hat{K}_e(\omega)u - b_{ii}(t)\hat{K}_i(\omega)v \ , \end{aligned} \tag{2.4}$$

where $b_{jk}(t) = a_{jk}\, F'(a_{j,e}\,\bar{u}(t) - a_{j,i}\,\bar{v}(t) - \theta_j)$ and where $\tau = \tau_i/\tau_e$ is the time constant of inhibition relative to excitation. If the homogeneous state of the system is an equilibrium point, then b_{jk} are just constants and the stability reduces to the previously mentioned Turing-type analysis for constant steady states (see also [55]). If, on the other hand, the homogeneous solutions are oscillatory (as will be the case for $\tau > \tau_{HB}$), then Eq. (2.4) is a linear periodic system which we can write as $X' = A(t;\omega)X$ with

$$A(t;\omega) = \begin{pmatrix} -1 + b_{ee}(t)\hat{K}_e(\omega) & -b_{ei}(t)\hat{K}_i(\omega) \\ \left(b_{ie}(t)\hat{K}_e(\omega)\right)/\tau & \left(-1 - b_{ii}(t)\hat{K}_i(\omega)\right)/\tau \end{pmatrix} .$$

Here we include the parameter ω to emphasize that the solutions depend on the wavenumber perturbation. We solve this linear T-periodic equation with initial conditions, $X = I$, where I is the identity matrix, to form a principal matrix of solutions. After one period, we obtain the Monodromy matrix $M(\omega) := X(T;\omega)$ which, for our system, is a 2×2 matrix, parametrized by ω. If any of the eigenvalues of $M(\omega)$ have magnitude greater than 1 for some value of ω, then the limit cycle will lose stability with spatial mode ω. With a 2×2 matrix M, there are three ways to lose stability: (i) a real eigenvalue increases above 1; (ii) a real eigenvalue decreases below -1; (iii) a complex pair obtains a magnitude greater than 1.

One need only check the determinant (D) and the trace (Tr) of M(ω) to test these conditions: (i) $Q_1 :=$ 1−Tr+ D > 0; (ii) $Q_2 :=$ 1+Tr+D> 0; (iii) $Q_3 :=$ 1−D> 0. That is, if any of these test functions falls below 0 as some parameter such as ω changes, then an instability will occur. Figure 7 shows a schematic of these conditions. With this background, we numerically solve the spatially homogeneous equations for one period, compute the Monodromy matrix, and then look for zero crossings of the three quantities. We have found that only Q_2 changes sign as ω varies, so henceforth, this is the only test function that we follow. We note that Q_2 signifies a period-doubling bifurcation, so we expect the bifurcating solution to

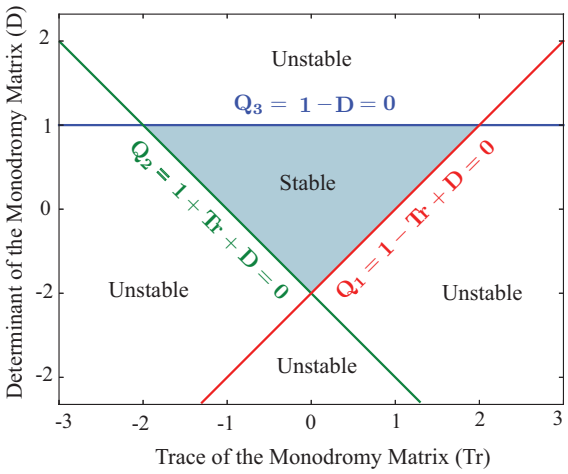

Figure 7: Diagram to show the boundaries for instability in terms of the trace (Tr) and determinant (D) of the Monodromy matrix.

repeat every other cycle, such as the pattern shown in Fig. 6C.

There are three parameters of interest to us: (1) The inhibitory space constant σ_i, (2) the inhibitory time constant τ_i, and (3) the excitatory threshold θ_e. Since space and time can be rescaled, the inhibitory space and time constants in Figures 8-11 are relative to those of excitation: $\tau = \tau_i/\tau_e$ and $\sigma = \sigma_i/\sigma_e$. The excitatory threshold, θ_e, switches the system from one to three equilibria and determines if the limit cycles terminate on a homoclinic orbit (see Fig. 2A). We find that for large enough space constant σ, the quantity $Q_2(\omega)$ has two roots that signify an interval of wavenumbers, ω, for which the homogeneous limit cycle is unstable. In Fig. 8, the blue curves show the graph of Q_2 as a function of wave number ω for a fixed value of σ. By varying σ, we can cause the two roots, indicated by the green curve in Fig. 8, to come together at a double root. This corresponds to a turning point of the green curve in the (σ, ω) plane, as seen in the right panel. The critical value of σ at which this occurs sets the boundary for pattern forming instabilities.

From here, we can follow the critical value of σ as τ varies for different choices of θ_e to obtain a family of curves that delineate where the homogeneous limit cycle is unstable. In Figure 9, we show these curves for the exponential kernel and find several qualitatively

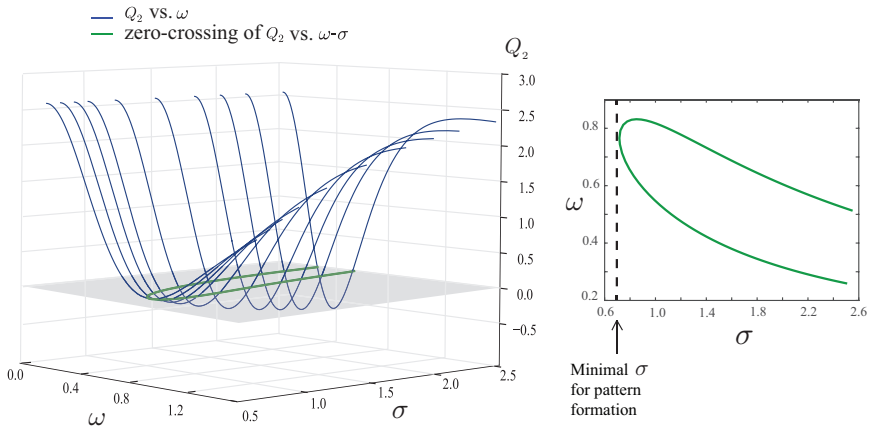

Figure 8: Surface plot of the test function Q_2 as a function of (σ, ω) for $\theta_e = 0.08$ and $\tau = .5$. Each blue curve is Q_2 as a function of ω for fixed σ. The green curve indicates the level set $Q_2 \equiv 0$ as σ and ω vary, and the right panel depicts the green curve in the gray plane. As σ decreases, the two zeros come together at the turning point of the green curve; this sets the minimal σ for pattern formation, which in this case is $\sigma \approx .716$, indicated by the vertical dashed line.

different aspects of them. Consider when $\theta_e = 0.125$, large enough so that there are three equilibria. In this case, limit cycles exist for τ-values between the Hopf and the homoclinic ($\tau_{HC} \approx 0.67$, for $\theta = 0.125$) bifurcations, and the instabilities occur between the solid and dashed (red) curves. The Hopf bifurcations (independent of σ) occur at the values of τ that are minima for the lower pattern forming cuves. When $\theta_e < 0.09783$,(the value for a saddle-node of equilibria), e.g. $\theta_e = 0.08$, there is a unique equilibrium point and a spatially homogeneous limit cycle for all $\tau > \tau_{HB}$. That is, there is no homoclinic boundary. In this case, there is a turning point in the stability curve which bounds the minimal value of σ for pattern formation away from zero (shown by the three upper solid curves). In Fig. 9, we show the stability curves for several values of excitatory threshold where there is no homoclinic: for $\theta_e = 0.097$ (violet), the system is near the saddle-node bifurcation of equilibria, and for $\theta = 0.08841$ (blue), there is a cusp at $\sigma = 0$. Here, we emphasize that σ can extend all the way down to $\sigma = 0$ for some choices of θ_e, so that patterns may occur even when

there is only local inhibition when $\theta_e \in (0.08841, 0.09783)$.

From the stability boundaries shown in Fig. 9, it is clear, that there are regions where

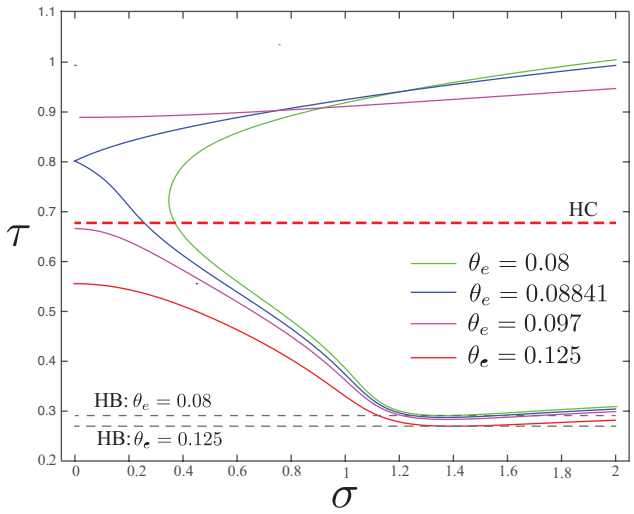

Figure 9: Stability diagram for the homogeneous periodic orbit as the parameters (σ) and time constant (τ) vary for the spatially-extended WC model. The homoclinic (HC) line corresponds to $\theta_e = 0.125$. Hopf bifurcations (HB) occur at the minima of each of the lower plotted curves.

$\sigma < 1$ and the homogeneous state loses stability. What is more interesting is that there is an upper bound on τ for which the uniform state loses stability, which is to say that inhibition can neither be too slow nor too fast. For θ_e-values that yield a turning point in the curve (e.g. $\theta_e = 0.08$), the upper boundary increases with increasing σ. As σ passes through one, the excitatory and inhibitory populations have identical spatial scales. Moreover, the upper boundary occurs at a value of $\tau < 1$, so the symmetry-breaking mechanism relies on the difference in time scales. As we further increase the spatial scale so that $\sigma > 1$, the upper boundary passes through $\tau = 1$ and there can occur patterns when the time scales of excitatory and inhibitory populations are the same. Next we compare the behavior of the theoretical stability curves with the behavior of the 1D spatial model. We discretize Eq. (1.1) into 256 points for each population, start close to the equilibrium point (with some added heterogeneity to break the symmetry) and then integrate over a range of parameters. We track the *spatial* variance of the simulation in order to automatically determine the strength

of the pattern.

Figure 10(a) shows the case of a single equilibrium point ($\theta_e = 0.08$) in which patterns seem to exist only in regions of parameter space where the uniform oscillation is unstable to spatial perturbations. Again, we remark that if τ is too large, then the uniform oscillation is always stable for $\sigma < 1$. Fig. 10(d) shows that the bottom boundary is limiting for patterns but the top boundary (determined by the homoclinic bifurcation of the homogeneous state) is not the limiting boundary. This means that there are patterns for parameter regimes in which there is *no homogeneous limit cycle.* There is no *a priori* reason that we would expect the linear stability analysis to predict the regime of nonlinear pattern formation; it is just a condition for the uniform state to be unstable.

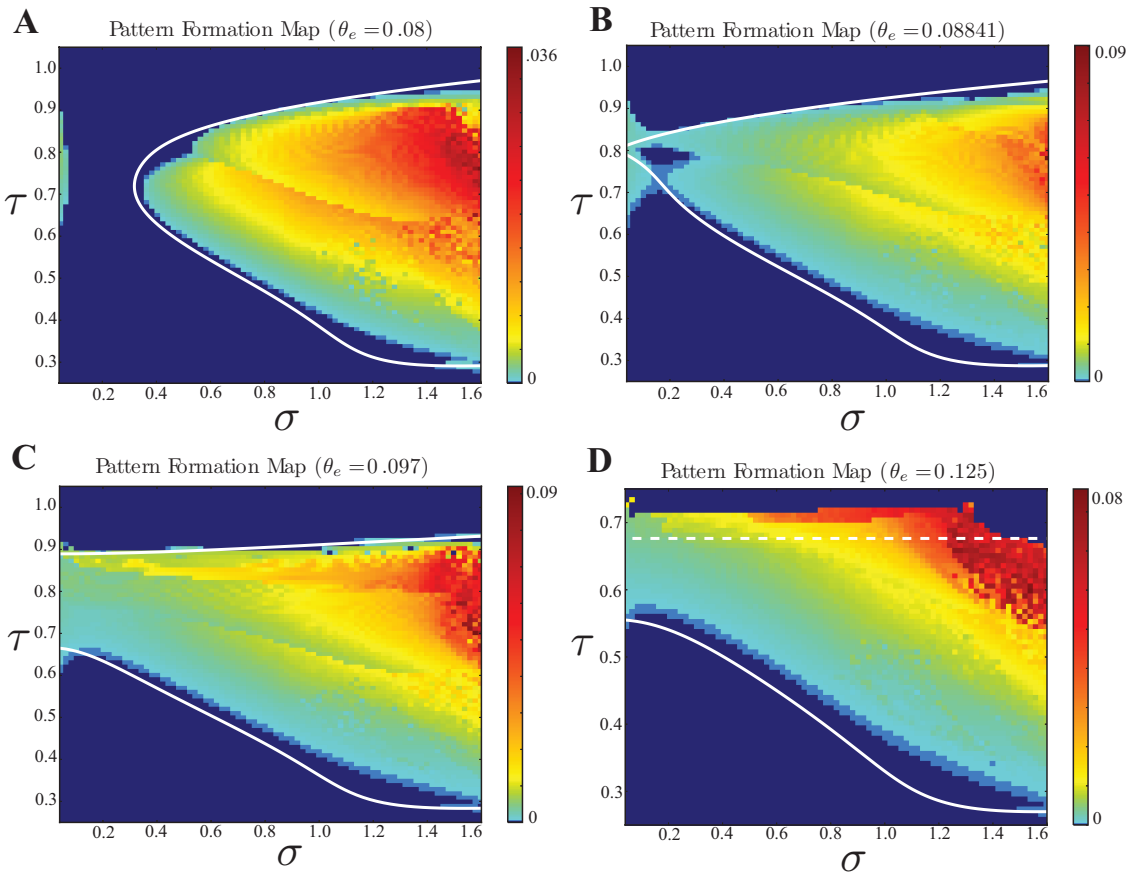

Figure 10: Comparison between the stability diagram from the linear theory and the full simulations. (a) $\theta_e = 0.08$: Patterns remain entirely in the instability region. (b) $\theta_e = 0.08841$: When the boundary breaks open at $\sigma = 0$. (c) $\theta = 0.97$ slightly less than the value of the saddle-node bifurcation. (d) $\theta_e = 0.125$: The upper boundary (horizontal, dashed line at $\tau = 0.6764$) is the homoclinic, and patterns can exist in regions where there is no limit cycle (above the line).

2.2.4 Pattern Formation with No Spatial Spread of Inhibition

Looking at Figures 10(c) and (d), there appear to be regions where there are patterns in the case of $\sigma = 0$, which is very surprising since there is now only one length scale in the system. Since this phenomena seems to depend on θ_e, we consider the behavior when $\sigma = 0$ and vary τ and θ_e. In Appendix A, we show that no pattern formation can arise from a constant state when $\sigma_i = 0$ (that is, $\sigma = \sigma_i/\sigma_e = 0$). Figure 11 shows the regime in (θ_e, τ) where there exist oscillations to the uncoupled system (the bulk oscillation). For θ_e to the left of the saddle-node value, $\theta_{SN} \approx 0.09783$ (labeled SNIC in Fig. 11), there is only one equilibrium point and it is unstable for τ above the curve of Hopf bifurcations. For $\theta_e > \theta_{SN}$, the bulk oscillation exists for τ between the Hopf bifurcation curve and the lower section of the homoclinic curve. Furthermore, within the region where there is a bulk oscillation, there is a curve labeled PF, above which the bulk oscillation is unstable and we expect pattern formation. Interestingly, this region extends slightly below θ_{SN} for a limited band of τ where there is only a limit cycle and a single equilibrium point. The smallest θ_e such that there is a range of τ-values for which the bulk oscillation is unstable is approximately $\theta_e \approx 0.08841$ and corresponds to the cusp seen in figure 9 at $\sigma = 0$.

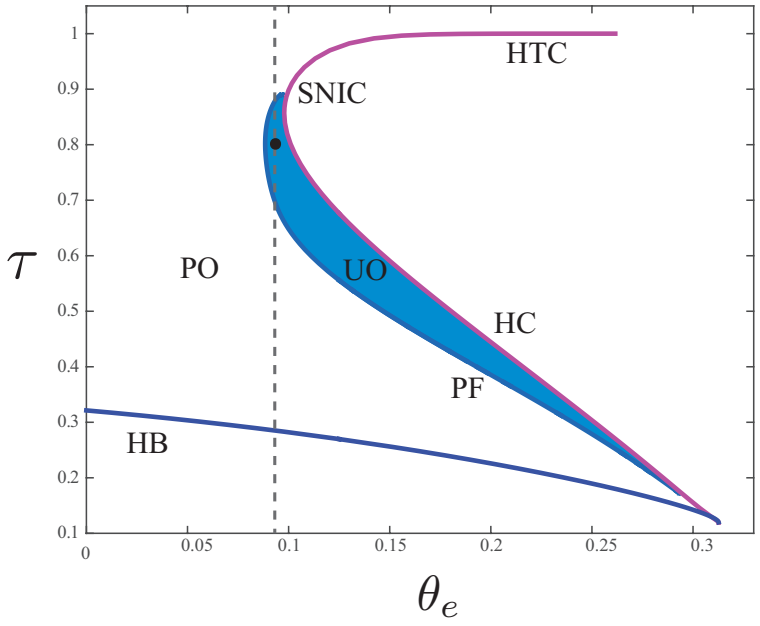

Figure 11: Phase-diagram showing regions where there is a periodic orbit (PO) and pattern forming instabilities as τ and θ_e vary with no spread of inhibition ($\sigma = 0$). The shaded region labeled UO, bounded between the homoclinic (HC) and pattern forming (PF) curves, indicates instabilities to the bulk oscillation when $\sigma = 0$. The upper branch labeled HTC is the curve of heteroclinic orbits (joining the saddle point with the down-state), while the lower branch labeled HC is the curve of homoclinics. These come together at a turning point, corresponding to a saddle-node on an invariant circle (SNIC). The vertical dashed line is $\theta_e = 0.094$, showing an interval of τ-values that give rise to pattern formation when there is one equilibrium. The black dot at $(\theta_e, \tau) = (0.094, 0.8)$ corresponds to parameters in Fig. 12(c).

2.3 THE TWO DIMENSIONAL NETWORK

Thus far, we have only considered the Wilson-Cowan equations with 1D spatial coupling and analyzed the stability of the bulk oscillation to certain wavenumber perturbations. However, the analysis for the 2D system will be identical to that of the 1D system, and in fact, it is the same for n-dimensional systems, as long as the spatial coupling profile decays with the Euclidean distance. Here we take the kernel to be the decaying exponential,

$$K_j(\sqrt{x^2+y^2}) = \frac{1}{2\,\pi\,\sigma_j^2}\,\exp\left(-\frac{\sqrt{x^2+y^2}}{\sigma_j}\right) \quad , \quad j \in \{e,\, i\}\ .$$

Then we can use the curves in Figures 9 and 10 to find parameters where we would expect patterns in the 2D spatially connected network, though the analysis will indicate nothing about the stability of the pattern itself.

To illustrate the geometry of the period-doubled branch of solutions, we create an array of 256 by 256 excitatory and inhibitory neurons with periodic boundary conditions and simulate the 2D spatially connected network. We present the spatio-temporal patterns in Fig. 12 as a series of five frames over equal time intervals for one period, T, of the period-doubled oscillation. To simulate perturbing from the spatially uniform oscillation, we impart small random fluctuations to initial conditions near the periodic orbit. When the uniform oscillation is unstable, the system may tend to the sorts of spatio-temporal patterns shown in Fig. 12, in which spatially-alternating active and quiescent states in the first column frames switch positions at half a cycle (not shown) between the third and fourth column frames.

In Figure 12(a), we let $\theta_e = 0.125$ and the rest of the parameters be the same as in Fig. 7(c) to show pattern-formation in the presence of a down-state. Then in Fig. 12(b), we increase τ to 0.7, which is above the homoclinic bifurcation indicated in Fig. 9. Here we remark that the linear stability indicates pattern formation for the parameter set in Fig. 12(a), since the point (σ, τ) falls well between the lower stability curve and the upper homoclinic boundary of Fig. 9. However, for the parameter set in Fig. 12(b), there is *no uniform state oscillation*, yet a pattern emerges. Similar to the reduced model in Fig. 13(b), the period-doubled oscillations seem to be stable even past the homoclinic bifurcation at $\tau_{HC} = 0.6764$. Lastly, Fig. 12(c) shows pattern formation in the case when there is only

local inhibition, i.e. $\sigma_i = 0$, and the parameters $(\theta_e, \tau) = (0.094, 0.8)$ correspond to the point on the vertical line within the shaded area of Fig. 11.

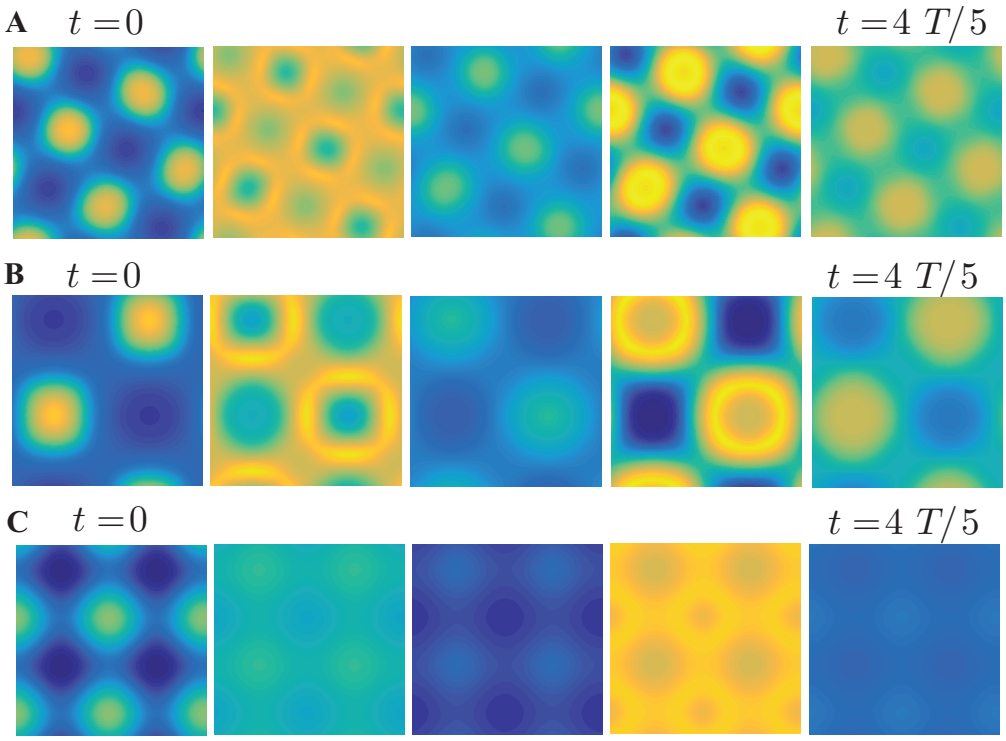

Figure 12: Five frames over one period for simulations of the 2D Wilson Cowan model with N=256 x 256 neurons. Spatio-temporal patterns when $\sigma_e = 10$ and parameters: (A) $\sigma_i = 6.67$, $\theta_e = 0.125$, $\tau = 0.6$, $T = 11.3$; (B) $\sigma_i = 6.67$, $\theta_e = 0.125$, $\tau = 0.7$, $T = 24.5$; (C) $\sigma_i = 0$, $\theta_e = 0.094$, $\tau = 0.8$, $T = 30.1$. These parameters correspond to the black dot at $(\theta_e, \tau) = (0.094, 0.8)$ in Fig. 11.

2.4 A REDUCED MODEL

We now describe a simple, highly reduced model that helps explain the difference in behavior between Fig. 10(a) and Fig. 10(d). We create a network of two pairs, $u_{1,2}$, $v_{1,2}$, with coupling between them. The coupling of pair 2 to pair 1 has the form $(1-q_e)u_1 + q_e u_2$ and $(1-q_i)v_1 + q_i v_2$, with a similar coupling for pair 1 to pair 2. That is, the coupling kernels, K_e, K_i are replaced with their two-point discrete analogs. If $q_{e,i} = 0$, then there is no coupling, and if $q_{e,i} = 0.5$, then the coupling is essentially all-all. We choose $q_e = 0.166$ and $q_i = 0.05$ so that the inhibitory coupling "spread" is less than a third of the excitatory. In Figure 13, we show the two bifurcation diagrams for the reduced system where respectively $\theta_e = 0.08$ and $\theta_e = 0.125$: In panel (a) where there is only one equilibrium point and the homogenous limit cycle exists for all $\tau > \tau_{HB}$, we see the periodic orbit becomes unstable at a period doubling bifurcation, and as τ further increases, the stable branch of period-doubled orbits connects back to the periodic orbit. This is qualitatively the same picture as Fig. 10(a). In contrast, panel (b) shows that while the periodic orbit becomes unstable at a period-doubling bifurcation as in (a), it does does not connect back to the branch of periodic orbits; instead, the stable period-doubled branch continues past the homoclinic bifurcation of the unstable periodic branch just as in Fig. 10(d).

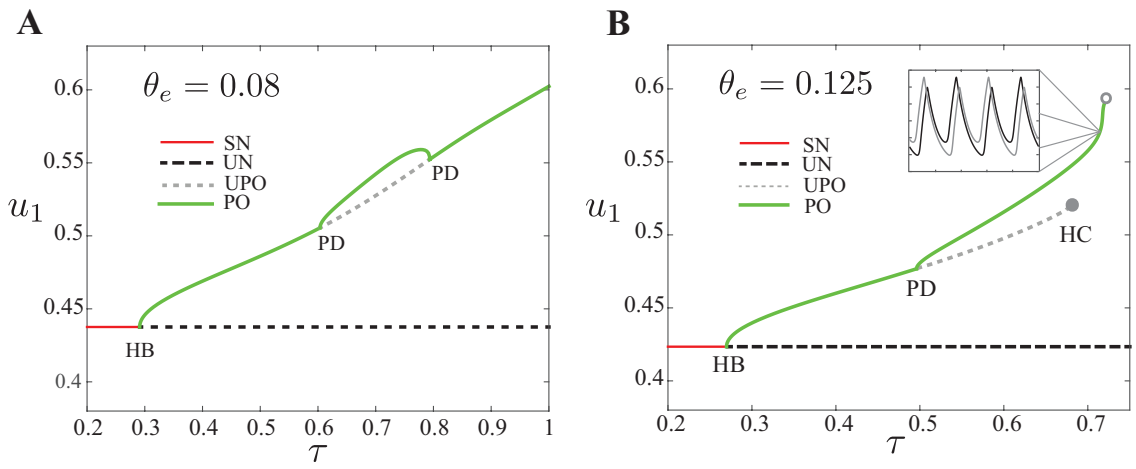

Figure 13: Bifurcation diagram for the pair of coupled WC equations. Labeling is the same as in Fig. 2 with an additional label for the unstable periodic orbits (UPO). (A) For $\theta_e = 0.08$, the curve of period-doubled orbits connects back to the branch of unstable periodic orbits, stabilizing the homogeneous periodic solution for all τ beyond the second PD-point. (B) For $\theta_e = 0.125$, unstable periodic orbits terminate at a homoclinic, HC. The inset shows u_1 and u_2 over two periods for $\tau = 0.7 > \tau_{HC}$.

2.5 DISCUSSION

In this chapter, we have shown that if the homogeneous state is a periodic solution rather than an equilibrium point, then it is quite easy to obtain pattern formation even when the inhibition has a much smaller spread than the excitation. In fact, the variance maps in Fig. 10(c) and (d) compared with the analytic curves from Figures 9 and 13 show that when τ is close to the homoclinic bifurcation, then there can be spontaneous pattern formation even if there is *no* inhibitory spread. A similar surprising result is that there can be patterns even when the excitatory and inhibitory interactions are identical; in both instances, there is only one characteristic length scale. In these cases, we observe from Fig. 9 that whenever $\sigma < 1$, the regions of instability lie below the line $\tau = 1$. This suggests that the symmetry-breaking mechanism must result from the difference in time scales of excitatory and inhibitory populations. Indeed, if the time scales and the space scales are the same, then we conjecture that no patterns can spontaneously arise from the oscillatory state.

Though we have found some similar work on pattern formation in the literature, there are notable differences between these results and results presented in this chapter. For instance, Kuramoto [45] has shown the existence of complex spatio-temporal patterns. He derives an equation for the spatial phase gradient that has the form $\theta_t = a\theta_x^2 - b\,\theta_{xx} - c\,\theta_{xxxx}$ which can be derived from any system of spatially coupled oscillators in the long-wave limit. The same analysis can be applied to the Wilson-Cowan system [20], but to get the coefficients $b, c > 0$ requires lateral inhibition. Since the Kuramoto result is a long-wave instability, we believe the mechanism in these papers is different from ours which is a finite wavelength instability.

As seen in Figures 6C and 13, the pattern formation arises via a period doubling bifurcation of the spatially homogeneous oscillatory state. In this sense, it is quite reminiscent of bifurcations seen in uniformly periodically forced systems. Crawford [11] and Silber [65] studied these phenomena using symmetry and bifurcation methods and [11] derived a normal form for this bifurcation. However, their set-up was more abstract, so it is unclear whether or not they needed lateral inhibition to obtain the pattern forming states. In a more closely related paper, Rule et al. [63] study the Wilson Cowan equations with uniform periodic driving and found pattern formation both through period doubling and a pitchfork bifurca-

tion. In this paper, they required lateral inhibition. Yang et al. [78] were among the first (to our knowledge) to use Floquet theory to analyze pattern formation in either an intrinsically oscillatory or a periodically forced chemical system. The authors found a variety of patterns arising from a period-doubling bifurcation much as we have seen here. However, they require lateral inhibition in their model.

More recently, [4] studied general two-variable reaction diffusion equations when there was a bulk oscillation. They provide some approximations for conditions on spatial patterns, but once again, the authors require lateral inhibition. Another paper worth mentioning is [67], in which Steyn-Ross et al. consider a mean field model of cortex with inhibitory diffusive coupling to study interneuronal gap junctions. They show that for large values of the inhibitory diffusion constant, D_i, Turing patterns can emerge, while for smaller values of D_i, the homogeneous fixed point can pass through a Hopf bifurcation to give rise to a bulk oscillation. Then, by tuning the inhibitory rate and diffusion constants, so that the system is near a codimension 2 Turing-Hopf bifurcation, they show complex spatio-temporal patterns. Though this seems like a similar setup as ours, the symmetry-breaking mechanism is different: While they analyze perturbations from a homogeneous fixed point and find patterns arising from competing Turing and Hopf instabilities, we linearize around a homogeneous oscillation and show patterns arising from a period-doubling bifurcation. Moreover, they take the diffusion constant of inhibition to be much greater than that of excitation, and thus, keeping with the theme, they require lateral inhibition. Whether or not other systems such as these reaction diffusion systems can show the same types of bifurcations in the absence of lateral inhibition remains an open question.

3.0 TRAVELING WAVES

3.1 INTRODUCTION

Cortical waves have been observed in a variety neural circuit experiments. Examples from slice preparation include hippocampal slices in guinea pigs [71], and rodent neocortex [6]. In addition, experimentalists have observed traveling waves *in vivo*, such as in the study of neural responses to whisker deflection in barrel cortex of anesthetized rats [80, 75] and more recently, in propagation reliability in primary visual cortex of awake macaques using multichannel electrodes [54]. The authors in [29] suggest that the shape and velocity of cortical waves in neocortex may be important to understanding underlying structures of the network. Their role in sensory and motor processing ranges from inducing variability [41] to controlling motor patterns [16, 62, 68, 35, 34, 79] to setting diverse phases in sensory oscillations [50, 52]. In addition, several researchers suggest that understanding the initiation and termination of so-called epileptiform events that lead to seizure activity may prove paramount for developing therapeutic techniques for seizure patients [59, 72].

There is a long-standing history in modeling traveling waves in nonlinear systems in general and more specifically, in neural field theory. Moreover, there has been an effort to develop theoretical models along with experimental results to qualitatively describe wave propagation and make further predictions. For instance, the authors in [5] studied the effects of $GABA_A$-mediated inhibitory post synaptic potentials on the initiation, propagation, and termination of synchronous activity in slices of rat neocortex. Rather than capturing all of the synaptic dynamics as in the Hodgkin-Huxley model, theorists often consider a reduced model such as the FitzHugh-Nagumo equations, which does not take into account voltage-gating variables. Moreover, since many areas of sensory cortex have a spatial-structure [48],

neural field equations with 1D continuous space can be used to model cortical waves [7]. Amari considered a scalar firing rate model given by a partial integro-differential equation. By assuming a Heaviside Step function for the transfer function, he was able to analytically construct localized patterns of activity and assess their stability to determine wave propagation [1]. Since then, many others have studied traveling waves in spatially-distributed neuronal networks [19, 9]. Pinto and Ermentrout studied a single population with synaptic depression using singular perturbation and were able to construct waves by separating the time scale of fast inhibition from slow inhibitory feedback [58].

In the absence of input, the cortex shows many complex spontaneous patterns. Among those which have garnered interest by physiologists are "up" and "down" states. During up states, intracellular recordings of neurons show that they are depolarized, which is due to ongoing synchronous synaptic activity. In [49], multi-electrode recordings reveal that there is a transition from down to up states in the form of a propagating wave; in other words, a wave front. In contrast, there is no such spatially organized transition from up to down states. Inhibition plays a crucial role in the existence of up and down states [64]. Hence, we can not simply propose that the fronts are traveling fronts in a scalar bistable medium [22], but rather, they involve an interplay between the excitatory and inhibitory populations.

In this chapter, we describe a firing rate model for the dynamics of the space-clamped excitatory-inhibitory cortical circuit that, depending on the timescale of the inhibition is either bistable or monostable. We base this circuit on the experimental results of [64] and [57]. We embed the dynamics in a spatially extended system of integro-differential equations in one- and two-spatial dimensions and then analyze the resulting dynamics. In the one-dimensional spatial case, by our choice of spatial weighting functions, we are able to reduce the existence of traveling fronts and pulses to solving a low-dimensional dynamical system. We find that, as the inhibitory time scale increases, there are fronts (heteroclinic orbits) that join the down state to an up state characterized by a spatially-homogeneous fixed point, a bulk oscillation, or a period-doubled, spatio-temporal pattern. For slower inhibition, we show that there are pulses (homoclinic orbits) which bifurcate into periodically modulated waves as the spread of inhibition increases. We combine direct simulation of the spatially discretized systems with numerical continuation of solutions to the corresponding boundary

value problem to understand the transitions and stability of the pulse and fronts. Lastly, we show simulations in two spatial dimensions and close with a discussion of our findings throughout the chapter.

3.2 A SYSTEM OF PARTIAL DIFFERENTIAL EQUATIONS: LOCALIZED INHIBITION

To study traveling waves, we first focus on Eq. (1.1) when there is only localized inhibition, i.e. $\sigma_i = 0$. In this case, the transfer function of the inhibitory dynamics only has spatial-dependence through the excitatory interaction kernels. Then we can convert the partial integro-differential equation to a 4D system of partial differential equations by letting $w = w(x,t) := K_e(x) \star u(x,t)$ denote the convolved excitatory current and taking two partial derivatives with respect to x, to show that w satisfies the second order partial differential equation: $\frac{\partial^2 w}{\partial x^2} = (w-u)/\sigma_e^2$, where $K_e(x) = \frac{1}{2\,\sigma_e} \exp\left(-\frac{|x|}{\sigma_e}\right)$. Then defining $z = z(x,t) := \frac{\partial w}{\partial x}$, we can write the partial integro-differential equation in (1.1), assuming localized inhibition, as

$$\begin{aligned} \frac{\partial u}{\partial t} &= -u + F(a_{ee}\, w - a_{ei}\, v - \theta_e) \\ \tau\, \frac{\partial v}{\partial t} &= (-v + F(a_{ie}\, w - a_{ii}\, v - \theta_i)) \\ \frac{\partial w}{\partial x} &= z \\ \frac{\partial z}{\partial x} &= (w - u)/\sigma_e^2 \ . \end{aligned} \tag{3.1}$$

This is a system of four coupled PDEs. If we include nonlocal inhibition, we can apply the same trick to get six coupled first order PDEs.

In the coming sections, we will explore the traveling wave solution of (3.1) and then follow the orbits of this 4D system embedded in the full 6D system. In the next section, we introduce the traveling wave frame ($\xi = x + \eta\, t$), and the PDEs become ODEs of the same dimension in this coordinate system. The solutions of the 6D system, are approximated through a decomposed shooting method, which decouples the 6D system into a 4D+2D set

of ODEs. This technique allows us to numerically approximate the traveling wave solutions of Eq. (1.1) by a homotopy of solutions from the 4D to the full 6D model when $\sigma_i > 0$, using continuation methods.

3.3 THE TRAVELING WAVE FRAME

In the next sections, we study the two traveling wave solutions to Eq. (3.1): 1. A traveling front solution, where the mean firing rate of E and I populations transitions from a down to up state; 2. A traveling pulse solution, where the E and I populations transiently increase their firing rates, make an excursion around the up state and then decay back to the down state. In particular, we analyze how the inhibitory time constant transitions the system from traveling fronts to traveling pulses. Later, when we consider the fully coupled 6D system, another bifurcation parameter of interest is the spatial length scale of inhibition, which, for $\sigma_e > 0$, without loss in generality can be studied in terms of the relative spatial spread of inhibition to excitation, given by the ratio $\sigma = \sigma_i/\sigma_e$.

These waveforms can be analyzed within the traveling wave frame, given by $\xi = x + \eta\, t$ where $\eta > 0$ is the unknown velocity of the wave. If we suppose solutions of the form $U(x,t) = u(\xi)$, $V(x,t) = v(\xi)$, then $\frac{\partial}{\partial x} = \frac{d}{d\xi}$, and the chain rule yields $\frac{\partial}{\partial t} = \eta\, \frac{d}{d\xi}$. In phase space, the traveling waves correspond to homoclinic (pulse) or heteroclinic (front) orbits; these are trajectories that connect a single equilibrium or two distinct equilibria, respectively, in the limit as $t \to \pm\infty$. Denoting $' = \frac{d}{d\xi}$, we obtain a 4-dimensional system of first-order differential equations:

$$\begin{aligned} \eta\, u' &= (-u + F(a_{ee}\, w - a_{ei}\, v - \theta_e)) \\ (\eta\, \tau)\; v' &= (-v + F(a_{ie}\, w - a_{ii}\, v - \theta_i)) \\ w' &= z \\ z' &= (w - u)/\sigma_e^2 \ , \end{aligned} \tag{3.2}$$

where $\eta > 0$ is the unknown wave speed. There are three fixed points of the system, just as in the space-clamped system, which we denote $(u, v, w, z)_\mu = (\bar{u}, \bar{v}, \bar{u}, 0)_\mu$, where $\mu = 1$ for

the down state, $\mu = 2$ for the saddle point and $\mu = 3$ for the up state. We first consider when $\tau < \tau_{HB}$ and determine parameters for the existence of a traveling front with wave speed $\eta > 0$. This solution corresponds to a heteroclinic orbit which connects the unstable manifold of the down state, $(u, v, w, z)_1 = (\bar{u}, \bar{v}, \bar{u}, 0)_1$ to the stable manifold of the up state, $(u, v, w, z)_3 = (\bar{u}, \bar{v}, \bar{u}, 0)_3$. Hence, the boundary conditions satisfy

$$\lim_{\xi \to -\infty} (u, v, w, z)(\xi) = (\bar{u}, \bar{v}, \bar{u}, 0)_1 \qquad \lim_{\xi \to \infty} (u, v, w, z)(\xi) = (\bar{u}, \bar{v}, \bar{u}, 0)_3 \ . \tag{3.3}$$

The linearization around the down and up states is given by

$$M_\mu = \begin{pmatrix} -1/\eta & -b_{ei}/\eta & b_{ee}/\eta & 0 \\ 0 & (-1 - b_{ii})/(\eta\,\tau) & b_{ie}/(\eta\,\tau) & 0 \\ 0 & 0 & 0 & 1 \\ -1/\sigma_e^2 & 0 & 1/\sigma_e^2 & 0 \end{pmatrix},$$

where $b_{ke} = a_{ke}\,\beta\,\bar{u}\,(1-\bar{u})$ and $b_{ki} = a_{ki}\beta\,\bar{v}\,(1-\bar{v})$, evaluated at the fixed points: $(u, v, w, z)_\mu$, $\mu = 1, 3$. In Appendix B.1, we show that as long as the up state is a stable solution to the space-clamped system in (1.2), then the matrix M_1 has one positive eigenvalue and the remaining three eigenvalues have negative real parts (for all $\eta > 0$). Thus, there is a one-dimensional unstable manifold for the down state equilibrium; this gives us an approximate starting point for our numerical shooting. In addition, we use a homotopy argument (Appendix B.1) to show that M_3 has a one-dimensional unstable manifold and a three dimensional stable manifold.

3.3.1 The Traveling Front: Local Inhibition

In Fig. 14, we approximate the heteroclinic with a one-dimensional shooting method in which we fix $\tau = 0.1$ and then vary $\eta > 0$ to obtain a trajectory (of finite period) that connects to the stable manifold of the up state. We refine this estimate using AUTO [18] by extending the period to a large number (10^4). We then continue in the desired parameter. In Fig. 14A(ii), we show the curve of heteroclinics in (τ, η) parameter space and note that as the inhibition slows down, the wave velocity increases. Intuitively, if the inhibition is slower, then the excitation can increase farther from the down state which gives more excitation

to neighboring excitatory populations before the inhibition gets a chance to kick in. In Fig. 14A(iii), we show several trajectories for various time constants. We note that the heteroclinic orbit has been continued up to τ nearly 1 in Fig 14A(i), which is well past the values of τ for which the up state is stable in the space-clamped system (cf Fig. 2A, where $\tau_{HB} \approx 0.27$, $\tau_{HC} \approx 0.67$).

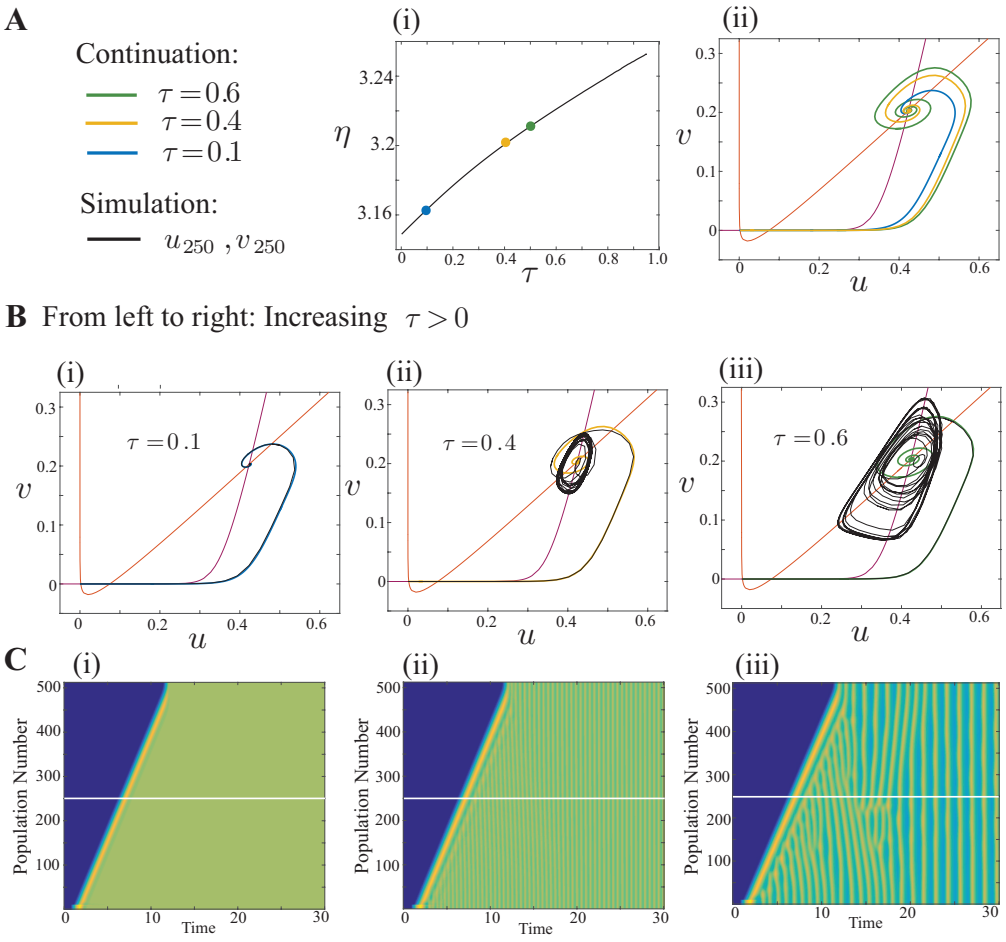

Figure 14: Comparison of traveling front solutions of the boundary value problem and simulations of the discretized network of $N = 512$ excitatory and inhibitory neurons with local inhibitory connections ($\sigma_i = 0$). (A) In panel (i), we continue the traveling front solution with respect to (τ, η) and show in panel (ii) the three different solutions for $\tau = [0.1\,,\, 0.4\,,\, 0.6]$. (B) The u-v phase planes: (i) $\tau = 0.1$: The system tends to the stable up state; (ii) $\tau = 0.4$: The firing rate increases and tends to a spatially-homogeneous limit cycle (bulk oscillation) around the up state; (iii) $\tau = 0.6$: The system moves toward a period-doubled oscillation (spatio-temporal pattern). (C) The three tendencies are shown in the corresponding array plots of the excitatory population firing rates. Horizontal, white lines denote the temporal dynamics projected in (B).

Then in Fig. 14B, we superimpose the simulations of the discretized network with $N = 512$ onto our numerical approximation of the heteroclinic in the u-v phase plane. To initialize the wave in the discretized system, we excite a small portion of the media and then check to see if a wave propagates. We find that the excitation propagates as a traveling front, and for all $\tau < \tau_{HB}$, the numerical shooting and simulations of the full network match well (Fig. 14B(i)). However, when $\tau > \tau_{HB}$ the up state equilibrium is no longer a stable fixed point for the space-clamped system, and this is demonstrated in panels (ii) and (iii) of Fig. 14B,C. In panel (ii), $\tau = 0.4 > \tau_{HB}$ and we observe that instead of joining the down state to a fixed point, as seen in the shooting method, the full spatially discretized system shows a wave that connects the down state to a spatially homogeneous limit cycle. For even larger τ, the full system appears to join the down state to a complex spatio-temporal pattern. Such patterns arise through a period-doubling bifurcation of a spatially homogeneous oscillation, and a detailed stability analysis of these types of spatio-temporal patterns can be found in [32]. Fig. 14A(ii) shows the front velocity only up to $\tau \approx 0.95$, beyond which we were unable to continue the solution. If we choose τ close to 1, then instead of fronts, we see pulses. These will be analyzed in section 3.3.3.

3.3.2 The Traveling Front: Nonlocal Inhibition

By introducing nonlocal coupling of the inhibitory population, the system in Eq. (3.1) increases to a 6D system of first order differential equations given by

$$\begin{aligned}
\eta\, u' &= (-u + F(a_{ee}\, w - a_{ei}\, q - \theta_e)) \\
(\eta\, \tau)\; v' &= (-v + F(a_{ie}\, w - a_{ii}\, q - \theta_i)) \\
w' &= z \\
z' &= (w - u) \\
q' &= r \\
r' &= (q - v)/\sigma^2 \ ,
\end{aligned} \tag{3.4}$$

where q, r are the additional variables to represent the convolution $(K_i \star v)(x)$ as a second order system, and $\sigma = \sigma_i/\sigma_e$ is the relative length scale of inhibition to excitation. Similar

to the 4D system, we write the boundary conditions for the traveling front (with wave speed $\eta > 0$). In the phase plane, this corresponds to a heteroclinic orbit with the following boundary conditions:

$$\lim_{\xi\to-\infty}(u,v,w,z,q,r)(\xi) = (\bar{u},\bar{v},\bar{u},0,\bar{v},0)_1 \qquad \lim_{\xi\to\infty}(u,v,w,z,q,r)(\xi) = (\bar{u},\bar{v},\bar{u},0,\bar{v},0)_3 \tag{3.5}$$

The linearization of the full 6D system in Eq. (3.4) around the down and up states is given by

$$M_\mu = \begin{pmatrix} -1/\eta & 0 & b_{ee}/\eta & 0 & -b_{ei}/\eta & 0 \\ 0 & -1/(\eta\,\tau) & b_{ie}/(\eta\,\tau) & 0 & -b_{ii}/(\eta\,\tau) & 0 \\ 0 & 0 & 0 & 1 & 0 & 0 \\ -1 & 0 & 1 & 0 & 0 & 0 \\ 0 & 0 & 0 & 0 & 0 & 1 \\ 0 & -1/\sigma^2 & 0 & 0 & 1/\sigma^2 & 0 \end{pmatrix},$$

where $b_{ek} = a_{ek}\,\beta\,\bar{u}\,(1-\bar{u})$ and $b_{ik} = a_{ik}\beta\,\bar{v}\,(1-\bar{v})$. In Appendix B.1, we show that the down state has a two-dimensional unstable subspace and a four-dimensional stable subspace. We also show that if the up state is an equilibrium of the space-clamped system in (1.2), then the dimensions of the stable and unstable subspaces are the same as those of the down state. Since the unstable space has a dimension greater than one, the numerical shooting is more difficult to implement than in the 4-dimensional ODE. More precisely, in the case of 4-dimensions, only one parameter (e.g. η) needs to be varied to approximate the heteroclinic and homoclinic orbits, while in the present case of 6-dimensions, two parameters (e.g. η and another parameter to adjust the angle along the two-dimensional unstable subspace) must be varied.

We thus use numerical solutions of the 4D system in Eq. (3.2) to shoot in the higher dimensional system in which the variables q, r are decoupled from the dynamics of the 4D system (but not vice-versa). From this we can obtain a decent approximation for the solution of Eq. (3.4) when $0 < \sigma_i << 1$. We then perform a homotopy from one system to the next using numerical continuation of a parameter, say λ, from 0 to 1, where $\lambda = 0$ gives the solution of Eq. (3.2) and $\lambda = 1$ gives the solution to Eq. (3.4) when the inhibitory population has nonlocal, spatially-distributed connections. We illustrate this homotopy method in

Fig. 15 and provide further explanation of this procedure along with detailed equations in Appendix B.2.

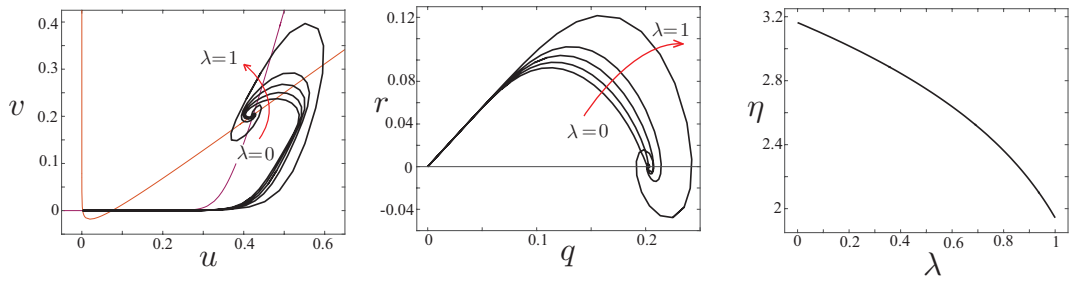

Figure 15: A homotopy of heteroclinic solutions: Increasing $\lambda = [0, 0.2, 0.4, 0.6, 0.8, 1]$ to go from the localized solutions to nonlocal solutions. Compare the orbits when $\lambda = 0$ to Fig. 14B(i) and $\lambda = 1$ to Fig. 16B(i).

Figure 16A depicts the velocity of the traveling front solutions to Eq. (3.4) when both excitation and inhibition have nonlocal, spatially-distributed connections. In Fig. 16A(i), we fix $\sigma = 0.8$ and vary τ against η. Then in Fig. 16A(ii), we plot the curve of fronts in (σ, η) parameter space for fixed values of $\tau = [0.1\,,\, 0.35\,,\, 0.5]$ and see that as σ increases, the velocity of the traveling front tends to zero. Moreover, the velocity monotonically decreases with increasing spatial spread of inhibition which means that the longer reach of inhibition more strongly suppresses excitation of the down state. This extends the onset of the pulse, which slows propagation of the wave. The behavior of the velocity as τ varies, shown in Fig. 16A(i), is qualitatively the same as in Fig. 15A(i); it is just slower as expected from Fig. 16A(ii).

In Fig. 16B, we let $\sigma = 0.8$ and find transitions which are similar to those found in Fig. 15B. For $\tau = 0.1$, the up state is stable and we see a transition of the system from the down state to the up state. As we increase τ to 0.4, a limit-cycle emerges around the unstable fixed point for the space-clamped system. Despite this, the curve of traveling fronts continues in (τ, η) space, so in Fig. 16B(ii) and (iii), we superimpose network simulations of the discretized spatial system onto numerical solutions and project them in the u-v phase plane. Since the spatially uniform up state is unstable, the network tends to a bulk oscillation

similar to the limit-cycle depicted in Fig. 2A. When $\tau = 0.5$, the spatially homogeneous oscillation is unstable and the system tends to a spatio-temporal pattern, which can be seen by the excitatory array plot in Fig. 16C(iii). Thus, we see that the effect of spatial connectivity of the inhibition has little qualitative effect on the form of the waves, both in the shooting and the full simulation. However, we note that the velocity is very strongly dependent on σ with the maximum effect occurring around $\sigma = 1$. That is, the velocity of the wave is very sensitive to the lateral connectivity of the inhibitory neurons when that connectivity has roughly the same spatial spread as the excitatory population. For nonlocal inhibition, the transition from the down state to a spatio-temporal patterned up state at higher values of τ is much more apparent than in the purely local inhibition case. Compare Figures 15C(iii) and 16C(iii). Interestingly, the shooting correctly predicts the velocity of the transition from the down state to the up state in the full simulation even though the steady state dynamics of the simulation are not spatially or temporally uniform. We suspect that the traveling wave that joins the down state to the up state (found through shooting) is unstable as a solution to the full integral equations. That is, while the front exists, it is not stable. In spite of the instability, the heteroclinic orbit provides an excellent estimate of the velocity for the down to up state activation.

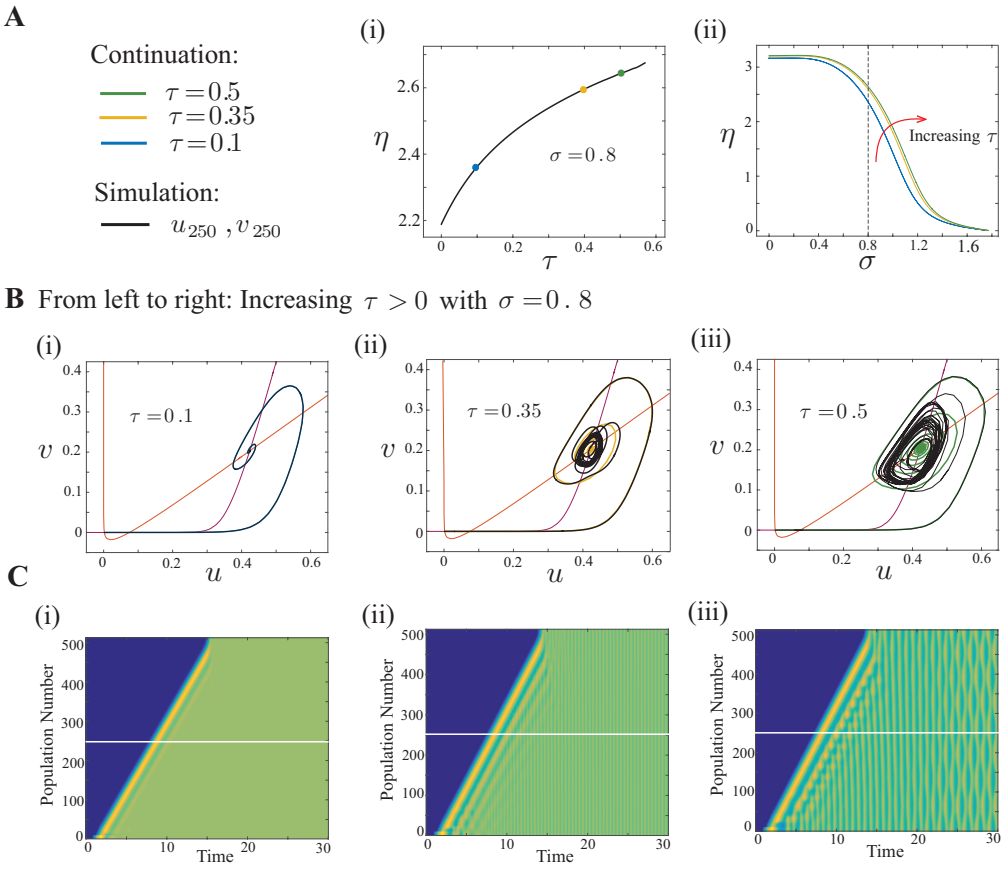

Figure 16: Comparison of traveling front solutions of the boundary value problem with simulations of the discretized network of ($N = 512$) excitatory and inhibitory neurons with nonlocal inhibitory connections ($\sigma_i > 0$). (A) The curve of heteroclinic orbits of the 6D system: (i) $\sigma = 0.8$ in (τ, η); (ii) $\tau = [0.1\,,\ 0.35\,,\ 0.5]$ in (σ, η) parameter space. (B) Numerical solutions and simulations in the u-v phase plane, increasing τ from left to right: (i) $\tau = 0.1$, (ii) $\tau = 0.35$, (iii) $\tau = 0.5$. (C) Space-time plot of the excitatory population firing rates for parameters in (B).

3.3.3 The Traveling Pulse: Nonlocal Inhibition

As we noted in section 1.3, when τ is large enough, there are no attractors around the up state and, so, excursions away from the down state return to the down state. Thus, we will now look for traveling pulse solutions to Eq. (3.4). These can be constructed in the same manner as for the traveling front, i.e. by starting with the 4D system in Eq. (3.2) and then performing a shooting method to obtain solutions of the fully connected 6D system. When τ is sufficiently large, the space-clamped system is an excitable medium; that is, there is a unique globally stable down state but sufficient perturbations cause a transient excitation before decaying back to the down state. Traveling pulse solutions are often found in spatially distributed excitable media [58, 3, 1], so it is natural to look for such solutions in our network. Thus, in this and the next few sections, we will study the properties of traveling pulses.

Here, we increase the time constant of inhibition, $\tau > \tau_{HC} = 0.6764$, and look for a pulse solution satisfying the boundary condition,

$$\lim_{\xi \to \pm\infty} (u, v, w, z, q, r)(\xi) = (\bar{u}, \bar{v}, \bar{u}, 0, \bar{v}, 0)_1 \ .$$

In our analysis of the traveling pulse, we are interested in how the spatial (σ) and temporal (τ) scales affect the speed of the traveling wave as well as the stability. In Fig. 17A(i), we fix τ and continue the orbit with respect to σ. (In a subsequent section, we will fix σ and continue with respect to τ as this enables us to see the transition from fronts to pulses.) Here, we note that the speed monotonically decreases with respect to σ, which means that as the spread of inhibition increases, the wave slows down. As with fronts, the reason for this is that the inhibitory population can reach longer range relative to the excitatory, which slows the increase in firing rate of excitation during propagation. Moreover, the curves in (σ, η) parameter space with larger τ lie above those with smaller τ, so as with fronts, slowing the inhibition speeds up the wave. This can be explained by the fact that activation occurs through feedforward excitation of neighboring excitatory populations and is quenched by the tracking inhibition. Hence, inhibition releases excitation to spread, but a larger time scale of inhibition, means inhibitory tracking is slower in turning off excitation. In addition, we observe in Fig. 17A(ii) and (iii) that the amplitude of the pulse increases with larger τ and larger σ.

In Fig. 17B, we plot the pulse trajectory in the u-v phase plane for fixed $\tau = 2$ and increasing σ to compare the trajectory from shooting (blue, yellow, green) with network simulations (black). We note that for small σ the simulations and the shooting match exactly, as in Fig. 17B(i), but there is an increasing discrepancy with larger values of σ, as shown in Fig. 17B(ii),(iii). This can be explained by looking at Fig. 17C where we show the full space-time plots of the excitatory firing rate for these same three values of σ. What appears to happen is that at higher values of σ (specifically, $\sigma > 1$) an instability of the pulse occurs that seems to be periodic in the traveling frame. Thus, the width of the pulse is not constant over time, and this appears to account for the discrepancy seen in Fig. 17B(ii),(iii). This type of pulse is often called a breather [26], or, a saltatory or lurching wave [30, 10].

To better see the periodic orbit, we can make a coordinate change along the line $y = x + \eta\, t$ for the space-time arrays in Fig. 17C. These types of waves are not simply similarity solutions, as in regular traveling wave solutions, but rather, they have additional temporal dynamics. Specifically, we observe oscillations of the activated region even when transformed to the moving frame by subtracting the mean velocity of the pulse (Fig. 18B). In Fig. 18C, we see these oscillations grow with increasing σ, which indicates that the oscillation goes through a bifurcation similar to the Hopf bifurcation for a fixed point. Though the oscillatory instability to the traveling wave is apparent in the discretized simulations, continuation of the pulse solution in the wave frame gives no indication. Instead, we see from Fig. 17A that the curves and orbits continue to exist, leaving from the unstable manifold and returning to the stable manifold of the down state. That is, while regular traveling pulses continue to exist, they appear to lose stability as σ increases. We note that this instability occurs over a limited range of values of τ and σ. If τ is large, then the wave appears to just die out as σ increases, while if τ is too small, then there is no pulse. Intuitively, the mechanism for lurching can be explained as follows: The larger time scale of inhibition allows for the wave to propagate quickly but the longer reach of inhibition staunches this propagation, slowing the wave down and reducing the total excitation. However, the diminished excitation and increased recurrent inhibition to the inhibitory network diminishes the inhibition, allowing the excitation to once again build up and push the wave forward.

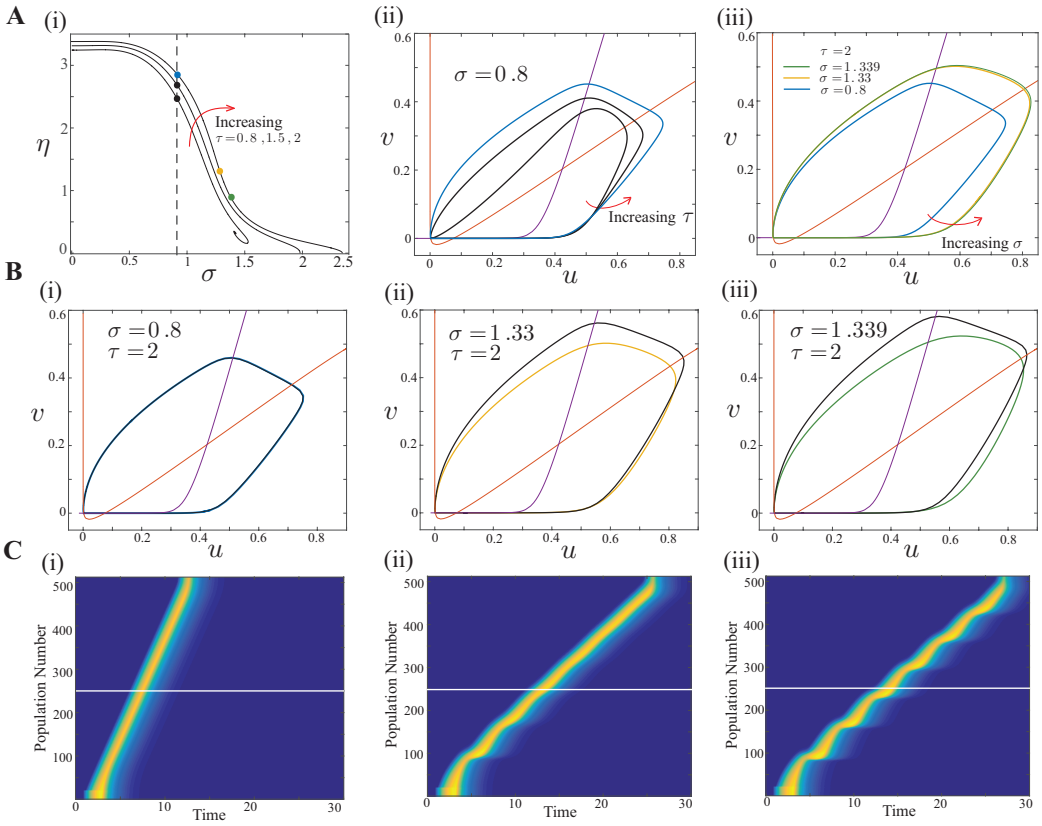

Figure 17: Comparison of traveling pulse solutions of the boundary value problem and simulations of the discretized network of $N = 512$ excitatory and inhibitory neurons with nonlocal inhibitory connections ($\sigma_i > 0$). (A) (i) The velocity (η) of the pulse solutions as σ varies for several different values of the inhibitory time constant: $\tau = [0.8, 1.5, 2]$. (ii) Excitatory-inhibitory (u, v) firing rates of population for $\sigma = 0.8$ and $\tau = [0.8, 1.5, 2]$, corresponding to intersections of the vertical dashed line in panel (i). (ii) Excitatory-inhibitory (u, v) firing rates corresponding to the dots in panel (i) for $\tau = 2$ and $\sigma = [0.8, 1.33, 1.339]$. (B) Numerical solutions and simulations in the u-v phase plane when $\tau = 2$ and increasing σ from left to right: (i) $\sigma = 0.8$, (ii) $\sigma = 1.33$, (iii) $\sigma = 1.339$. (C) Space-time plot of the excitatory population firing rates for parameters in (B).

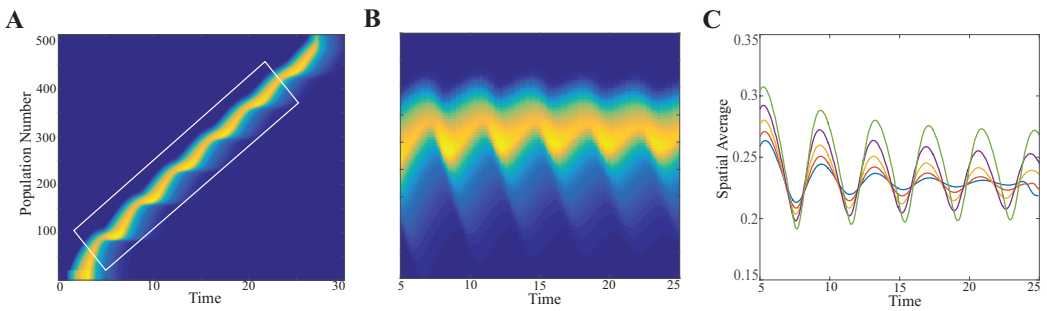

Figure 18: Domain-straightening of the lurching wave to show the oscillatory instability as σ increases. (A) Array plot of the excitatory population firing rates when $N = 512$, $\sigma_e = 15$ and σ_i is such that $\sigma = 1.339$ as in Fig. 17.C(iii). (B) We estimate the speed and make a change of coordinates to transform the activated region enclosed in the rectangle shown in (A). (C) A spatial average of panel (B) gives a smooth oscillation with amplitude that grows with increasing $\sigma = [1.3, 1.31, 1.32, 1.33, 1.339]$.

3.4 STIMULUS-DEPENDENT ACTIVATION

In Fig. 16, we see that for $\sigma = 0.8$ there exists a traveling front up to about $\tau = 0.6$, while in Fig. 17A(i), there are pulses for at least $\tau = 0.8$, and so, we try to understand how the waves make the transition from fronts to pulses as τ varies. Indeed, τ is a natural parameter to study as it determines the stability of the up state in the space-clamped system. Figure 19A shows a plot for the continuation of the front (solid) and the pulse (dashed) at $\sigma = 0.8$. The front continuation terminates near the homoclinic bifurcation for the space-clamped system as does the pulse. The velocity of the traveling solutions seems to be continuous as the dynamics pass from the front to the pulse. We note that for $\tau > \tau_{HB}$, the front is unstable (cf. Fig. 16B), but the velocity matches the velocity of the front that joins the down state to the up state attractor. If we choose a value of τ near the transition point (shown by the dotted line, $\tau = 0.68$) and briefly excite a local region in the spatially discretized network, we observe that there are two kinds of attractors depending on the strength of the stimulus: Front-like (longer lasting stimuli) and pulse-like (shorter lasting stimuli) dynamics.

This is shown in Fig. 19C,D. The pulses appear to reflect off the boundaries so that in a semi-infinite domain, we would not expect to see the reflection. In Fig. 19B, we show the temporal evolution of these two distinct waves at two spatial locations. The front is shown by the orange and blue curves and the pulse by the black curves. The temporal evolution of the front and pulse solutions look identical up until a point where the pulse drops back to the down state, but the front continues to evolve, in this case, to a spatio-temporal pattern.

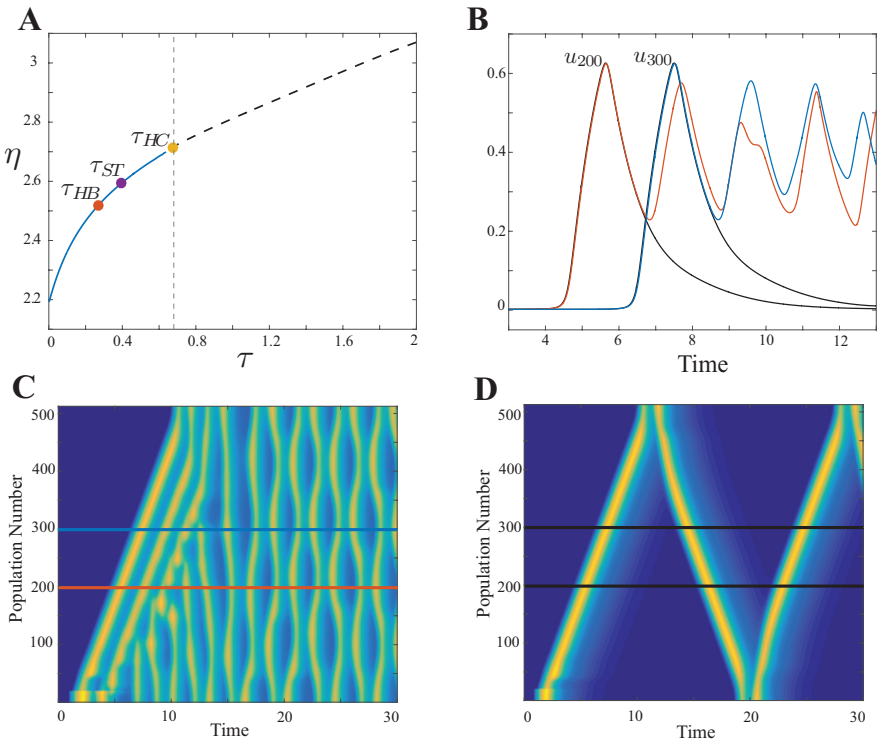

Figure 19: Bistability near the transition from fronts to pulses. (A) Continuation of the front (solid line) and the pulse (dashed line) as the relative time scale of inhibition, τ varies for $\sigma = 0.8$. The values of τ that characterize the onset of the Hopf bifurcation (HB), spatio-temporal patterns (ST), and a homoclinic (HC) are indicated. (B) Temporal evolution of a front (orange, blue) and a pulse (black) at two different spatial locations for $\tau = 0.68$. (C, D) The front and the pulse in a space-time plot of the excitatory firing rate. The pulse is evoked by a stimulus lasting 1 time unit and the front, by a stimulus lasting 2.5 time units.

3.5 TRAVELING WAVES IN THE 2D MODEL

Thus far, we have only considered the Wilson-Cowan equations on a one-dimensional spatial domain to analyze how the speed and stability of the wave depend on the temporal and spatial length scales of the system. Next, we consider a two-dimensional spatially-distributed network with kernels that decay with the Euclidean distance. Here we take the kernel to be the decaying exponential,

$$K_j(\sqrt{x^2+y^2}) = \frac{1}{2\,\pi\,\sigma_j^2}\,\exp\left(-\frac{\sqrt{x^2+y^2}}{\sigma_j}\right) \quad , \quad j \in \{e,\, i\}\ .$$

We can use the curves in Figures 16 and 17 to find parameters where we might expect traveling waves in the system. To simulate the 2D spatially connected network, we create an array of 256 by 256 excitatory and inhibitory neurons with reflecting boundary conditions. We impart an initial localized stimulus and present the resulting numerical solutions in Fig. 20 as a series of five frames over equal time intervals to show the propagation. We fix $\tau_e = 1$ and $\sigma_e = 10$ and choose three different pairs of values for τ_i and σ_i to represent the three different behaviors of the up state. In Fig. 20A, the up state is a stable equilibrium, and the outwardly moving front eventually goes to a spatially uniform constant solution. In Fig. 20B, parameters are such that the up state has a stable homogeneous oscillation and the asymptotic state of the 2D system is a spatially uniform bulk oscillation. Finally in Fig. 20C, parameters are chosen so that there is a symmetry breaking instability of the uniform oscillation in the up state and the wave transitions to that state. See the supplemental movie for a clearer picture.

In Fig. 21A, we increase τ to 2 so that a stable pulse exists for $\sigma = 0.9$. An outwardly traveling pulse appears which meets with the boundary and leaves the system back at the down state. We then increase the spatial scale of inhibition (as in Fig. 18C) to look for "lurching" waves in the 2D system. In Fig. 21B, we stimulate from the upper left corner of the media (instead of the center) to show how the band of excitation propagates with varying width. From $t = 4$ to $t = 6$, the band of excitation contracts as inhibition catches up, and then from $t = 6$ to $t = 8$, it expands as feedforward excitation progresses the wave. This lurching behavior is better seen in a space-time plot of the excitatory populations along

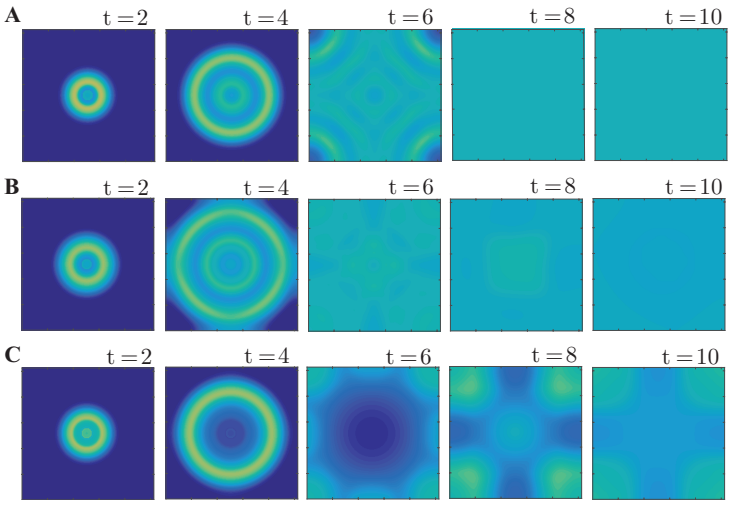

Figure 20: Traveling fronts in the 2D spatially-distributed network (256×256) initiated by disc-shaped stimuli of radius 10 spatial units about the center of the media. We set $\sigma_e = 10$, $\tau_e = 1$ and show the excitatory population firing rates as a sequence of equal time frames for $\sigma = 9$ and three values of the inhibitory time constant: (A) $\tau_i = 0.1$; (B) $\tau_i = 0.4$; (C) $\tau_i = 0.6$.

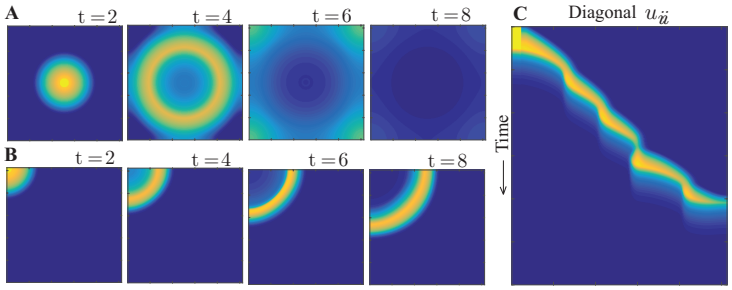

Figure 21: Traveling pulses in the 2D spatially distributed network (256×256), setting $\sigma_e = 10$, $\tau_e = 1$, $\tau_i = 2$. We show the excitatory population firing rates as a sequence of equal time frames: (A) The regular traveling pulse for $\sigma_i = 9$; (B) The lurching pulse initiated in the corner for $\sigma_i = 14.5$. (C) Space-time plot along the diagonal of (B) to better illustrate the lurching behavior.

the diagonal of the domain in panel B, which is displayed in Fig 21C. In the cases where we impart a center-stimulus, we note that the outward propagation of the waves in 2D is radially symmetric in both the front and pulse simulations. Thus, it is possible to reduce the 2D system to a 1D system in order to better explore features like the velocity and magnitude of the waves. We briefly explain how to do this in Appendix B.4.

3.6 DISCUSSION

Traveling waves in nonlocal media has been the object of a great deal of mathematical and computational study. In the context of cortical networks, experimentalists have used the waves to say something about the local circuitry of the network and have also suggested some roles for waves in sensory processing [77, 42]. Waves arise when active space-clamped dynamics interact in a spatially localized manner. In almost all the studies of waves in neural fields, the space-clamped dynamics is either bistable or excitable; in the former case, the models are scalar with just a population of excitatory cells and in the latter, the space-clamped dynamics generally has a single equilibrium point. In this chapter, we have considered a different type of active medium for which there are three spatially homogeneous equilibria–one of which is on the middle branch of the excitatory nullcline, which means that it is conditionally stable. This state (called the inhibitory stabilized state [57, 74] or up state) has been found to have many interesting computational features. Thus, we have focused our attention on waves that join the down state to this up state and how their existence depends on the stability of this state. We exploited the exponential nature of the connectivity kernels in order to reduce the study of traveling waves to finding heteroclinic and homoclinic orbits to a 4 or 6 dimensional set of ODEs. For such systems, the combination of numerical shooting and continuation with AUTO has allowed us to study how the speed and other properties of the waves depend on the inhibitory time and space scales.

Traveling fronts in the full network correspond to heteroclinic orbits in the ODE system. These fronts take the network from the stable down state to the up state. While we were able to find fronts over a wide range of parameters, simulations in the discretized spatial

network showed that the front did not always settle onto the up state equilibrium. Instead, as the time course of inhibition (τ) increases, the up state goes through several bifurcations, and the front joins the down state to more complex dynamics in the up state—first leading to a spatially uniform oscillation and then to a spatio-temporal pattern. In spite of the instability, we found that the velocity determined by shooting closely matched the velocity of the full network simulation. In both the shooting and the simulation, there was a maximum value of τ, beyond which there were no fronts of any kind.

The experiments described in [49] indicate that the transitions of cortical states from down to up are spatially organized into waves, though the transitions from up to down are not. Our results are consistent with these experiments in that we have not found fronts that transition the system from up to down state activity. This is typical for waves in bistable media; they typically only transition in one direction (e.g. up to down or down to up, but not both). We note also that the dynamics in the up state are far richer than in the down state with oscillations and complex spatio-temporal dynamics possible. This richness could endow cortical networks with greater computational capabilities [73] so it makes biological sense for the transition to the up state to be organized.

The traveling pulse corresponds to a homoclinic orbit in the traveling wave frame. As with the traveling front, we compare solutions to the boundary value problem to the 1D simulations of the discretized network. Here, the bifurcation parameter is the spatial scale, $\sigma = \sigma_i/\sigma_e$, and simulations show that the traveling pulse goes through a Hopf-like instability leading to lurching waves. Such waves have been found in stimulus-locked waves in a neural field model with excitation and adaptation [26], wherein the authors determine the instability using an Evans function due to the simple nature of the nonlinearity. Using a similar approach, Folias studied this type of oscillatory instability in standing waves, referring to them as 'breathers' [25]. Instabilities of solitary waves were also analyzed in [30] where there was an explicit delay in the coupling between the neurons. Traveling pulses are a fairly common phenomena in neural tissue, both *in vitro* and *in vivo* [77, 54] as well as in pathological situations [59, 43] where they have been modeled without an inhibitory population of neurons.

We concluded the chapter with some two-dimensional simulations that show radially

symmetric waves. We describe how such waves could be analyzed in Appendix B.4. With appropriate initial conditions, we expect to also observe spiral and rotating waves, which are seen in cortical slices [38] and more recently in human cortex during sleep [53]. The analysis and simulation of these waves remains a topic for further study.

4.0 THE NONSMOOTH WILSON-COWAN EQUATIONS

This chapter is based on [33].

4.1 INTRODUCTION

The Wilson–Cowan (WC) equations represent a common means of studying the dynamics between excitatory and inhibitory populations of neurons. A number of recent experimental papers suggest that the cerebral cortex lies in the so–called inhibitorily–stabilized network (ISN) state which means that there is a stable equilibrium state that intersects the middle branch of the excitatory nullcline [57]. A commonly used simplification replaces the smooth firing rate function with the step function. In this chapter, we explore the consequences of the nonsmooth approximation on the dynamics for WC systems that have such a middle–branch equilibrium in their smooth analogue. In the nonsmooth system, the inhibitory stabilized state corresponds to a *pseudo focus* (or *focal crossing*) occurring at the intersection of two *switching manifolds*—the subject of current work in nonsmooth systems theory. To study the dynamics we introduce and use techniques from Filippov systems and differential inclusions. We show nonsmooth equivalents of the Hopf, saddle–node on an invariant circle, and homoclinic bifurcations. We then compare these solutions with trajectories of the smooth system to show a similar qualitative but differing quantitative bifurcating behavior. In addition, we present several nonstandard bifurcations, such as *linear sliding modes*, *tangencies*, and *grazing solutions*, that arise as a result of the discontinuities in the system.

Mathematical neuroscientists have studied some of the more classical neural models by approximating nonlinear functions (prescribed in the model) with nonsmooth functions. For

instance, the McKean model simplifies the FitzHugh–Nagumo equations by replacing the cubic polynomial reaction function with a piecewise linear (pwl) function, having three pieces. The second caricature is a limiting case of the first, for which the slope of the middle branch goes to infinity, so that $f(u) = -u + H(u - a)$, where $0 < a < 1$ and H is the Heaviside step function ($H(u) = 0, u < 0$ and $H(u) = 1, u > 0$) [51]. Tonnelier revisits the McKean caricature in two recent publications: In [70], he studies the pulse traveling wave solutions in a diffusion model, writing asymptotic expressions for the wave and wave speed; in [69], he shows analytical expressions for spiking solutions and limit cycles in a space clamped system. More recently in [60], Rotstein and Coombes made a similar simplification of the FitzHugh–Nagumo equation, taking a piecewise linear function with four linear pieces, in order to study the small amplitude oscillations and Canard explosions that arise. In Section 4.6, along with the smooth, logistic system, we analyze the (continuous) nonsmooth, pwl system.

In [76], Wilson and Cowan derive and analyze the interacting dynamics of localized excitatory and inhibitory population, and since then, neural field models have been extended to include spatial interactions that produce a variety of spatial patterns. In order to facilitate the analysis of these patterns, the firing rate function has often been approximated by the Heaviside step function. For examples of such an approximation, see [1], [9], and [58] in their analysis of activity patterns of synaptically coupled neuronal networks in a single spatial dimension. In these papers, the dynamics of the solutions tend to be similar to their numerically determined smooth analogues, since they avoid regimes where the argument of the step function vanishes. Here, we show that even in the simple two–variable discontinuous WC model, the dynamics can be quite complicated and different from the smooth analogue. The complexity, as we will see, arises from the fact that there is an interior equilibrium point necessitated by the ISN.

In this chapter, we concern ourselves with transitions and bifurcations of the two-dimensional nonsmooth Wilson–Cowan equations with the Heaviside step function as the firing rate. Some of the bifurcations are quite similar to the smooth case, while others arise as a consequence of jump discontinuities in the vector field. These types of bifurcations are termed discontinuity–induced bifurcations (DIBs) in the nonsmooth systems literature. To

supplement the more classical dynamical systems theory, we introduce Filippov systems and differential inclusions, which will be useful for later bifurcation and geometrical phase plane analysis.

4.2 PRELIMINARY DEFINITIONS

To help with notation in mathematical definitions, consider the generic nonsmooth autonomous system,

$$x' = \begin{cases} f_1(x) \ , & h(x) > 0 \\ f_2(x) \ , & h(x) < 0 \ . \end{cases}$$

Typically, $f_1 \, , f_2 : \mathbb{R}^n \to \mathbb{R}^n$ and $h : \mathbb{R}^n \to \mathbb{R}$ are smooth functions. Note that, by writing the above nonsmooth system, we have already implicitly assumed that there is a single manifold of nonsmooth incidence. This does not have to be the case, and in fact, is not for the system studied in this manuscript. This brings us to our first definition:

Definition 1. A *Switching Manifold* is a manifold (typically smooth) that is implicitly defined by the zero level set $\Sigma := \{x \in \mathbb{R}^n | \ h(x) = 0\}$. This is a geometric description of the set of nonsmooth or discontinuous points of the system.

In this chapter, we use the term *switching boundary* interchangeably with *switching manifold*. Next we define a type of trajectory that hits the switching boundary and cannot leave due to the vector fields on either side. At the switching boundary, the dynamics are ambiguous. The *Filippov Method* is a means of resolving this ambiguity by approximating the dynamics along the boundary with a convex combination of the vector fields on either side [23].

Definition 2. A *(linear) sliding mode* is a solution that moves along the switching boundary Σ and exists with sliding dynamics given by the convex combination

$$f_{1,2}^{sl} := \alpha \, f_1 + (1 - \alpha) \, f_2 \ ,$$

with $\alpha \in [0,1]$ such that the normal to the switching manifold is orthogonal to the sliding dynamics, i.e.

$$\nabla h \cdot f_{1,2}^{sl} = 0\,,$$

where $\cdot$ denotes the inner product.

The above definition is actually one for linear sliding, and though the concept of linear sliding has been generalized to nonlinear sliding modes by Jeffrey in [39], we will restrict our attention to linear sliding. Filippov's convex method is especially important when studying these solutions, as the method gives necessary conditions for there to exist linear sliding modes and a clear way of determining the stability of such solutions [23]. A necessary condition, of course, is that $(\nabla h \cdot f_1)\,(\nabla h \cdot f_2) < 0$. That is, projections of the vector fields f_1 and f_2 onto the normal to the switching manifold must have opposite signs. Hence the stability is determined by the projective configuration, which leads to the following more colloquial definition for *attractive* and *repulsive* sliding modes.

Definition 3. A sliding mode is said to be *attractive (repulsive)* if solutions tend toward (away from) the boundary.

Note that this definition can be made completely rigorous by looking at the inner product of the normal vector to the switching manifold with the vector fields f_1 and f_2. Jeffrey gives a rigorous treatment for the stability of sliding modes, by deriving a differential equation for α. Linearizing the α dynamics about the sliding mode, he recovers the stability conditions given by Filippov [39].

Definition 4. A *pseudo equilibrium* is a point x_0 such that

$$\begin{aligned} \alpha\, f_1(x_0) + (1-\alpha)\, f_2(x_0) &= 0 \\ h(x_0) &= 0 \end{aligned} \tag{4.1}$$

for α given by the sliding mode in Definition 2.

A pseudo equilibrium is a point in the switching manifold at which the Filippov derivative is zero. Definition 4 was given by di Bernardo et al. in [14], who make a distinction between *admissible* ($\alpha \in [0,1]$) and *virtual* ($\alpha > 1$ or $\alpha < 0$) pseudo equilibria . In our analysis of a *pseudo heteroclinic* orbit (Definition 5), we observe that a pseudo equilibrium transitions

from admissible to virtual as one of the parameters in our model increases through a critical value. Just as we may define pseudo equilibria, we define special orbits in a similar way.

Definition 5. *Pseudo heteroclinics* connect two equilibria (at least one of which is a pseudo equilibrium) and *pseudo homoclinics* are solutions that tend to a single pseudo equilibrium, both forward and backward time.

Another interesting feature of Filippov systems comes about from the linear sliding modes. Note that if a sliding mode is attractive in one time direction, it will be repulsive in the other time direction. An attractive sliding mode may pass through a point for which $\alpha = 0$ or $\alpha = 1$. Hence the vector field is tangent to the manifold here. If we were to start from this initial condition and evolve backward in time, the sliding mode is repulsive and solutions are non–unique [14].

Definition 6. A *grazing solution* is a trajectory that touches the switching manifold at a tangency. In [15], di Bernardo et al. define a grazing bifurcation in terms of four conditions. The first three are the tangency conditions, while the last one, which is $\frac{d^2}{dt^2}\, h(x(t))|_{t=0} > 0$ evaluated at the tangency $x(0)$, ensures the same curvature (on either side of the tangency) with respect to the switching manifold.

A nice three dimensional example illustrates a grazing bifurcation in a paper by di Bernardo et al. on normal form grazing in piece–wise smooth systems [15]. Kuznetsov et al. present several one parameter bifurcations of a planar system for which equilibria (or solution trajectories) collide with (or graze) the switching manifold [46]. Furthermore, they introduce the notion of *visible* and *invisible* tangencies in planar systems which differ in their concavity with respect to the tangent line of the switching manifold. As their name suggests invisible tangent points do not appear in the nonsmooth phase space, but can be observed if the appropriate vector field is extended past the boundary [13, 46]. Jeffrey gives some nice illustrations of the three dimensional geometry of various types of invisible and visible sliding–grazing bifurcations [40].

We put the two–dimensional firing rate model in a parameter regime for which there is one *true* stable fixed point (the quiescent state) and two *pseudo* fixed points (the pseudo saddle and the inhibitory–stabilized state). The middle equilibrium is a pseudo saddle with

a stable manifold that acts as a threshold for excitability. The inhibitory–stabilized state corresponds to a focal crossing occurring at the intersection of two switching manifolds. Neural networks sitting at the inhibitory-stabilized state may show differing responses to sensory input, depending on the time constant of inhibition and the size and direction of the perturbation. By direction, we refer to the (u, v) phase plane and in terms of the model, this can be interpreted as how the stimulus is distributed across the network. For instance if an excitatory input is localized to E–cells, trajectories may move away from the ISN for large enough time constant of inhibition. For a certain range of τ, trajectories tend to stable limit cycles and for even larger time constant of inhibition, perturbations of the ISN state tend to the stable equilibrium at the origin.

In our analysis, we often numerically solve an appropriate boundary value problem (see Appendix C) and use continuation methods in order to show a variety of solutions and bifurcations, which include: a pseudo Hopf Bifurcation; a pseudo saddle–node on an invariant circle (SNIC) bifurcation; linear sliding modes (using Filippov's Convexification Method); and a visible grazing solution near a homoclinic bifurcation which establishes non–uniqueness with respect to the forward time direction. Thus we find many interesting dynamics and bifurcations of this two dimensional E-I system of Wilson Cowan equations which we will refer back to in Chapter 5 where we study waves in the spatially-extended system.

4.3 THE WILSON-COWAN EQUATIONS WITH HEAVISIDE FIRING RATE

To simplify notation, we write the Wilson-Cowan equations in such a way that the recurrent excitation to the network (for both E and I cells) and the excitatory time constant are normalized to one. By appropriate rescaling of time and renaming of parameters, one can show there is no loss in generality in writing,

$$\begin{aligned} u' &= -u + H(u - a\,v - b) \\ \tau\,v' &= -v + H(u - c\,v - d)\ . \end{aligned} \tag{4.2}$$

The parameters a and c govern the inhibitory connections relative to excitatory, and b and d are the relative thresholds to E and I populations, respectively. In our analysis, we let parameters have the relation $a > c$ and $b < d$. Typical values are $a = 2$, $b = 0.05$, $c = 0.25$, and $d = 0.3$ throughout. With this choice of parameters we have one true and two pseudo equilibria. From Eqn. (4.3), we see the discontinuities occur when the argument of the Heaviside function vanishes. Hence, define the functions $g : \mathbb{R}^2 \to \mathbb{R}$ and $h : \mathbb{R}^2 \to \mathbb{R}$, by

$$g(u, v) := u - a\,v - b\ , \quad h(u, v) := u - c\,v - d\ .$$

Then we can define the switching boundaries—which are simply lines in the plane —in terms of these functions:

$$\Sigma = \{(u, v) \in \mathbb{R}^2 |\ v = (u - b)/a\} = \{g(u, v) = 0\} \tag{4.3}$$

$$\Gamma = \{(u, v) \in \mathbb{R}^2 |\ v = (u - d)/c\} = \{h(u, v) = 0\}\ . \tag{4.4}$$

We often refer to Σ and Γ as the u–switching boundary ($g = 0$) and the v–switching boundary ($h = 0$), respectively, to remind the reader which variable has discontinuous derivative when passing through this manifold.

Parameter values are such that the nullclines and switching boundaries take the form shown in Fig. 22. The true u-nullclines occur at $\{u = 0\} \cap \{g(u, v) < 0\}$ and $\{u = 1\} \cap \{g(u, v) > 0\}$. The true v-nullclines are $\{v = 0\} \cap \{h(u, v) < 0\}$ and $\{v = 1\} \cap \{h(u, v) > 0\}$. These are represented by solid lines in Fig. 22. We define four regions of the plane, denoted by R_1 to R_4, which have smooth vector fields and are separated by the switching boundaries (dashed lines) defined in Equations (4.3) and (4.4). Hence, we can succinctly define the regions in terms of the functions g and h as follows:

$$\begin{aligned}
R_1 &:= \{v \geq 0\ ,\ g \geq 0\ ,\ h \leq 0\} \\
R_2 &:= \{0 \leq u \leq 1\ ,\ v \geq 0\ ,\ g \geq 0\ ,\ h \geq 0\} \\
R_3 &:= \{0 \leq u \leq 1\ ,\ 0 \leq v \leq 1\ ,\ g \leq 0\ ,\ h \geq 0\} \\
R_4 &:= \{0 \leq u \leq 1\ ,\ 0 \leq v \leq 1\ ,\ h \leq 0\ ,\ g \leq 0\}\ .
\end{aligned}$$

We remark that the regions are subsets of the unit square $[0, 1] \times [0, 1]$. This is an important feature of the model, for it eliminates runaway activity in the system. Based on the

qualitative dynamics, we can see that $[0,1] \times [0,1]$ is positively invariant with respect to the piecewise linear flow in (4.3). That is, if a trajectory starts in the unit square all trajectories stay in the unit square for all $t \geq 0$. For instance, take $(u_0, v_0) \in R_2 \cap \{(u,v) \,|\, u = 1\}$. Then $u' = 0$ and $v' > 0$, and the trajectory rides along the u–nullcline till it enters region R_3, at which point $u' < 0$ and $v' > 0$. Hence, the solution moves away from the boundary. Similar arguments can be made for the other boundaries, so we may restrict our analysis to the unit square.

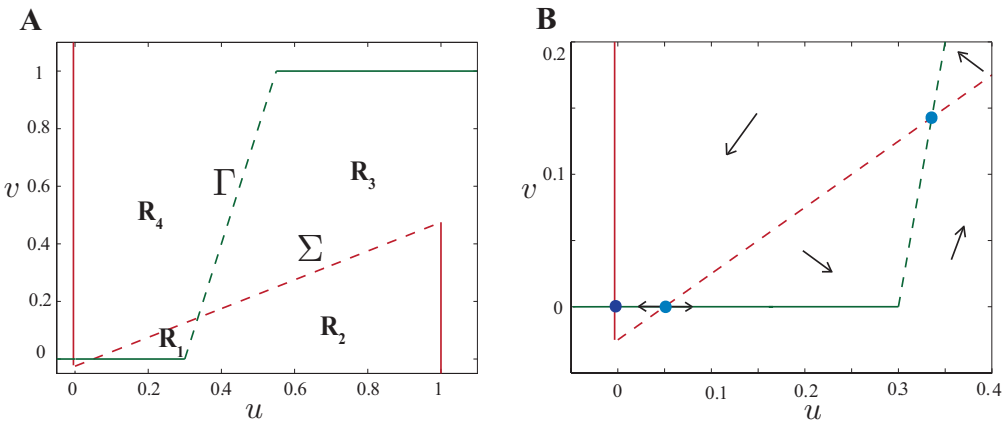

Figure 22: The u, v phase plane with nullclines (solid) and switching boundaries (dashed). (A) The vector field is piece–wise smoothly defined on the four regions R_1 to R_4 as labeled. (B) The phase plane is magnified around the fixed point (dark blue) and pseudo fixed points (light blue) with arrows depicting the qualitative direction field on each region.

4.3.1 The Filippov System

We now present the discontinuous system given in Equation (4.3) as a Filippov system.

$$\begin{pmatrix} u \\ v \end{pmatrix}' \in F(u,v) := \begin{cases} f_1(u,v)\,, & (u,v) \in R_1 \\ \overline{co}\{f_1,\, f_2\}\,, & (u,v) \in R_1 \cap R_2 \\ f_2(u,v)\,, & (u,v) \ \in R_2 \\ \overline{co}\{f_2,\, f_3\}\,, & (u,v) \in R_2 \cap R_3 \\ f_3(u,v)\,, & (u,v) \in R_3 \\ \overline{co}\{f_3,\, f_4\}\,, & (u,v) \in R_3 \cap R_4 \\ f_4(u,v)\,, & (u,v) \in R_4 \\ \overline{co}\{f_4,\, f_1\}\,, & (u,v) \in R_4 \cap R_1 \end{cases} \tag{4.5}$$

Here, the $\overline{co}\{f,\, g\} := \alpha\, f + (1-\alpha)\, g$ with $\alpha \in [0,1]$ is the closed convex hull of all values between f and g.

4.3.2 Equilibria and Pseudo Equilibria

In this section, we characterize steady states of the Filippov system found in Eq. (4.5). There is only one fixed point of the system $(\bar{u}_1, \bar{v}_1)$, which is the stable resting state. However, since the system in Eq. (4.3) has a discontinuous right hand side, we should consider the Heaviside function as set valued at zero. Then we obtain a differential inclusion, as in Eq. (4.5), which brings into consideration two other points in the plane, *pseudo equilibria*. Figure 22 shows the switching boundaries, defined by Σ and Γ, drawn with dashed lines. Their intersection, though not a fixed point in standard ODE theory, behaves as such. For instance, when $\tau > 0$ is small, trajectories with nearby initial conditions tend to this intersection point, but for τ past a certain value, even solutions starting in a neighborhood, go away from the intersection. The stability of this pseudo fixed point will be analyzed by expanding in a neighborhood of the intersection point and studying the Poincaré map of the local dynamics.

As shown in Fig. 22, the point $(\bar{u}_2, \bar{v}_2)$ occurs at the intersection of the v-nullcline and the switching manifold $\{g \equiv 0\}$. We characterize this point as a *pseudo saddle* with unstable manifolds that coincide with the invariant set $\{v \equiv 0\} \cap \{0 < u < d\}$. From the

rest state, if we give a small depolarizing current to the network, the system returns to the stable resting state. A sufficiently large depolarizing current pulls up the u–nullcline through a pseudo saddle–node bifurcation, which allows mean firing rate of E cells to escape rest, and through recurrent excitation to both E and I cell types, the excitatory cells drive the inhibitory population from a lower activity state. The threshold for excitability as a response to sensory input to the network is largely determined by the stable manifold emanating from the pseudo saddle. For initial conditions past this separatrix, the fate of the trajectory is then determined by the stability of the inhibitory–stabilized state, corresponding to the pseudo focus $(\bar{u}_3, \bar{v}_3)$. In the coming sections, we will investigate this separatrix along with stability of the pseudo focus to obtain a more global picture of the nonsmooth phase plane.

In Sections 4.4.1 and 4.4.2, we show that the point $(\bar{u}_3, \bar{v}_3) = (\frac{a\,d-b\,c}{a-c}, \frac{d-b}{a-c})$ undergoes a pseudo Hopf bifurcation for some $\tau = \tau_{HB}$. That is, for small $\tau_{HB} > \tau > 0$, the point $(\bar{u}_3, \bar{v}_3)$ is a *stable* pseudo focus, while for $\tau > \tau_{HB}$, it is an *unstable* pseudo focus. Generalizations of the Hopf bifurcation have been presented in a series of collaborative papers by Küpper and in a separate work by Han and Zhang [44, 81, 31]. These works generalize the Hopf bifurcation for a pseudo focus occurring at a *single* switching manifold, while the pseudo Hopf, presented in the next sections, occurs for a point at the intersection of the *two* switching manifolds. Though we refer to this point as a pseudo focus or focal crossing, we will see in Section 4.5.1 that for small $\tau > 0$ trajectories may have sliding modes approaching it in finite time[1]. As Fig. 23 depicts trajectories that piecewise smoothly spiral toward or away from the intersection (depending on τ), we use the term "focus". Then, in order to have a well-defined Poincaré Map, we should be prudent in checking that there are only transversal crossings of the switching manifolds in a neighborhood of this point. We show that this is indeed the case in Sections 4.5.1 and 4.5.2.

[1]It may be appropriate, then, to refer to this point as a pseudo node for this range of τ.

4.4 BIFURCATION ANALYSIS OF THE UP STATE

4.4.1 A local approximation around the intersection of the two switching boundaries

We have a general notion of stability for the pseudo focus at $(\bar{u}_3, \bar{v}_3)$. That is, the point is stable if solutions tend to it as $t \to \infty$, and unstable if solutions tend to it as $t \to -\infty$. If we were to try the standard linear stability analysis, beginning with the system found in Eq. (4.3), we would formally differentiate the Heaviside and obtain a Dirac-delta function multiplied by some scalar. Since we are at the intersection of two switching manifolds, it is unclear how to evaluate the delta functions. Instead, we consider the local expansion in an ε–neighborhood of the intersection, by putting $u = \bar{u}_3 + \varepsilon\widetilde{u}$, $v = \bar{v}_3 + \varepsilon\widetilde{v}$, and $t = \varepsilon\widetilde{t}$.

Hence differentiating with respect to $\frac{d}{dt} = '$, we have $u' = \varepsilon\widetilde{u}' = \frac{d\widetilde{u}}{d\widetilde{t}}$ and $v' = \varepsilon\widetilde{v}' = \frac{d\widetilde{v}}{d\widetilde{t}}$. For now, we let $(\bar{u}, \bar{v}) = (\bar{u}_3, \bar{v}_3)$ denote the intersection of the two switching boundaries, recalling that it solves the linear system given by $g(\bar{u}, \bar{v}) = h(\bar{u}, \bar{v}) = 0$. Plugging into (4.3) , we obtain $\frac{d\widetilde{u}}{d\widetilde{t}} = -\bar{u} + H(\widetilde{u} - a\widetilde{v}) + O(\varepsilon)$ and $\frac{d\widetilde{v}}{d\widetilde{t}} = \left(-\bar{v} + H(\widetilde{u} - c\widetilde{v})\right)/\tau + O(\varepsilon)$. Note that we may absorb the ε's found inside the Heaviside step function, as its value is only determined by the sign of the argument. Putting $u \mapsto \widetilde{u}$, $v \mapsto \widetilde{v}$, and $t \mapsto \widetilde{t}$, we write the nonsmooth approximate system up to order ε,

$$\begin{aligned} \frac{du}{dt} &= -\bar{u} + H(u - av) \\ \frac{dv}{dt} &= \left(-\bar{v} + H(u - cv)\right)/\tau \ . \end{aligned}$$

We define the switching manifolds in terms of the zero level sets of $l_1(u, v) = u - a\,v$ and $l_2(u, v) = u - c\,v$. Hence, the boundaries are lines passing through the origin with slopes $\frac{1}{a}$ and $\frac{1}{c}$, that is,

$$\Sigma' = \left\{(u, v) \in \mathbb{R}^2 |\ v = \frac{u}{a}\right\} = \{l_1(u, v) = 0\}$$

$$\Gamma' = \left\{(u, v) \in \mathbb{R}^2 |\ v = \frac{u}{c}\right\} = \{l_2(u, v) = 0\} \ .$$

The switching boundaries are depicted in Fig. 23, along with solution trajectories for two values of the inhibitory time constant τ. The vector fields are appropriately labeled by the

functions p_1 through p_4.

$$p_1(u,v) = \begin{pmatrix} -\bar{u}+1 \\ -\bar{v}/\tau \end{pmatrix}, \qquad p_2(u,v) = \begin{pmatrix} -\bar{u}+1 \\ (-\bar{v}+1)/\tau \end{pmatrix}$$

$$p_3(u,v) = \begin{pmatrix} -\bar{u} \\ (-\bar{v}+1)/\tau \end{pmatrix}, \quad p_4(u,v) = \begin{pmatrix} -\bar{u} \\ -\bar{v}/\tau \end{pmatrix}$$

4.4.2 The Poincaré Map

Note that the vector fields $p_1, \ldots, p_4$ are constants, and as the constants differ, trajectories that transversally cross the switching boundaries Σ' and Γ' have constant jumps in their derivatives (independent of where the solution crosses the boundary). Though the vector field is discontinuous, solutions are piecewise smooth and continuous everywhere. Moreover, in Sections 4.5.1 and 4.5.2, we show that sliding modes do not exist along the u and v–switching boundaries, neither above nor below the intersection point for all $\tau > \tau_{crit3}$ (defined in Eq. (4.10)). Hence, for $\tau > \tau_{crit3}$, we may define a continuous Poincaré Map of Eq. (4.6) analogous to the one from standard ODE theory. We let the Poincaré section be the set $S := \Sigma' \cap \{(u,v) \mid -1 < u < 0\}$ and parametrize it by the u–variable. Then we define the Poincaré Map

$$\mathbf{P} : (-1,0) \to (-1,0) \text{ given by } \mathbf{P}(u_0) = P(u_0;\tau) = u_4^* ,$$

where $(u_0, u_0/a)$, $(u_4^*, u_4^*/a) \in S$.

For smaller values of $\tau_1 > \tau_{crit3}$, we have $\mathbf{P}(u_0;\tau_1) - u_0 > 0$, indicating that the pseudo equilibrium at $(\bar{u},\bar{v})$ is stable. On the other hand, $\tau_2 > \tau_{crit3}$ large enough gives that $\mathbf{P}(u_0;\tau_2) - u_0 < 0$, corresponding to an unstable focus. The right panel of Figure 23 illustrates this using values of τ above and below the bifurcation value of $\tau = \tau_{HB} \approx 0.5239$.

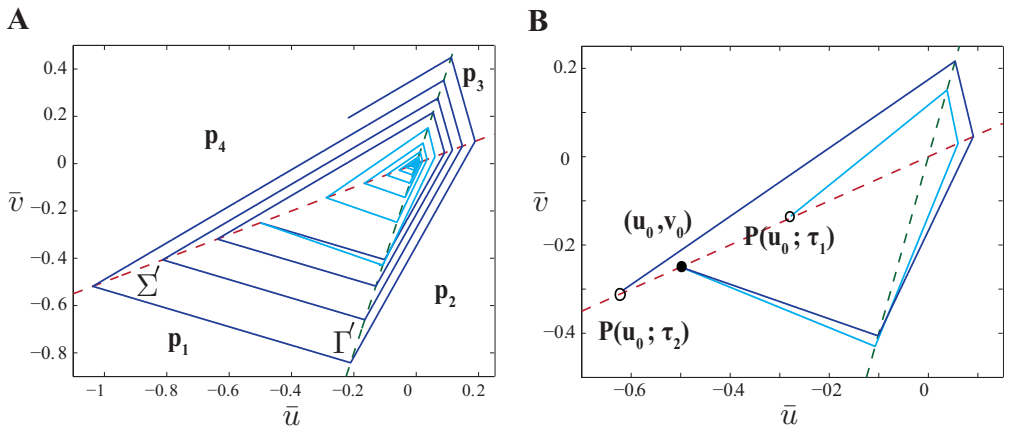

Figure 23: The phase plane of the asymptotic expansion found in Equation (4.6). (A) Two superimposed counter-clockwise, piecewise smooth trajectories that transversally cross the switching boundaries defined by Σ' (red dashed) and Γ' (green dashed). The light blue solid line depicts a trajectory tending to the stable pseudo focus at zero that corresponds to $\tau_1 = 0.47$. The dark blue curve is a solution trajectory spiraling away from the origin, with the same initial condition $(-.5, -.25)$ but for $\tau_2 = 0.55$. (B) The values of the Poincaré map (empty circles) from the initial condition (filled–in black circle) for parameter values τ_1 and τ_2. All other parameters are as in Fig. 22.

By continuous dependence on parameters, the Poincaré Map is continuous with respect to τ and thus has the intermediate value property. Hence, there must be a value of τ for which the Poincaré Map is the identity on $(-1, 0)$. We may write a piecewise smooth solution that is continuous everywhere by satisfying continuity conditions at transversal crossings of the switching manifolds. We let (u_i, v_i) for $i = 1, \ldots, 4$ be the solution of the equation

$$\begin{pmatrix} u_i \\ v_i \end{pmatrix}' = p_i(u_i, v_i)\,.$$

We successively piece together the limit cycle by taking the final value u_i^* of the solution with right hand side $p_i(u, v)$ to be the initial value for the proceeding system $p_{i+1}(u, v)$. Let $(u_0, v_0) = (u_0, u_0/a) \in \Sigma'$ with $u_0 \in (-1, 0)$. After much algebraic manipulation and good use of vector field symmetries, we are able to write an analytic formula for $\tau_{HB} = \tau(\bar{u}, \bar{v}, a, c)$. We conjecture that at this value of τ there are infinitely many periodic solutions in the expanded system (4.6) and a pseudo Hopf bifurcation in the nonsmooth system of interest, found in Eq. (4.3).

First, we define the expressions m_1 through m_4 which are the slopes of the solutions multiplied by τ:

$$m_1 = \tfrac{-\bar{v}}{(-\bar{u}+1)}\ , \quad m_2 = \tfrac{-\bar{v}+1}{(-\bar{u}+1)}\ ,$$
$$m_3 = \tfrac{-\bar{v}+1}{(-\bar{u})}\ , \quad m_4 = \tfrac{\bar{v}}{\bar{u}}\ .$$

The first piece of the solution is the line $v_1 = v_0 + \frac{m_1}{\tau}(u_1 - u_0)$. This line intersects the boundary Γ' at the point $\frac{u_1^*}{c} = v_1 = v_0 + \frac{m_1}{\tau}(u_1^* - u_0)$. Solving for u_1^*, we obtain $u_1^* = u_0 \frac{(\tau/a - m_1)}{(\tau/c - m_1)}$ and $v_1^* = u_1^*/c$. Solving the next linear system, we have $v_2 = v_1^* + \frac{m_2}{\tau}(u_2 - u_1^*)$. The line intersects the boundary Σ' at the point $\frac{u_2^*}{a} = v_2^* = v_1^* + \frac{m_2}{\tau}(u_2^* - u_1^*)$. Hence, $u_2^* = u_1^* \frac{(\tau/c - m_2)}{(\tau/a - m_2)}$ and $v_2^* = u_2^*/a$. Recognizing the pattern, we have $v_3 = v_2^* + \frac{m_3}{\tau}(u_3 - u_2^*)$ which intersects Γ' at $u_3^* = u_2^* \frac{(\tau/a - m_3)}{(\tau/c - m_3)}$. Lastly, we have $u_4^* = u_3^* \frac{(\tau/c - m_4)}{(\tau/a - m_4)}$. Plugging the previous equation into each proceeding equation we obtain a formula for the Poincaré Map

$$\mathbf{P}(u_0; \tau) = u_4^* = u_0\, K(\tau)\ ,$$

where

$$K(\tau) := \frac{(\tau - a\,m_1)\,(\tau - c\,m_2)\,(\tau - a\,m_3)\,(\tau - c\,m_4)}{(\tau - c\,m_1)\,(\tau - a\,m_2)\,(\tau - c\,m_3)\,(\tau - a\,m_4)}$$

is the ratio of two polynomials in τ. If $K(\tau) > 1$, then the pseudo fixed point $(\bar{u}_3, \bar{v}_3)$ is repelling and if $K(\tau) < 1$, it is attracting.

The transition from attracting to repelling is the pseudo Hopf bifurcation point, thus we want to find the value of τ, such that $K(\tau) = 1$. To do this, we multiply both sides of the equation, $K(\tau) = 1$ by the polynomial in the denominator of $K(\tau)$. After expanding the two quartics, we note that the constant terms and the leading terms cancel on either side. Dividing both sides by τ, we obtain two quadratics in τ. To help with simplifications, we note that $m_1\,m_3 = m_2\,m_4$. We have

$$\begin{aligned} q_1(\tau) = \tau^2\ &(a\,(m_1 + m_3) + c\,(m_2 + m_4)) - \tau\,(m_1\,m_2 + m_3\,m_4 + m_1\,m_4 + m_2\,m_3)\,a\,c \\ &-\tau\ \left(a^2 + c^2\right)\ m_1\,m_3 + a\,c\,(a\,(m_2 + m_4) + c\,(m_1 + m_3))\ m_1\,m_3 \end{aligned}$$

and

$$\begin{aligned} q_2(\tau) = \tau^2\ &(a\,(m_2 + m_4) + c\,(m_1 + m_3)) - \tau\,(m_1\,m_2 + m_3\,m_4 + m_1\,m_4 + m_2\,m_3)\,a\,c \\ &-\tau\ \left(a^2 + c^2\right)\ m_1\,m_3 + a\,c\,(a\,(m_1 + m_3) + c\,(m_2 + m_4))\ m_1\,m_3\ . \end{aligned}$$

We see that the first order terms cancel. Denoting $q(\tau) = q_1(\tau) - q_2(\tau)$, we set

$$0 = q(\tau) = \tau^2\,(a - c)\ (m_1 - m_2 + m_3 - m_4)) - a\,c\ (a - c)\ (m_1 - m_2 + m_3 - m_4)\ .$$

Hence we have a formula for τ when $K(\tau) = 1$ and thus, where the pseudo Hopf bifurcation occurs,

$$\tau_{HB} := \sqrt{(a\,c)\ m_1\,m_3} = \sqrt{(a\,c)\,\frac{\bar{v}_3\,(1 - \bar{v}_3)}{\bar{u}_3\,(1 - \bar{u}_3)}}\ . \tag{4.6}$$

In Figure 24, we plot Eq. (4.6) as a function of the parameters a, b, c and d. In each panel, the dots correspond to the usual parameter values and the curves are functions of one parameter while keeping the rest fixed to these values. Moreover, as seen in the first panel in varying a, since $\tau > 0$, there cannot exist a Hopf bifurcation if the inhibition to the

excitatory population is too weak. The bottom two panels of Fig. 24 show $\tau = \tau_{HB}$ as the disinhibition c and the inhibitory threshold d are varied respectively. Note the asymptotes are given by $c = \frac{a\,(1-d)}{1-b} = \frac{28}{19} \approx 1.4737$ and $d = 1 - \frac{c\,(1-b)}{a} = \frac{141}{160} = .88125$ and occur as $\bar{u}_3$ approaches 1.

Numerical simulations indicate that the limit cycles encircling the focal crossing at $(\bar{u}_3, \bar{v}_3)$ are stable. However, it is quite difficult to show this, as the Poincaré Map for (4.3) must be pieced together as we did for the expanded system in (4.6). If the Poincaré section is taken to be the lower piece of the u–switching manifold (and parametrized by u_0 as before), then the map contains four unknown constants $t_1, \ldots, t_4$, which are the durations that the solution spends in regions $R_1, \ldots, R_4$. If we denote the fixed point of the Poincaré Map for (4.3) by u_0^* , then we would need to solve for $t_1, \ldots, t_4$ to determine their dependence on the initial point, u_0 in a δ–neighborhood of u_0^*, in order to show whether the derivative of the Poincaré Map is above or below 1.

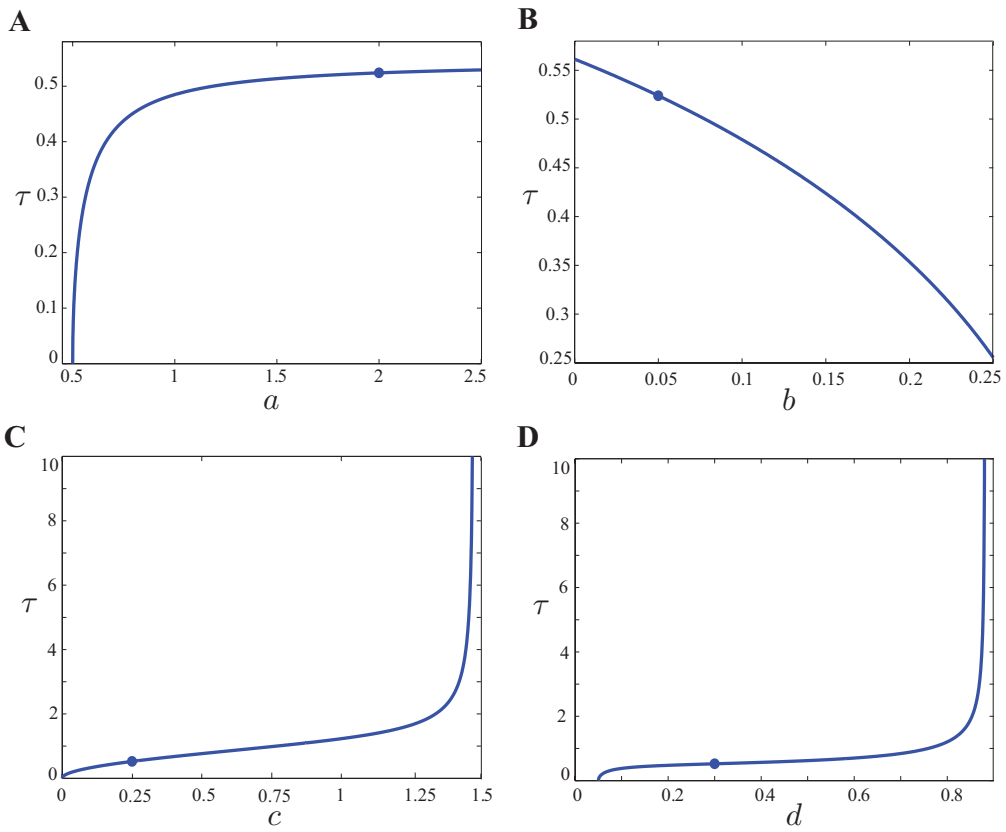

Figure 24: The parameter value of $\tau = \tau_{HB}$ for which the system undergoes a pseudo Hopf bifurcation, plotted using Eq. (4.6) as a function of the parameters.

4.5 ADDITIONAL BIFURCATIONS

4.5.1 Sliding in the Pseudo Heteroclinic

In the next section we study the pseudo heteroclinic orbit connecting the two pseudo fixed points $(\bar{u}_2, \bar{v}_2)$ to $(\bar{u}_3, \bar{v}_3)$. Once again, the time scale of the inhibitory population is an important parameter in determining how trajectories approach the focal or nodal crossing, whether it be through a spiraling approach by transversal crossings of the boundaries or through a sliding mode along the v–switching manifold. We perturb from the point $(\bar{u}_2, \bar{v}_2)$ in the u–direction. If we perturb to the left, the trajectory goes to lower resting state at $(0, 0)$; if we perturb to the right, the trajectory travels along the invariant manifold till it reaches the corner. To determine whether the solution slides along Γ below the pseudo fixed point, we employ the Filippov Method for sliding modes. Write the sliding dynamics as

$$\begin{pmatrix} u \\ v \end{pmatrix}' \in f^{sl}_{1,2}(u, v) := \alpha\, f_1(u, v) + (1 - \alpha)\, f_2(u, v) \quad , \quad \alpha \in [0, 1]\,. \tag{4.7}$$

As ∇h is normal to the switching manifold, the necessary condition for linear sliding is

$$(\nabla h \cdot f_1)\,(\nabla h \cdot f_2) < 0\ ,$$

that is, the inner product of the normal with the two vector fields must have opposite sign. Following the method, we put $0 = \nabla h \cdot f^{sl}_{1,2} = \begin{pmatrix} 1 \\ -c \end{pmatrix} \cdot \begin{pmatrix} -u + 1 \\ (-v + 1 - \alpha)/\tau \end{pmatrix} = -u + 1 - c\,(-v + 1)/\tau + c\,\alpha/\tau = u\,(1/\tau - 1) + c\,\alpha/\tau + 1 - d/\tau - c/\tau$, since we are looking for sliding along the line $v = (u - d)/c$. Hence,

$$\alpha = 1 - \tau\,/c + d/c - u\,(1 - \tau)/c\ . \tag{4.8}$$

Then $\alpha \leq 1$ holds for all $\tau > 0 > \frac{d-u}{1-u}$ $(\forall\, u > d)$ which gives us no restriction on τ for sliding along the lower piece of the v–switching boundary. But we also require $\alpha \geq 0$, which holds for all $(u, v) \in \Gamma \cap \{d \leq u \leq \bar{u}_3\}$ whenever τ is less than

$$\tau_{crit2} := \frac{c + d - \bar{u}_3}{1 - \bar{u}_3}\ . \tag{4.9}$$

Assume that $\tau < \tau_{crit2}$ and $v = \frac{u-d}{c}$. Plug in α from Eq. (4.8) to the Filippov derivative found in Eq. (4.7) to obtain

$$\begin{pmatrix} u \\ v \end{pmatrix}' \in f_{1,2}^{sl}(u,v) = \begin{pmatrix} -u+1 \\ \frac{-\left(\frac{u-d}{c}\right)+1-(1-\tau/c+d/c-u(1-\tau)/c)}{\tau} \end{pmatrix} = \begin{pmatrix} -u+1 \\ \frac{1}{c}(-u+1) \end{pmatrix} .$$

Then the sliding dynamics are such that $\frac{dv}{du} = \frac{dv/dt}{du/dt} = \frac{1}{c}$, which is the slope of a line in the plane. We then note that $\frac{d}{du}(v) = \frac{d}{du}(\frac{u-d}{c}) = \frac{1}{c}$ which shows self-consistency that $h(u,v) = 0$ as was assumed.

Since the derivative of Eq. (4.9) with respect to u is negative for all $u \in [0,1]$, then τ_{crit2} is the infimum over all values of τ for which sliding exists in the set $\Gamma \cap \{d \le u \le \bar{u}_3\}$. Moreover, evaluating (4.9) at $u = d$, the smallest value of τ for which (partial) sliding may exist on $\Gamma \cap \{d \le u \le \bar{u}_3\}$ is given by

$$\tau_{crit3} := \frac{c}{1-d} . \tag{4.10}$$

Now, for τ slightly greater than τ_{crit2}, the sliding mode falls off at the critical value of u, say $u = u_{crit1} := \frac{c+d-\tau}{1-\tau}$, which corresponds to $f_{1,2}^{sl} = f_2$. At this point, the trajectory goes into R_2, and the trajectory spirals into the focal crossing, going through an infinite number of transversal crossings with the nearby switching manifolds. To prove this, we first show there are only transversal crossings along $\Sigma \cap \{\bar{u}_3 \le u \le 1\}$. We require $\alpha \in [0,1]$ so that

$$0 = \overline{co}\{f_2,\ f_3\} \cdot \nabla g = \alpha - u + \frac{1}{\tau}(u - a - b) .$$

Then $\alpha = u + \frac{1}{\tau}(a+b-u)$, if sliding is to exist. Note that $\alpha \ge \frac{1}{\tau}(a+b-u) > 1$, so *no sliding exists* above the focal crossing between the vector fields f_2 and f_3 for all $0 < \tau \le 1$.

We see that the absolute value of the slopes of the vector fields in Figure 22 decrease with increasing τ. As a consequence, for τ small enough, we expect stable sliding along $\Gamma \cap \{\bar{v}_3 \le v \le 1\}$ and for $0 < \tau < 1$ large enough, expect unstable sliding along $\Sigma \cap \{b \le u \le \bar{u}_3\}$. The latter, we leave for the next section in which we study the pseudo homoclinic bifurcation. To investigate the former, we apply the Filippov Method. We have

$$\begin{pmatrix} u \\ v \end{pmatrix}' \in f_{3,4}^{sl}(u,v) = \alpha\, f_3 + (1-\alpha)\, f_4 = \begin{pmatrix} -u \\ \frac{-v+\alpha}{\tau} \end{pmatrix} \quad , \quad \alpha \in [0,1] .$$

Setting $\nabla h \cdot f_{3,4}^{sl} = 0$, for sliding to exist, we must have

$$\alpha = v - \frac{\tau}{c} u = v - \frac{\tau}{c} (c\, v + d) = v\,(1 - \tau) - \tau\, d/c \ .$$

Note that $\alpha = v\,(1-\tau) - \tau\, d/c \leq 1$ for all $\tau > 0$, and $\alpha = v\,(1-\tau) - \tau\, d/c \geq 0$ if and only if

$$\tau \leq \frac{v}{v + d/c} \, .$$

As $\frac{v}{v+d/c}$ is an increasing function of v, we have stable sliding for all $(u, v) \in \Gamma \cap \{\bar{v}_3 \leq v \leq 1\}$ whenever

$$\tau \leq \tau_{crit1} := \frac{\bar{v}_3}{\bar{v}_3 + d/c} \ .$$

For the usual parameters, the critical values of τ occur in the order

$$\tau_{crit1} < \tau_{crit2} < \tau_{crit3} \ .$$

Figure 25 shows a sliding mode along the switching boundary Γ as well as a sliding mode that falls into R_2 and then spirals into the pseudo focus. The last curve corresponds to letting $\tau_{crit3} < \tau < \tau_{HB}$, for which no sliding exists along this piece of the v-switching boundary.

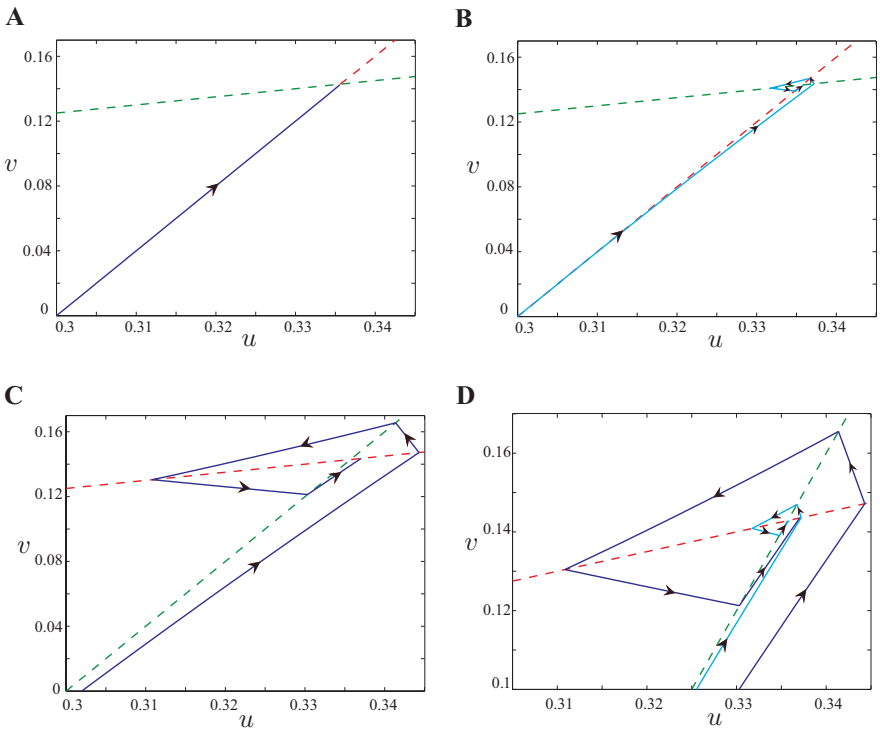

Figure 25: Three trajectories coming off the unstable manifold of the pseudo saddle, tending to the stable pseudo focus at $(\bar{u}_3, \bar{v}_3)$ for values of $\tau < \tau_{HB} \approx 0.52396$. (A) The dark blue trajectory is the sliding mode along the v-switching boundary ($0.3 = \tau < \tau_{crit2} \approx .3226$). (B) The light blue illustrates partial sliding when $0.352 = \tau > \tau_{crit2}$, falling off at $u_{crit1} = 11/36 = 0.30\bar{5}$. (C) The dark blue has no sliding modes, letting $\tau = .38 > \tau_{crit3} \approx .3571$. (D) Magnification of panel B and C.

4.5.2 The Pseudo Homoclinic Bifurcation

As we increase the bifurcation parameter τ through τ_{HB}, the focal crossing becomes unstable, giving rise to limit cycles. The limit cycles are shown in Fig. 26, with the larger orbit corresponding to larger τ. The other two curves in Fig. 26 depict the stable manifold of the pseudo saddle at $(\bar{u}_2, \bar{v}_2)$, with colors corresponding to the same values of τ as in the limit cycles. This stable manifold gives a clear geometrical threshold for the population of neurons to go to a higher activity state and return to rest. As the time scale of inhibition increases, the threshold moves closer to the corner. Though not shown, for large enough τ, the sliding mode evolving backward in time hits the v–switching manifold from region R_2. A simple shooting argument using continuous dependence on parameters shows that there is a $\tau = \tau_{HC}$ such that a stable sliding trajectory evolving backward in time along the stable manifold hits the knee of the v–nullcline. This relies on the fact that the forward–stable trajectories transversally cross the boundaries for all $\tau \geq \tau_{crit3}$.

We now use the Filippov method to study sliding along the u–switching boundary, above the pseudo saddle at $(\bar{u}_2, \bar{v}_2)$. Hence, write

$$\begin{pmatrix} u \\ v \end{pmatrix}' \in f_{1,4}^{sl}(u,v) = \alpha\, f_1 + (1-\alpha)\, f_4 = \begin{pmatrix} \alpha - u \\ \frac{-v}{\tau} \end{pmatrix} \quad , \quad \alpha \in [0,1]\,. \tag{4.11}$$

Following the method, we put $0 = \nabla g \cdot f_{1,4}^{sl} = \alpha - u + \frac{a\,v}{\tau}$. Then

$$\alpha = u - \frac{a\,v}{\tau} = u - \left(\frac{u-b}{\tau}\right)\,. \tag{4.12}$$

Plugging α from Eq. (4.12) into Eq. (4.11), we have the sliding dynamics

$$\begin{pmatrix} u \\ v \end{pmatrix}' \in f_{1,4}^{sl}(u,v) = \begin{pmatrix} -\frac{a\,v}{\tau} \\ \frac{-v}{\tau} \end{pmatrix}\,.$$

Then $\frac{dv}{du} = \frac{1}{a}$, which is precisely the slope of the line $v = \frac{(u-b)}{a}$.

The stable limit cycles shown in Fig. 26 grow with τ and persist up until they meet with an unstable limit cycle at a saddle-node of limit cycles (see Fig. 27 below). This latter bifurcation occurs for τ beyond the homoclinic bifurcation. The homoclinic orbit (shown in Fig. 27) has a sliding mode which is unstable in the forward time direction. Thus the

homoclinic orbit is stable backward in time and has attractive sliding up to the critical value of $u = u_{crit2} := \frac{b}{1-\tau}$ for $0 < \tau \leq 1$. This is precisely when $\alpha = 0$, and hence the Filippov derivative along the u–switching manifold coincides with f_4 at the critical value $u = u_{crit2}$. Starting from the initial value $(u_{crit2}, \frac{(u_{crit2}-b)}{a})$ and flowing backward in time, the trajectory is uniquely determined and approaches the pseudo saddle (in finite time) via the unstable manifold along the u–axis. However, since sliding during the homoclinic is stable in the backward time direction, the forward time evolution shows a *visible grazing* solution or *tangency* at the critical sliding value of $(u_{crit2}, \frac{(u_{crit2}-b)}{a})$.

Figure 27 shows the homoclinic orbit along with the grazing solution which illustrates the time-directional non–uniqueness. Beginning from $(u_{crit2}, \frac{(u_{crit2}-b)}{a})$, one solution asymptotically approaches the stable node at the origin and the other embraces the sliding mode. Once the sliding mode begins, it is invariant as $\nabla g \cdot f_4 > 0$ and $\nabla g \cdot f_1 < 0$ and thus, the solution asymptotically slides into the pseudo saddle.

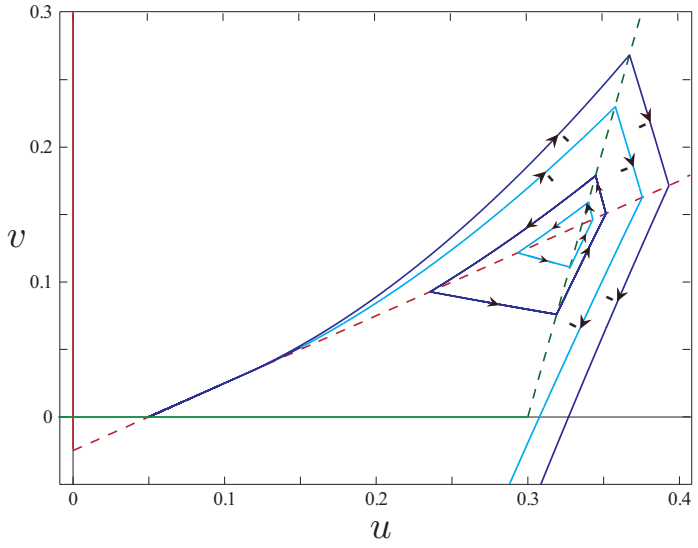

Figure 26: The limit cycles and stable manifold of the pseudo saddle for two values of τ, both satisfying $\tau_{HB} < \tau_1 = 0.55 < \tau_2 = 0.58 < \tau_{HC}$. As sliding on the u-switching boundary is unstable forward in time, the sliding is stable up to a critical value $u = u_{crit2}$ when evolving backward in time. The arrows with negative signs denote the backward in time evolution.

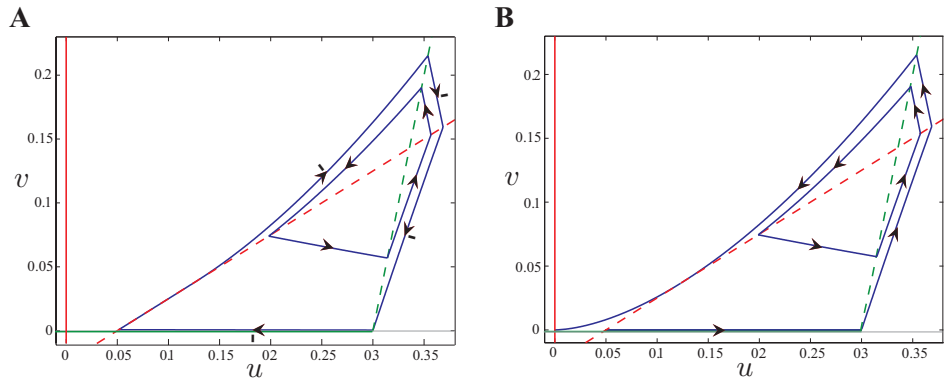

Figure 27: At the homoclinic bifurcation $\tau \approx 0.595$: (A) a stable limit cycle (forward in time) and homoclinic (converging backward in time). (B) the same stable limit cycle and trajectory connecting the unstable manifold of the pseudo saddle to the stable node at the origin (forward in time). The homoclinic and grazing solution are identical until the sliding point at $u = u_{crit}$. From this point, the solution curves evolve backward in time uniquely. However, forward in time, there are two viable paths consistent with the vector field. The trajectory may tend to the node at the origin (forward stable) or slide into the pseudo saddle at $(b, 0)$ (backward stable).

4.5.3 After the Pseudo Homoclinic

Unstable limit cycles emerge from the homoclinic bifurcation and shrink with increasing τ. Then for some value of $\tau > \tau_{HC}$, say $\tau := \tau_{LP}$, the stable and unstable periodic orbits collide to annihilate one another. This happens at the fold in the bifurcation diagram, shown in Fig. 28.

Figure 28 was pieced together, solving three similar boundary value problems and continuing the orbit to produce a co–dimension one bifurcation diagram. For the stable limit cycle, we write an 12 dimensional boundary value problem having dynamics for (u, v) according to the region $R_1 \dots R_4$ (see Appendix C). With initial condition on the u–switching manifold, we solve each piece simultaneously and apply boundary conditions that ensure continuity of

the periodic orbit. We separate the unstable limit cycle into two pieces with respect to the bifurcation parameter τ: (1) The orbit with a sliding mode along the u–switching manifold (Fig. 28, dark blue), and (2) the orbit with transversal crossings only (Fig. 28, light blue). As these limit cycles are unstable, we numerically integrate backward in time to converge to the orbit. The periodic orbit without a sliding mode is solved with essentially the same BVP as the stable periodic orbit, while the periodic orbit with a sliding mode has an extra piece to solve. Hence we set up a 15 dimensional BVP for the unstable periodic orbit with sliding (see Appendix, section C).

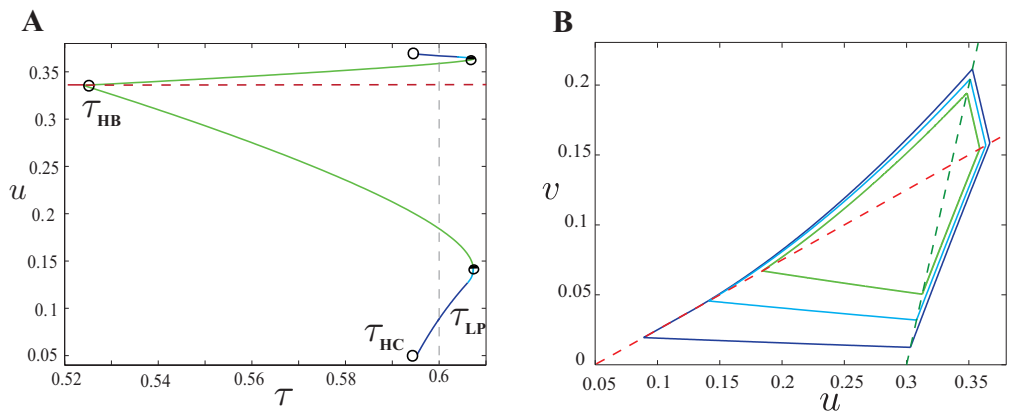

Figure 28: Bifurcation diagram following the maximal and minimal values of u for the stable and unstable periodic orbits as we vary τ: (A) The stable periodic orbits (green) appear from a Hopf bifurcation for $\tau_{HB} \approx 0.5239$ from a stable pseudo focus (red). The curve of growing stable limit cycles terminates at a saddle-node of limit cycles $\tau_{LP} \approx 0.6073$ when it collides with the larger, shrinking unstable periodic orbit. These unstable limit cycles near the fold have no sliding (light blue). Then for $\tau \approx 0.6061$, a sliding mode exists on the u-switching boundary. The sliding periodic orbits (dark blue) terminate at the homoclinic bifurcation $\tau_{HC} \approx 0.595$. (B) The green and dark blue limit cycles are stable and unstable respectively and correspond to $\tau = 0.6$ as depicted by the vertical grey line in the bifurcation diagram. The light blue orbit corresponds to the saddle-node of limit cycles (SNLC) at which the unstable and stable limit cycles collide.

4.5.4 The Pseudo SNIC

In the next section, we study the saddle-node on an invariant circle (SNIC) bifurcation. This bifurcation is not a traditional SNIC as in a smooth system, since the saddle-node that collides with the stable node is actually a pseudo equilibrium. Still, as the pseudo saddle behaves like a fixed point, the bifurcation is quite analogous. We take τ large enough so that the pseudo focus is unstable and let the bifurcation parameter be the activity threshold b to the excitatory population.

A decrease in the bifurcation parameter b raises the u–switching boundary. Starting with small positive threshold $b = 0.05$ (Fig. 29, top), we have a pseudo heteroclinic coming off the right unstable manifold of the pseudo saddle (in finite time) that tends to the stable fixed point at the origin. Figure 29 also shows a smaller heteroclinic which satisfies $v = 0$ for all time and $u \to 0$ as $t \to \infty$ and $u \to b$ as $t \to -\infty$. As both heteroclinics take infinite time to reach at least one endpoint, these solutions cannot be solved by setting up an appropriate BVP as before (See Appendix, section C).

Figure 29B shows the pseudo SNIC bifurcation ($b = 0$). At this point, the pseudo saddle and stable node collide. Similar to Fig. 29A, the solution spends infinite time in region R_4

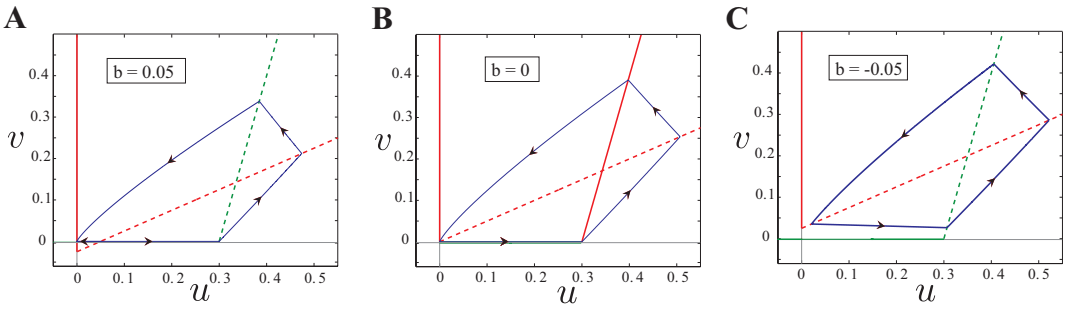

Figure 29: (A) For $b > 0$, there is a fixed point at the origin and a pseudo saddle. Two heteroclinic orbits connect the pseudo saddle to the origin: A larger orbit that goes around the intersection point and a smaller one along $v = 0$. (B) When $b = 0$, the system is at the SNIC bifurcation. (C) For $b < 0$, we see a periodic orbit.

as it asymptotically approaches zero, so we cannot set up a BVP to directly obtain the orbit. Instead we set up an 8 dimensional BVP for the stable limit cycle found in the bottom panel and then follow this solution as $b \to 0^-$. As b gets closer to the bifurcation value, the period of time spent in R_4 increases: The larger the period becomes; the closer the approximation for the SNIC bifurcation.

4.6 THE SMOOTH AND PIECE–WISE LINEAR SYSTEMS

We now consider the Wilson–Cowan equations with four different firing rate functions:

$$f_1(x) = (\text{atan}(\beta x) + \pi/2)/\pi\,, \quad \text{atan}$$

$$f_2(x) = 1/(1 + \exp(-\beta x))\,, \quad \text{logistic}$$

$$f_3(x) = (1 + \text{erf}(\beta x))/2\,, \quad \text{erf}$$

$$f_4(x) = \begin{cases} 0 & x < 0 \\ \beta\, x & 0 \le x \le \frac{1}{\beta} \\ 1 & x > \frac{1}{\beta} \end{cases} \quad , \quad \text{pwl}\,.$$

Note that f_1, f_2, and f_3 are smooth, (strictly) increasing, and asymptote to 0 and 1, while f_4 is a continuous, nondecreasing function that is smooth except at the points $x = 0$ and $x = \frac{1}{\beta}$ and is bounded by 0 and 1. In this section, we will compare the behavior of the solution trajectories for the smooth and piece–wise linear systems, specifically, the periodic orbits that arise from a Hopf bifurcation, in the stiff limit when $\beta >> 1$.

The systems having the firing rates $f_1, \ldots, f_4$ point–wise limit to the discontinuous system found in Eqn. (4.3) when passing the limit, $\beta \to \infty$. So it is natural to ask whether the bifurcations of the smooth and pwl stiff systems limit to those in the discontinuous system. The top of Figure 30 shows the bifurcation diagram for the smooth WC model with logistic firing rate function, letting $\beta = 1000$. Broadly speaking, it is qualitatively similar to the nonsmooth diagram. That is, we see the Hopf bifurcation and the fold of limit cycles with the unstable branch shrinking from a homoclinic bifurcation. For a fixed value of $\tau = 0.55$,

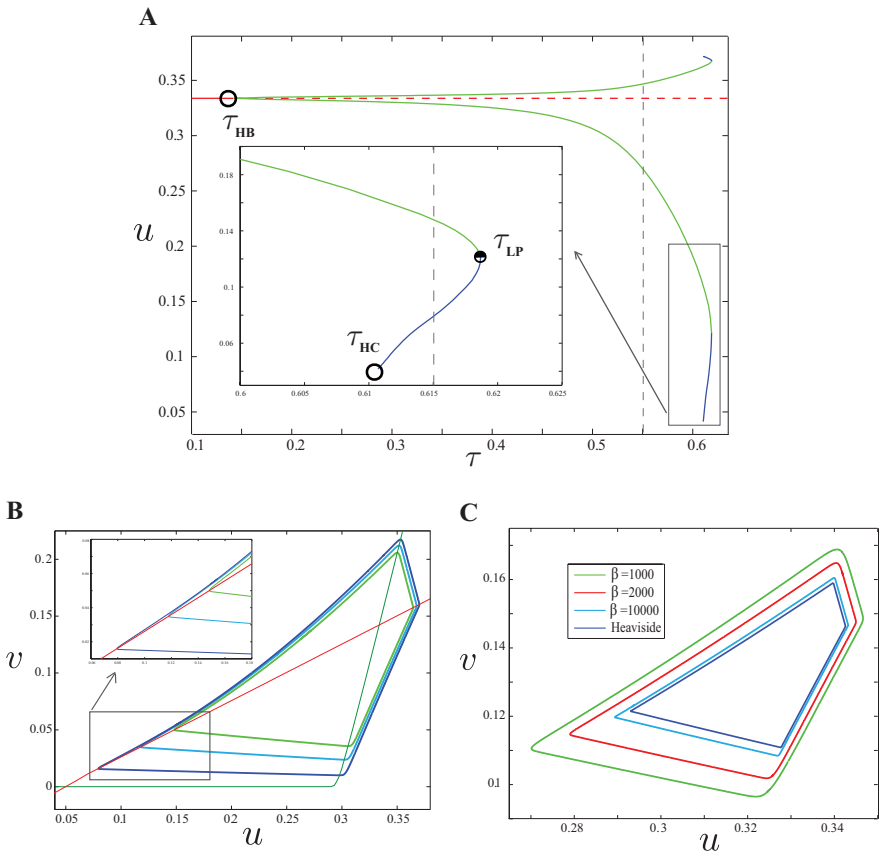

Figure 30: Convergence of smooth limit cycles. (A) The bifurcation diagram for smooth (logistic) firing rate function, taking $\beta = 1000$. We follow the maximum and minimum values of the u-component as τ varies. The solid, red line is the stable equilibrium, the dashed, red line is the unstable equilibrium, the green lines are stable limit cycles and blue lines, unstable limit cycles. Three bifurcations are shown: The Hopf at $\tau_{HB} \approx 0.1473$, the fold of limit cycles (SNLC) at $\tau_{LP} \approx 0.6189$ and the homoclinic at $\tau_{HC} \approx 0.6107$. An expanded view of the fold is shown in the inset. (B) The stable (green) and unstable (dark blue) limit cycles correspond to the intersection of the vertical, dashed lines found in the inset of the top panel ($\tau = 0.615$). The light blue is the SNLC. (C) A series of limit cycles for the smooth system, fixing $\tau = 0.55$ and increasing β. This shows the limiting tendency to the limit cycle of the Heaviside system, shown in dark blue.

the bottom, right panel of Fig. 30 indicates that the limit cycles in the smooth system converge to those in the nonsmooth system as β increases. The bottom left panel shows the stable (green) and unstable (blue) limit cycles near the fold ($\tau = 0.615$) and at the fold ($\tau_{LP} = 0.6189$). Comparing these limit cycles with those found in Fig. 28, there is a similar qualitative shape.

In Table 1, we compare the HB, HC, and SNLC bifurcations for the Heaviside, logistic and pwl systems, and the last column gives the length of the interval for which there are stable and unstable limit cycles:

Table 1: Bifurcation Table

Firing rate	β	τ_{HB}	τ_{HC}	τ_{LP}	$\tau_{LP} - \tau_{HC}$
Heaviside	—	0.5239	0.595	0.6073	0.0123
logistic	1000	0.1473	0.6107	0.6189	0.0082
pwl	1000	0.2513	0.4649	0.4679	0.0030
logistic	2000	0.1398	0.6039	0.6130	0.0091
pwl	2000	0.2506	0.4646	0.4674	0.0028

We see in Table 1 that even for such a large value of β, the Hopf bifurcation point is very different than that for the Heaviside model. However, despite this, the behavior for larger τ (away from the Hopf) is quantitatively similar for the logistic firing rate function. Indeed, we see from Figures 28 and 30 and Table 1 that once τ exceeds the value for the pseudo Hopf bifurcation of the nonsmooth system, the dynamics of the stiff, smooth system are quite similar. So, it remains to better understand why the Hopf bifurcation is so far away. Figure 31 offers some insight into this question. The bottom, right panel is a two–parameter diagram showing the curve of Hopf bifurcations in (β, τ) space for the nonlinear smooth functions as well as the pwl function. Hence, there are limit cycles above and to the right of these curves. For the pwl model, an analytic curve of Hopf bifurcations can be found by setting the trace of the autonomous linear system equal to zero. As the graph of a function,

we have

$$\tau_{HB}^{pwl}(\beta) = \frac{c\beta + 1}{\beta - 1} \ .$$

Interestingly, the $\lim_{\beta\to\infty} \tau_{HB}^{pwl}(\beta) = c$. Hence for the stiff pwl system, when fixing other system parameters, c is essentially what determines the supercritical Hopf. Hence, any increase in inhibitory-inhibitory connection strength will require slower dynamics in the v–component to lose stability and give rise to limit cycles.

It is quite clear from Fig. 31 that as $\beta \to \infty$, the curves asymptote to different values, so the limiting value of the Hopf *depends on the choice of the firing rate function*. Thus, we cannot expect that the loss of "stability" of the pseudo focus should occur at the same value of τ for the nonsmooth system and the point–wise limiting systems. Indeed, there is over a fourfold difference in τ_{HB} between the inverse tangent and error function choices.

In Fig. 30A, we observe the amplitude of the smooth limit cycles remains very small up to $\tau = 0.4$, which suggests that perhaps the actual amplitude of the limit cycle will tend to zero as β goes to infinity. This notion is further confirmed in panels A and B of Figure 31, which show the amplitude of the limit cycles for the logistic (left) and pwl (right) firing rate functions with $\beta = 1000$ (green) and $\beta = 2000$ (blue). The maxima and minima of the limit cycles for larger β are squeezed between those corresponding to lower β for *essentially* all $\tau \in (\tau_{HB}, \tau_{LP})$. Though this does not hold for τ close to τ_{HB}, if we take into account that the fixed point decreases with increasing β, then the amplitude of limit cycles for $\beta = 2000$ is bounded above by the amplitude for $\beta = 1000$. The log-log plot of β vs. the amplitude of the limit cycles in Fig. 31C illustrates this nicely. We see that the amplitude decreases with increasing β and tends to zero like $O(\beta^{-1})$ as $\beta \to \infty$ (indicated by the dashed lines) for both the pwl and logistic systems.

In the pwl model, for a fixed $\beta > 0$, there is a region in the (u, v) plane which includes the middle-branch fixed point. Indeed, this is the linear system for which we can compute the Hopf bifurcation. Hence, when the real part of the eigenvalues pass through the imaginary axis, the equilibrium is a linear center, so in a small neighborhood of the equilibrium, there is a continuum of periodic orbits which are bounded by an outermost periodic orbit. This orbit is half-stable in that trajectories with initial conditions in the exterior converge to it,

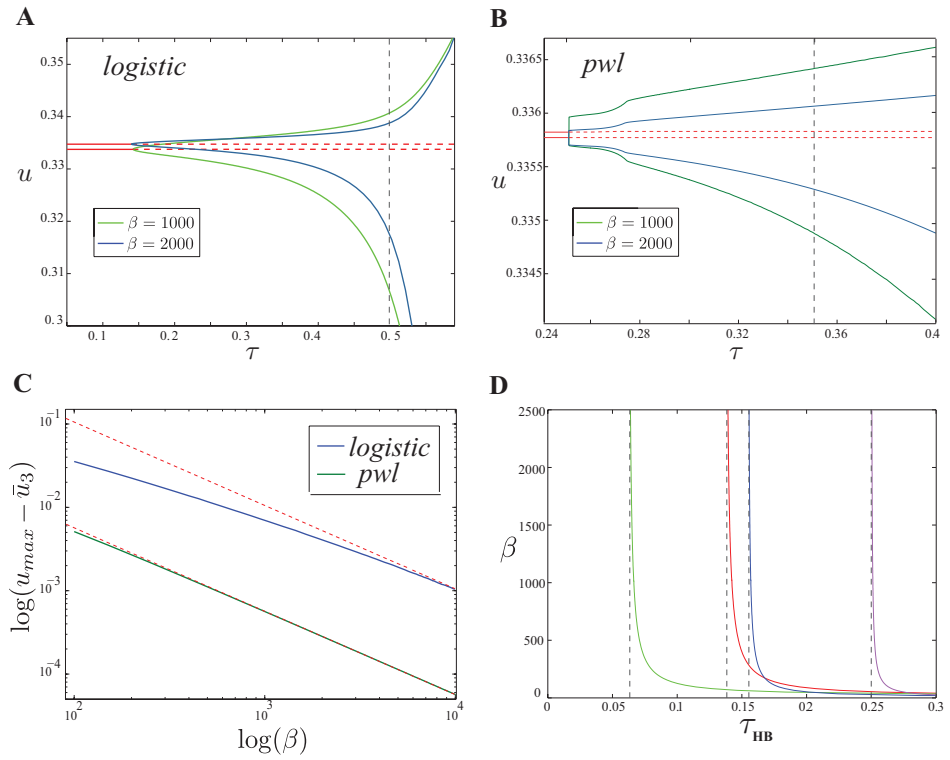

Figure 31: (A) The logistic firing rate, and (B) the piece–wise linear firing rate, taking $\beta = 1000$ (green) and $\beta = 2000$ (blue). We plot the maximum and minimum values of the u–component, following the stable limit cycles as τ varies. The solid (dashed) red line indicates the stable (unstable) equilibria, which are approximately $\bar{u} = 0.333759$ ($\beta = 1000$) and $\bar{u} = 0.334738$ ($\beta = 2000$) for the logistic and $\bar{u} = 0.335829$ ($\beta = 1000$) and $\bar{u} = 0.335772$ ($\beta = 2000$) for the pwl. (C) A log-log plot of β vs. the difference in the maximal value of the limit cycle and the fixed point for both the logistic and pwl system with values of τ indicated by a vertical dashed line in (A) $\tau = .5$ and (B) $\tau = .35$, respectively. (D) The co–dimension two bifurcation diagram, continuing the curve of Hopf bifurcations in (β, τ) space. The vertical, dashed lines mark the asymptotes at 0.633, 0.1555, and 0.1384 for the smooth functions inverse tangent, logistic, and error function, respectively, and $c = 0.25$ for the pwl system.

while trajectories with initial conditions in the interior neither tend toward nor away from it. Figure 31B shows the bifurcation diagram for the pwl system, fixing two values of $\beta >> 1$. For each curve of limit cycles, we see a vertical line at the Hopf bifurcation which illustrates the family of periodic orbits. This vertical line connects to the limiting maxima and minima of the stable limit cycles when taking $\tau \to \tau_{HB}^{+}$.

Now, to gain some insight into the scaling of the limit cycle amplitudes, we consider the simple, toy model:

$$\begin{aligned} x' &= \tanh(\beta(x - ay)) \\ y' &= (\tanh(\beta(x - cy))/\tau \ . \end{aligned} \tag{4.13}$$

The origin is the only fixed point and will be a node if $a > c$. There is a Hopf bifurcation at $\tau = c$. Using the same techniques as in Section 4.4.2, it is easy to show that for the nonsmooth system (with tanh replaced by the sign function) when $\tau < \sqrt{a\,c}$, then the origin is an attractor and if $\tau > \sqrt{a\,c}$ the origin is a repellor and all solutions wind out to infinity. Unlike the WC equations, the discontinuous system has no limit cycles.

Returning to the smooth system, multiply both equations by β, let $(u, v) = \beta\,(x, y)$ and rescale time via $s = \beta t$ to get

$$\begin{aligned} \dot{u} &= \tanh(u - a\,v) \\ \dot{v} &= \tanh(u - c\,v)/\tau \ . \end{aligned} \tag{4.14}$$

We have eliminated β, and we can now use numerical continuation to study the bifurcations of the system independent of β. We find that there is a supercritical Hopf bifurcation at $\tau = c$ and that the periodic solution persists until $\tau = \sqrt{a\,c}$ where it appears to become unbounded. For $c < \tau < \sqrt{a\,c}$, there is a periodic solution (at least numerically) to the (u, v) system. Since $x = u/\beta$, we see that as β gets large, the magnitude of the periodic solution is very small at least until τ reaches the neighborhood of $\sqrt{a\,c}$. This simple scaling argument gives a partial explanation of Figure 31 and provides some intuition about why the smooth HB is so far away from the pseudo HB for the discontinuous WC model.

4.7 DISCUSSION

In the first sections of this chapter, we have presented several discontinuity–induced bifurcations, which arise in the Wilson-Cowan equations as a result of the discontinuous firing rate function. As the image of the Heaviside step function is contained in the set $\{0, 1\}$, the firing rate function acts as an on–off switch determined by the relative activities of E and I populations. The u and v–switching boundaries provide a geometric description of these instantaneous switches. Parameters are such that the two boundaries intersect at a pseudo focus, $(\bar{u}_3, \bar{v}_3)$, which partitions the phase plane into four regions.

By letting the Heaviside step function be set–valued at zero, i.e. $H(0) \in [0, 1]$, the graph of the firing rate function is connected. Applying the Filippov Convexification Method, we were able to analytically verify the existence and stability of the sliding modes which we had previously observed in numerical simulations of the smooth, stiff system. In our analysis of the pseudo heteroclinic orbit, we found a condition on τ for which sliding exists for the entire length of the v–switching boundary. The pseudo equilibrium at $(\bar{u}_3, \bar{v}_3)$ changes from an *admissible* to a *virtual* pseudo focus as τ increases through a critical value. Partial sliding exists up to a critical value of u, after which the solutions fall off and spiral into the pseudo focus. Finally, for large enough τ, only transversal crossings occur along the v–switching boundary (Figure 25).

In our initial study of the pseudo focus $(\bar{u}_3, \bar{v}_3)$, we were uncertain of how to determine its stability. There was little to be found on pseudo equilibria occurring at the intersection of two switching manifolds in the nonsmooth literature. In fact, this subject is a current area of research (Mike Jeffrey, personal communication). A local expansion of the system near the intersection was found to be useful. Indeed, we discovered that the focal crossing goes through a pseudo Andronov–Hopf bifurcation at $\tau = \tau_{HB}$. Though there is no sense in which the real part of the eigenvalues of the linearized system go through the imaginary axis, others have found a generalized Hopf bifurcation of a pseudo focus located at a single switching manifold [44, 47, 81]. To show the pseudo Hopf, we defined the Poincaré map of the asymptotic expansion dynamics, and pieced together the solution lines. We obtained an analytic formula for $\tau_{HB} = \tau_{HB}(a, b, c, d, \bar{u}_3, \bar{v}_3)$ at which the Poincaré map has a fixed point.

In the discontinuous system of interest, this corresponds to the pseudo Hopf bifurcation.

We constructed the co–dimension one bifurcation diagram by numerically solving and continuing three separate boundary value problems with respect to τ: one for the stable limit cycle, one for the unstable limit cycle without sliding, and one for the unstable limit cycle with sliding. For a small range of τ values, a stable and an unstable limit cycle coexist till they collide at a turning point in the bifurcation diagram. We compared the bifurcation diagram of periodic solutions in the discontinuous Heaviside case to the stiff, smooth and pwl cases. The qualitative shape of the two bifurcation diagrams is similar, however, it seems that the discontinuous system shortens the parameter range of stable oscillations but increases it for unstable oscillations. This may be a result of the sliding modes found along the u–switching boundary in the Filippov system, a nice example of a DIB. The limit cycles of the discontinuous transitions from limit cycles without sliding modes to ones with sliding modes in a similar manner as the class of planar Filippov systems studied by Giannakopoulos & Pliete [27]. This so-called grazing–sliding bifurcation during a periodic orbit has been presented by di Bernardo et al. in a three dimensional illustration [13].

We find that a grazing bifurcation occurs at the pseudo homoclinic orbit, illustrating how the switching manifold may add instability and uncertainty to the system. At the pseudo homoclinic bifurcation, solutions starting at the tangency point of the u–switching boundary are non–unique in forward time (Fig. 27). Indeed, one solution slides into the pseudo saddle, and the other tends toward the origin with the latter being the stable solution. In their study of bifurcations in piecewise nonsmooth systems, Jeffrey and Hogan present the geometry of this *visible fold* bifurcation in which an orbit visibly grazes a switching boundary with stable sliding [40].

We compared the limit cycle bifurcations of the nonsmooth system to those of the smooth system. We found that the nonsmooth system has similar dynamics to that of its smooth counterpart, at least for sharp enough nonlinearities, but the loss of stability of the fixed point occurs through quite different mechanisms. In the smooth case, there is the usual Hopf bifurcation and as $\beta \to \infty$, this point converges to a specific value that depends on the choice of nonlinearity, as seen in Fig. 31D. As shown in Fig. 30, the magnitude of the limit cycles is nearly zero up until a critical value of τ, which seems to occur near $\tau = \tau_{HB}$, i.e. near

the pseudo Hopf for the nonsmooth system. This seems to hold for other smooth functions as well, and we show the small oscillations of the pwl model in Fig. 31B. In Fig. 31C, a log-log scale plot of β versus limit cycle amplitude shows how the amplitude decreases with increasing β for both the logistic and pwl firing rate models. The dashed line is the log-log plot of β versus $1/\beta$, translated to include the minimal amplitudes for the logistic and pwl curves. Numerical integration seems to be consistent with the scaling predicted with the toy model, that is, the amplitude of the stable limit cycles approaches zero asymptotically like $1/\beta$ as $\beta \to \infty$. The nonlinear logistic requires much larger β to observe this behavior, while the pwl model has this trend for smaller β.

We extended our analysis to include the stiff, pwl system, and though we have given an equation for the curve of Hopf bifurcations in (τ, β) space, much of the results were presented using numerical integration, some of which proved to be difficult for two main reasons. Firstly, the pwl firing rate function given in section 4.6 splits the direction field into *nine* regions in the plane, so setting up a boundary value problem would require a lot of bookkeeping to track which regions the trajectory realizes. Secondly, as the system has "corners", we cannot apply the usual numerical continuation methods to obtain the single-parameter bifurcation diagrams. Despite the numerical challenges, the pwl system has some interesting behaviors. For instance, the Andronov–Hopf bifurcation occurs at a linear center, for which a small neighborhood of the equilibrium contains a family of periodic solutions. This corresponds to a vertical line in the bifurcation diagram in Fig. 31 whose endpoints meet with curve of stable limit cycles at a nonsmooth corner. Though there is some further analysis to be done on the pwl model, most of the results would be (more or less) expected, which explains the somewhat brief study of it here.

Lastly, we showed the pseudo saddle-node on an invariant circle bifurcation, taking the disinhibition b to be the bifurcation parameter. This bifurcation has no hidden sliding modes. In fact, it is rather similar to the SNIC bifurcation of the smooth system, suggesting this bifurcation is not discontinuity-induced. The reason it is not a true SNIC, however, is that a *pseudo* saddle at $(b, 0)$ collides with the node at the origin.

Throughout this manuscript, we have for the most part fixed the parameters, a, b, c, d which relate to thresholds and coupling strengths. We focused our attention on changes

in the relative timescale between excitation and inhibition. The main reason for this is the time scale τ has no effect on the values of the equilibria and pseudo equilibria. Thus, changes in dynamics are not attributable to changes in the number of equilibria but in their stability. Of course, we could easily fix τ and vary the other parameters and see similar types of bifurcations. For example, Fig. 24 shows two parameter curves of the pseudo Hopf, plotting τ_{HB} against a, b, c, and d. Since the values of τ for which various sliding and grazing bifurcations occur can depend on distance along the switching boundary from the pseudo focus, it is clear that fixing τ and varying another parameter, say a, can have a similar effect. It is easy to determine the loss of pseudo equilibria, as we need only determine whether the intersection of the switching boundaries occurs at a point in the interior of the unit square $(0,1) \times (0,1)$. Pseudo saddles will always occur at points where either $v = 0$ or $v = 1$. It would be interesting to continue the homoclinic orbits in two parameters to also explore how these may be gained and lost.

Recently, Coombes et al. revisited the so-called integrate–and–fire single neuron spiking model and showed several nonsmooth bifurcations. For instance, the model has threshold parameters at which voltage (and adaptive current dynamics) are instantaneously reset, and grazing bifurcations occur when the trajectories tangentially approach these values [8]. In a similar vein, we revisit the classical WC model from a nonsmooth systems perspective. The difference here is the discontinuities are found in the system derivatives (and not in the variables themselves), and as such, we find a different variety of discontinuity–induced bifurcations. For a parameter regime in which there exists an inhibitory–stabilized network state (in the smooth system), the ISN state exists as a focal crossing of two switching manifolds (in the nonsmooth system) which gives rise to complicated transitions and nonsmooth bifurcations.

5.0 PIECEWISE CONSTRUCTION OF WAVES IN THE NONSMOOTH SPATIALLY-DISTRIBUTED WILSON-COWAN EQUATIONS

5.1 INTRODUCTION

As mentioned in Chapter 4, mathematical neuroscientists have often used the Heaviside step function to facilitate in the analysis of patterns, such as "bumps" and waves, in spatially-distributed neural field models. Typically, the transfer function is found under the spatial integral so that these patterns can be truncated to a compact spatial region [1, 9, 58]. In this chapter, we use similar techniques to analyze traveling pulses of the nonsmooth spatially-distributed model. We found in Chapter 3 that these waves seem to exist for large enough time constant of inhibition and find evidence through simulation that they also exist in the nonsmooth version of the model, when the firing rate function is the Heaviside step function. We limit our study to local inhibition and consider the exponential kernel as in Chapters 2 and 3.

5.2 THE PULSE

We can study the traveling pulse solution in the traveling wave frame, $\xi = x + \eta\, t$. Hence, we obtain a 4D system of differential equations in the traveling wave variable which is given by

$$
\begin{aligned}
u' &= \left(-u + H(w - a\,v - b)\right)/\eta \\
v' &= \left(-v + H(w - c\,v - d)\right)/\left(\eta\,\tau\right) \\
w' &= z \\
z' &= (w - u)/\sigma_e^2 \ ,
\end{aligned}
\tag{5.1}
$$

where the parameters a, b, c, d have the same values as in Chapter 4. This is essentially the system in Eq. (3.2), replacing the smooth firing rate function with the Heaviside step function (denoted by $H(u)$).

From our analysis in Chapter 4, we expect the stability of the up state to depend on the time constant of inhibition, τ. We see in Fig. 28 that the up state goes through a pseudo Hopf bifurcation that gives rise to limit cycles that terminate at a pseudo homoclinic bifurcation. With this in mind along with our results on the traveling pulse of the smooth system in Chapter 3, we look for traveling pulse solutions when the time constant of inhibition is larger than the value of the homoclinic bifurcation.

We find two types of traveling pulses, with the only difference being that for smaller values of τ, there is a sliding mode along the switching manifold defined by $w - a\,v - b = 0$ above the up state. We can solve for these types of solutions by setting up an appropriate boundary value problem for which the switching manifolds yield boundary conditions that put the solution on a *bounded domain*.

We first look at the traveling pulse when $\tau > 0.82$, which ensures that there is no sliding. The pulse can be understood by looking at the four pieces shown in Fig. 32A, with the essential pieces labeled 1 and 2. We can start the boundary value problem with $u = v = z = 0$ and $w = b$ so that u increases while v remains zero (piece 1, light blue). Once w hits the threshold for inhibition ($w = d$), v begins to increase (piece 2, dark blue). The firing rates for both excitation and inhibition increase till the trajectory hits the switching manifold given by $w - a\,v - b = 0$, turning off excitation thereafter. Thus, the boundary conditions that close the system are given by

$$
\begin{aligned}
w_2(1) - a\,v_2(1) - b &= 0 \\
w_2(1) + z_2(1) - \frac{\eta}{1+\eta}\,u_2(1) &= 0 \ ,
\end{aligned}
\tag{5.2}
$$

where evaluating at 1 indicates the end of the trajectory. The two conditions ensure that the trajectory hits the switching manifold, $w - a\,v - b = 0$, while intersecting with the stable manifold of the origin. We fill in the rest of the pieces to the solution (piece 3 in orange; piece 4 in black) using continuity conditions at the switching manifolds. The fourth piece (black) asymptotically approaches the origin, so we integrate this for a long time to obtain a decent picture of the solution.

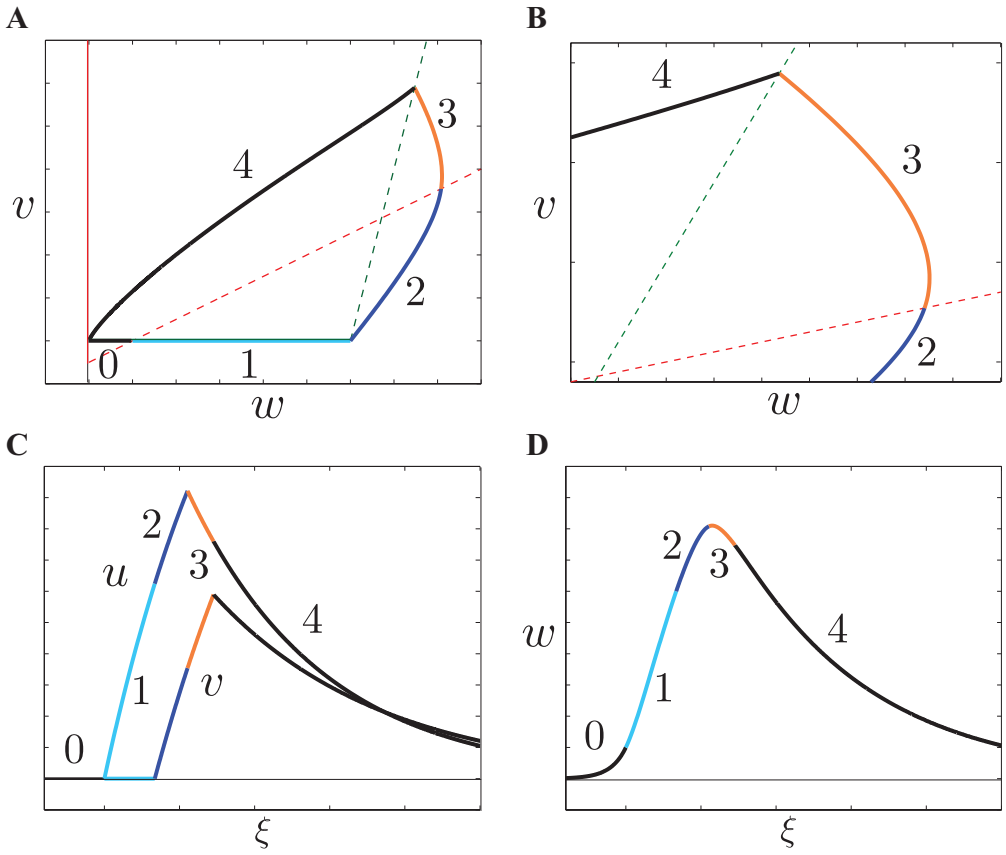

Figure 32: The pulse (no sliding dynamics). (A) Projection onto w-v plane with switching manifolds for u (dashed red) and v (dashed green). (B) Zooming in on the pieces above the up state equilibrium. (C) The u-v trajectories against ξ. (D) w against ξ.

Decreasing τ so that $0.755 < \tau < 0.82$, we have a traveling pulse with a piece of sliding along the manifold $w - c\,v - d = 0$ (above u_3) before the firing rates exponentially decay to zero. We still have to satisfy the conditions of Eq. (5.2) except now there is a sliding trajectory (piece 4, violet) between pieces 3 (orange) and 5 (black) with the dynamics given by the sliding parameter $\alpha \in [0,1]$, $\alpha = v + \frac{\eta\tau}{c}\,z = \frac{w-d}{c} + \frac{\eta\tau}{c}\,z$ (see Chapter 4 for how to compute α). We show this type of traveling pulse solution in Fig. 33 for $\tau = 0.755$. For the inset in Fig. 33B, we plot the sliding parameter α and the value of $h = w - c\,v - d$. The sliding portion ends at a tangency point ($\alpha = 0$) after which v decreases back to rest (piece 5, black).

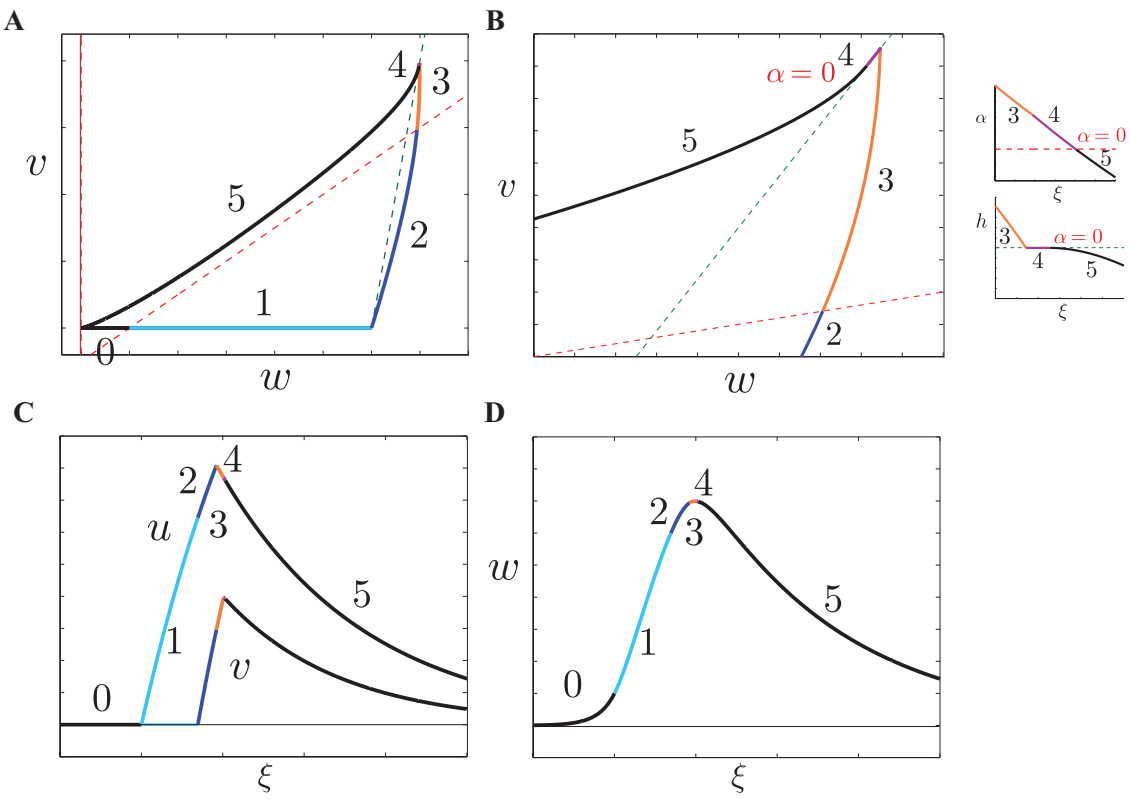

Figure 33: The Pulse solution (sliding dynamics). (A) Projection into w-v plane with switching manifolds for u (dashed red) and v (dashed green). (B) Zooming in on the pieces above the up state equilibrium with insets showing the sliding parameter α and the value of h. (C) The u-v trajectories against ξ. (D) w against ξ.

5.3 DISCUSSION

Taking the firing rate function to be the Heaviside step function simplifies the analysis of the traveling pulse solution so that we can analytically solve for the pulse solution using a boundary value problem. Though we do not have a complete picture of the types of traveling waves seen in this nonsmooth system, we were able to construct two types of traveling pulse solutions, one of which contained a sliding mode. Future work could be done to look for traveling front solutions similar to those found in the smooth spatially-distributed system in Chapter 3. This may prove to be quite complicated because of pseudo equilibrium occurring at the intersection of two switching manifolds. In addition, one might consider the spatially-distributed system with nonlocal inhibitory connections, which adds two dimensions to the system along with another parameter for the spatial scale. It would be interesting to see if sliding dynamics occur in this system and how they affect the wave speed. Lastly, it would be interesting to see how the traveling waves of the nonsmooth spatially-distributed system compare with the smooth system.

6.0 CONCLUSION

Since each chapter concludes with a discussion of the main results, we keep our concluding remarks brief, summarizing our results and describing future directions. Throughout this document, we have analyzed a spatially-distributed mean field model of the population average activities of interacting excitatory and inhibitory neurons. We fixed parameters so that the space-clamped system has a phase plane in which the active state is associated with an equilibrium point that lies on the middle branch of the cubic-shaped nullcline of the excitatory population. This equilibrium is a stable steady-state of the system for small time constants of inhibition, τ, and represents the inhibitory stabilized network (ISN) state. The equilibrium becomes unstable through a Hopf bifurcation as the time constant increases.

In Chapter 2, we studied spatio-temporal pattern formation when the system has a bulk oscillation around the up state. While many studies of pattern formation arise from instabilities to the spatially-homogeneous steady-state (i.e. from the fixed point), we analyze instabilities to the limit cycle oscillation and show doubly-periodic patterns that depend on both the spatial and temporal variables. In this study, we computed analytical curves that serve as boundaries for the pattern-forming regions in parameter space and compared these with the discretized network simulations. We also varied the threshold for excitation with and without the presence of a down state. When there is a down state equilibrium, the space-clamped system goes through a homoclinic bifurcation as τ further increases and no limit cycles exist past this point. Interestingly, we found that the system can still support spatio-temporal patterns, which may have something to do with the bistable behavior between the traveling front and pulse found in Chapter 3. This might be a topic for future investigation.

In Chapter 3, we considered the spatially-distributed network when the space-clamped

system had a spatially-homogeneous down state and studied down to up state transitions of the network, which correspond to traveling fronts. By setting up an appropriate boundary value problem and using continuation methods, we were able to follow these solutions with respect to the temporal and spatial scales of the system. In the presence of a bulk oscillation, the network simulations tend to a synchronous oscillation while the boundary value problem follows solutions that connect to the stable manifold of the up state and asymptotically approach the fixed point. We suspect that the solutions of the boundary value problem are unstable, though they give decent approximations of the wave velocity of traveling fronts in the network simulations. For larger values of τ, the traveling fronts approach the sorts of spatio-temporal patterns found in Chapter 2. For even larger τ, there exist traveling pulses in which a wave of excitation propagates across the network that returns back to the down state. Then a natural question is what happens for intermediate values of τ. We found bistability between these two behaviors and the tendencies depended on the time duration of the initial stimulus. Possible future work might be to study the network when there are time-dependent or spatially-dependent input currents for the various parameter regimes. Depending on the problem at hand, one might include noisy inputs to the system and study the transitions between states of the deterministic model.

In Chapter 4, we studied the phase plane of the space-clamped model with the Heaviside firing rate function. We found several bifurcations of the nonsmooth system that are analogous to the bifurcations in the smooth system. We also compared several models with differing firing rate functions (e.g. the logistic, hyperbolic tangent, and piecewise linear functions) that limit to the nonsmooth system. With a general understanding of the nonsmooth WC equations, we studied the spatially-extended version of the nonsmooth system in Chapter 5. We were able to construct approximate solutions of the traveling front for small τ by defining the sliding dynamics and solving an appropriate boundary value problem. For larger values of τ, the trajectory spirals into the up state so that there are an infinite number of pieces to solve for in the boundary value problem. For large enough τ, we can analytically solve for the traveling pulse, since the solution can be truncated by an end condition that corresponds to the trajectory hitting the stable manifold of the down state. In the phase diagram, the curve of front solutions smoothly meets the curve of pulse solutions as τ in-

creases. These curves meet near the homoclinic bifurcation, above which we find bistability between the front and pulse in network simulations. The bistability was obtained by changing the initial stimulus input in a similar manner as we did in the smooth system, but the the nonsmooth traveling front does not seem to leave patterns in its wake. In this study, we only considered spatially-distributed connections in the excitatory population, so future work would be to include spatially-distributed connections in the inhibitory population as well. Another possible direction is to study how the traveling wave solutions change as a result of increasing the gain parameter, β, and it might be interesting to compare the waves for large β with the nonsmooth construction.

APPENDIX A

SPATIO-TEMPORAL PATTERN FORMATION

A.1 LINEAR STABILITY FROM A SPATIALLY HOMOGENEOUS EQUILIBRIUM

Here we show how to find parameters to obtain pattern formation when $\sigma_e > \sigma_i$ in the WC network with spatial coupling, when considering perturbations from a spatially uniform equilibrium. We make a change of variables to make it easier to explicitly find parameters and consider:

$$\begin{aligned} u_t &= -u + g_e(a_{ee}K_e(x) \star u - a_{ei}K_i(x) \star v) \\ \tau v_t &= -v + g_i(a_{ie}K_e(x) \star u - a_{ii}K_i(x) \star v)\,, \end{aligned} \tag{A.1}$$

where $g_\mu(J) = (f(J-\theta_\mu) - f(-\theta_\mu))/f'(-\theta_\mu)$ for $\mu = e, i$. (We can readily change to the usual WC equations with a linear change of variables.) This convenient transformation assures that $g_\mu(0) = 0$ and $g'_\mu(0) = 1$. As usual, we suppose that $K_\mu(x) = K(x/\sigma_\mu)/\sigma_\mu$ so that the shapes of the interaction kernels are the same up to a space constant. Let $H_\mu(\omega)$ be the Fourier transform of the kernels, which are normalized so that $H_\mu(0) = 1$. If $\sigma_e < \sigma_i$, then $H_e(\omega) \geq H_i(\omega)$ with equality only at $\omega = 0$. When we linearize around the homogeneous state $(0, 0)$ and take the Fourier transform we see that the resulting matrix (parameterized by ω) has a determinant proportional to

$$D(\omega) = 1 + a_{ii}H_i(\omega) + (a_{ei}a_{ie} - a_{ii}a_{ee})H_e(\omega)H_i(\omega) - a_{ee}H_e(\omega)\,. \tag{A.2}$$

We want the determinant to be positive for ω near zero and then to become negative for some interval of ω bounded away from 0. We also require that the trace be negative, but since the trace is $-1 + a_{ee}H_e(\omega) - (1 + a_{ii}H_i(\omega))/\tau$, we can always choose τ small enough to ensure that this is negative for all ω. Strictly speaking, we require only that $D(0) > 0$, but in practice, it is generally true that $Q := a_{ei}a_{ie} - a_{ee}a_{ii}$ is also positive. Note that for any reasonable kernels, $H_e(\omega) \to 0$ as $\omega \to \infty$ so that $D(\omega) > 0$ for ω large. We can write the determinant as

$$D(\omega) = 1 + (a_{ii} + QH_e(\omega))H_i(\omega) - a_{ee}H_e(\omega)\,,$$

which makes it clear that decreasing σ_i (increasing $H_i(\omega)$) always makes the determinant more positive and thus pulls the system away from pattern forming instabilities.

A.2 CONDITIONS ON PARAMETERS FOR PATTERN FORMATION WITHOUT LATERAL INHIBITION

Now we want $D(\omega)$ to have a negative minimum value at some value of ω while staying positive when $\omega = 0$. To obtain pattern formation without lateral inhibition, we will set $\sigma_e = \sigma_i$ and then if $D(\omega)$ falls below zero, by continuity, we can choose $\sigma_i < \sigma_e$ so that $D(\omega) < 0$. Now let $w = H_e(\omega) = H_i(\omega)$ and $b = a_{ee} - a_{ii}$ so that $D(\omega) = 1 - bw + Qw^2$. We require that this quadratic have a local minimum at some value of $w \in (0, 1)$. Then the extremum is $w_{min} = b/(2Q)$, and this is a minimum only if $Q > 0$, as we assumed. Then we must have $Q > b/2$, since $w_{min} \in (0, 1)$. Evaluating $D(\omega)$ at the minimum, we have

$$D(\omega_{min}) = 1 - b^2/(2Q) + b^2/(4Q) = 1 - b^2/(4Q)\,.$$

Since this must be negative and $D(1) = 1 - b + Q > 0$, we obtain 3 constraints: (1) $Q > b - 1$, (2) $Q > b/2$, and (3) $Q < b^2/4$, where only (1) and (3) matter. That is, we need

$$b - 1 < Q < b^2/4\,. \tag{A.3}$$

If we choose parameters so that (A.3) is satisfied, then we should be able to obtain pattern formation when $\sigma_i = \sigma_e$. So by continuity, we can find parameters for pattern formation

from a spatially homogeneous equilibrium point when σ_i is slightly less than σ_e. Note that this is all in the linearized regime, and so, we must be careful that the nonlinearities do not prove to be an issue (e.g. we get subcritical bifurcations or other homogeneous equilibria).

A.3 NO SPREAD OF INHIBITION

We close with a remark that with *no spread* of inhibition ($\sigma_i = 0$), there can be no pattern forming instability from a homogeneous equilibrium for then equation (A.2) becomes:

$$D(\omega) = 1 + a_{ii} + (a_{ei}a_{ie} - a_{ii}a_{ee} - a_{ee})H_e(\omega).$$

This is monotonic in ω so there can be no value of $\omega > 0$ where $D(0) > 0$ and $D(\omega) < 0$.

APPENDIX B

TRAVELING WAVES

B.1 THE LINEARIZATION OF THE 4D AND 6D SYSTEMS

In this section of the appendix we show that in the 4D system, both the up and down states have a one-dimensional unstable subspace and a three-dimensional stable subspace. We then show that for the 6D system, there is a two-dimensional unstable space and a four-dimensional stable space for both fixed points. We first analyze linearizations of the 4D system at the up and down states. Putting $\sigma_e = 1$, the characteristic polynomial corresponding to the 4D linearization around the up and down-states is of the form

$$p(\lambda) = \lambda^4 + A_3\,\lambda^3 + A_2\,\lambda^2 + \,A_1\lambda + A_0 \ ,$$

where

$$A_3 = \frac{1}{\eta}\left(1 + \frac{(1+b_{ii})}{\tau}\right) \quad , \quad A_2 = \frac{1}{\eta^2}\left(\frac{(1+b_{ii})}{\tau} - \eta^2\right)$$
$$A_1 = -\frac{1}{\eta}\left((1-b_{ee}) + \frac{(1+b_{ii})}{\tau}\right) \quad , \quad A_0 = -\frac{1}{\eta^2\,\tau}\,\left((1-b_{ee})(1+b_{ii}) + b_{ie}\,b_{ei}\right) \ .$$

Note that $A_3 > 0$, and for $0 < \tau < \tau_{HB}$, we have that $A_1 \equiv \frac{Tr(0)}{\eta} < 0$ and $A_0 = -\frac{D(0)}{\eta^2} < 0$, where $Tr(0)$ and $D(0)$ denote the trace and determinant of the space-clamped system. Now the sign of A_2 depends on the parameters τ and η. Nonetheless, there is one sign change between the coefficients, so applying Descartes' rule of signs, we have exactly one positive root. Looking at $p(-\lambda)$, we have three sign changes (regardless of the sign of A_2), so

Descartes' rule gives three or one negative roots.

Around the *down-state*, we found numerically that for the given parameters $\bar{u} = 2.1443 \times 10^{-3}$ and $\bar{v} = 2.2944 \times 10^{-9}$. Hence the terms $b_{ee} = a_{ei}\beta\bar{v}\,(1-\bar{v})$ and $b_{ei} = a_{ei}\beta\bar{v}\,(1-\bar{v})$ are of order $O(10^{-1})$, while the terms $b_{ie} = a_{ie}\beta\bar{v}\,(1-\bar{v})$ and $b_{ii} = a_{ii}\beta\bar{v}\,(1-\bar{v})$ are of order $O(10^{-7})$. Setting $b_{ie} = b_{ii} = 0$, a good approximation for the characteristic polynomial is

$$p(\lambda) = \lambda^4 + \frac{1}{\eta}\left(1+\frac{1}{\tau}\right)\lambda^3 + \frac{1}{\eta^2}\left(\frac{1}{\tau} - \eta^2\right)\lambda^2 - \frac{1}{\eta}\left((1-b_{ee}) + \frac{1}{\tau}\right)\lambda - \frac{(1-b_{ee})}{\eta^2\,\tau}\ ,$$

which has a zero at $\lambda = -\frac{1}{\eta\,\tau} < 0$. We further factor to obtain,

$$p(\lambda) = \left(\lambda + \frac{1}{\eta\,\tau}\right) q(\lambda)\ ,$$

where $q(\lambda) = \lambda^3 + \frac{1}{\eta}\lambda^2 - \lambda - \frac{(1-b_{ee})}{\eta}$. Since $q(\lambda)$ has exactly one positive root, then the remaining two roots are either negative or form a complex conjugate pair. Note that $q\left(-\frac{1}{\eta}\right) = \frac{b_{ee}}{\eta} > 0$ and $q(0) = -\frac{(1-b_{ee})}{\eta} < 0$, so by the Intermediate Value Theorem, there is at least one real root on the interval $(-\frac{1}{\eta}, 0)$, which then gives two negative roots of $q(\lambda)$. Hence the down-state has a three dimensional stable manifold and one dimensional unstable manifold.

If we homotopy from the down to up-state so that the coefficients b_{ij} move (continously) away from zero, then we can follow (continuously) the roots of the resulting family of polynomials. Now we want to show that the three dimensional stable manifold is preserved under this homotopy. Around the up-state, Descartes' rule of signs still gives a one positive root and (at least) one negative root of $p(\lambda)$ when $0 < \tau < \tau_{HB}$, so we consider how the two additional negative roots starting in the down-state can pass through the imaginary axis. One case is through a zero eigenvalue, which is not possible, since $A_0 < 0$. The other is through a complex conjugate pair passing through the imaginary axis, in which case there must be a point when the real part is zero and the pair is of the form $\lambda = \pm\omega\,i$ with $\omega \in \mathbb{R}$. Looking at $p(\omega\,i)$, the imaginary terms must cancel, so we have the necessary condition: $-A_3\,\omega^2 + A_1 = 0$. Since $A_3 > 0$ and $A_1 < 0$, this is impossible. Hence, the up-state has a three dimensional stable manifold and one dimensional unstable manifold.

Now we study the 6D linearization and use similar arguments as in the 4D linearization

to show that for certain values of τ and $\sigma = \sigma_e/\sigma_i$ the up and down-states have four dimensional stable manifolds and two dimensional unstable manifold. We write the characteristic polynomial:

$$f(\lambda) = \lambda^6 + C_5\,\lambda^5 + C_4\lambda^4 + C_3\,\lambda^3 + C_2\,\lambda^2 + C_1\lambda + C_0 \ ,$$

where

$$C_5 = \frac{1}{\eta\,\tau}\,(1+\tau) \ , \quad C_4 = -1 - \frac{1}{\sigma^2} + \frac{1}{\eta^2\,\tau} \ ,$$

$$C_3 = -\frac{1}{\eta}\left(1 - b_{ee} + \frac{1}{\tau} + \frac{1}{\sigma^2}\left(1 + \frac{1+b_{ii}}{\tau}\right)\right) \ , \quad C_2 = -\frac{1}{\eta^2\,\tau}\left(1 - b_{ee} + \frac{1}{\sigma^2}\left(\eta^2\,\tau + 1 + b_{ii}\right)\right) \ ,$$

$$C_1 = \frac{1}{\eta\,\sigma^2}\left(1 - b_{ee} + \frac{1+b_{ii}}{\tau}\right) \ , \quad C_0 = \frac{1}{\eta^2\,\sigma^2\,\tau}\left((1-b_{ee})(1+b_{ii}) + b_{ie}\,b_{ei}\right) \ .$$

Note that $C_5 > 0$. Also, for $0 < \tau < \tau_{HB}$, $C_1 = -\frac{Tr(0)}{\eta\,\sigma^2} > 0$ and $C_0 = \frac{D(0)}{\eta^2\,\tau^2} > 0$. If in addition $0 < \sigma < 1$, then $C_3 < 0$. Independent of the sign of C_4, we have two sign changes when ordering the coefficients. Hence, we have either two or zero positive roots. Considering $f(-\lambda)$, we see that there are four sign changes, which gives four, two, or zero negative roots. Setting $b_{ie} = b_{ii} = 0$ as before, we obtain an approximation for the characteristic polynomial around the down-state:

$$g(\lambda) = \left(\lambda^2 - \frac{1}{\sigma^2}\right)\,p(\lambda) \ .$$

Hence, we gain two real roots: One positive and one negative. Then the down-state has a four dimensional stable manifold and a two dimensional unstable manifold. Using a similar homotopy argument as in the 4D linearization, we can show this stability structure is preserved as we move b_{ie} and b_{ii} away from zero. A positive eigenvalue cannot be gained from a negative eigenvalue, as $C_0 = \frac{D(0)}{\eta^2\,\tau^2} > 0$. Now suppose a complex conjugate pair (with negative real part) passes through the imaginary axis, i.e. $\lambda = \pm\omega\,i$ with $\omega > 0$ at some point. Looking at $g(\omega\,i)$, we must have $0 = C_5\,\omega^4 - C_3\,\omega^2 + C_1 = C_5\,(\omega^2)^2 - C_3\,(\omega^2) + C_1$, but since $C_5 > 0$, $C_3 < 0$ and $C_1 > 0$, there are no positive roots. Hence there is no solution such that ω is real, and so, purely imaginary eigenvalues are not possible. Thus, both the

up and down-states have four dimensional stable manifolds and two dimensional unstable manifolds.

B.2 A HOMOTOPY FROM LOCAL TO NONLOCAL INHIBITION

Briefly, we describe our continuation methods to obtain traveling wave solutions of the 6D system in Eq. (3.4). Let $v_\lambda := (1-\lambda)\, v + \lambda\, q$ with homotopy parameter $\lambda \in [0,\, 1]$. We write the system:

$$\begin{aligned} \eta\, u' &= (-u + F(a_{ee}\, w - a_{ei}\, v_\lambda - \theta_e)) \\ (\eta\, \tau)\; v' &= (-v + F(a_{ie}\, w - a_{ii}\, v_\lambda - \theta_i)) \\ w' &= z \\ z' &= (w - u) \\ q' &= r \\ r' &= (q - v)/\sigma^2 \ . \end{aligned} \tag{B.1}$$

When $\lambda = 0$, we have $v_{(\lambda=0)} = v$ so that the first four equations are decoupled from the last two, and this becomes a more manageable shooting problem (varying $\eta > 0$) for Eq. (3.2). The last two equations see the dynamics of v and have one dimensional stable and unstable manifolds. Once $\eta > 0$ is fixed, the dynamics for v are approximated and we can vary $\sigma > 0$ to solve for the heteroclinic or homoclinic orbit in the $(q,\, r)$ system. With an initial approximation of the orbit, we make the 'period' larger. In practice, before coupling the (u, v, w, z) system by continuing λ from 0 to 1, the parameter $\sigma > 0$ may need to be decreased. In the figure below we illustrate the homotopy of heteroclinic solutions for $\sigma = 0.9$, $\tau = 0.1$ by plotting the trajectory in the u-v and q-r planes and increasing the homotopy parameter λ from 0 to 1.

B.3 ANALYSIS OF STANDING WAVES

In Fig 17, we see that for $\tau > 0$ large enough the speed of the traveling pulse goes to zero as $\sigma > 0$ increases. Analytically, these waves correspond to $\eta = 0$ so that the time-invariant solutions $u(x)$, $v(x)$ can be put in terms of $(w,\, z,\, q,\, r)(x)$:

$$\begin{aligned} u(x) &= F(a_{ee}w(x) - a_{ei}q(x) - \theta_e) \\ v(x) &= F(a_{ie}w(x) - a_{ii}q(x) - \theta_i) \end{aligned} \tag{B.2}$$

where the remaining variables $(w,\, z,\, q,\, r)(x)$ satisfy

$$\begin{aligned} w' &= z \\ z' &= (w - u) \\ q' &= r \\ r' &= (q - v)/\sigma^2\,, \end{aligned} \tag{B.3}$$

with the boundary conditions,

$$\lim_{x\to\pm\infty} (w,\, z,\, q,\, r)\,(x) = (\bar{u},\, 0,\, \bar{v}, 0)_1 \ .$$

This is a 4D nonlinear differential equation with $' = \frac{d}{dx}$. Since these are time-invariant solutions, the temporal scale τ is no longer a parameter of the system. The linearization around the down-state and corresponding eigenvectors are

$$\begin{pmatrix} 0 & 1 & 0 & 0 \\ 1 - b_{ee} & 0 & b_{ei} & 0 \\ 0 & 0 & 0 & 1 \\ -b_{ie}/\sigma & 0 & (1 + b_{ii})/\sigma & 0 \end{pmatrix}, \quad \begin{pmatrix} b_{ei} \\ \lambda\, b_{ei} \\ (\lambda^2 + b_{ee} - 1) \\ \lambda\,(\lambda^2 + b_{ee} - 1) \end{pmatrix},$$

where the eigenvalues satisfy

$$\lambda^4 - (1 - b_{ee} - (1 + b_{ii})\,/\sigma)\ \lambda^2 + (1 - b_{ee})\,(1 + b_{ii})/\sigma + b_{ie}\, b_{ei}/\sigma = 0\ .$$

Hence,

$$\lambda^2 = \frac{\left(1 - b_{ee} - (1 + b_{ii})/\sigma\right) \pm \sqrt{\left(1 - b_{ee} - (1 + b_{ii})/\sigma\right)^2 - 4\left(\left(1 - b_{ee}\right)(1 + b_{ii})/\sigma + b_{ie}\, b_{ei}/\sigma\right)}}{2} ,$$

which are both real and positive. Hence the eigenvalues take the form $\pm\sqrt{c_1}$ and $\pm\sqrt{c_2}$ where c_1, $c_2 > 0$, and the down-state E_d has two positive and two negative eigenvalues. Unfortunately, numerically obtaining a homoclinic orbit connecting the two dimensional unstable manifold to the two dimensional stable manifold of the down-state is a difficult task, since initial perturbations of the trajectory should be linear combinations of the eigenvectors corresponding to the unstable directions, which depend on the parameter $\sigma > 0$.

B.4 ANALYSIS OF 2D TRAVELING WAVES: A REDUCTION TO 1D

A possible method for analyzing the traveling waves found in our 2D spatial model is to exploit the radial symmetry of traveling waves initiated by a circular-shaped stimulus located at the center of the media. The strategy is to convert the system to polar coordinates, wherein the convolutions become special functions and the spatial dimension is reduced to one. Since these waves are independent of the polar angle, we can integrate out the angle to define the kernel

$$J(r, r') = \frac{2\pi}{\sigma^2} \exp\left(-\frac{r^2}{2\sigma^2}\right) I_0\left(\frac{r\, r'}{\sigma^2}\right) \left[r' \exp\left(-\frac{r'^{\,2}}{2\,\sigma^2}\right)\right] ,$$

where $I_0(x) = \int_0^\pi \exp\left(x\, \cos(\phi)\right)\, d\phi$ denotes the modified Bessel Function of the first kind. Then the 2D spatial convolution terms become radially-dependent 1D integrals:

$$(K \star u)(r, t) = \int_0^\infty J(r, r')\, u(r', t)\, dr' .$$

Then one can analyze the partial integro-differential equation in radial coordinates given by

$$\begin{aligned} \frac{\partial u}{\partial t}(r, t) &= -u(r, t) + F\left(a_{ee} \int_0^\infty J_e(r, r')\, u(r', t)\, dr' - a_{ei} \int_0^\infty J_i(r, r')\, v(r', t)\, dr' - \theta_e\right) \\ \tau\, \frac{\partial v}{\partial t}(r, t) &= -v(r, t) + F\left(a_{ie} \int_0^\infty J_e(r, r')\, u(r', t)\, dr' - a_{ii} \int_0^\infty J_i(r, r')\, v(r', t)\, dr' - \theta_i\right) . \end{aligned} \tag{B.4}$$

APPENDIX C

THE BOUNDARY VALUE PROBLEMS

This appendix is to write the boundary value problems that were numerically solved to create Figures 25–29. To write equations more succinctly, since each piece is solved simultaneously, we can normalize the periods of each piece so that the trajectory starts at 0 ($u_i(0)$ and $v_i(0)$) and ends at ($u_i(1)$ and $v_i(1)$) and solve for the periods $p_1, \ldots, p_5$.

We write the boundary value problem with three columns: The first contains the piecewise dynamics; the second column gives a corresponding boundary condition; and the third column is a description of the condition: Continuity is abbreviated to '*cty.*' and switching manifold is abbreviated to '*s.m.*' .

C.1 FIGURE 25

To produce the lower, right three panels of Fig. 25, we solved a 15 dimensional boundary value problem: 2 dimensions for the each of the five pieces; 5 dimensions to obtain the five periods in each region. We label the solution pieces by (u_i, v_i) for i going from 1 to 5 with counterclockwise orientation in the phase plane.

$$
\begin{aligned}
u_1' &= p_1\,(-u_1+1) & u_1(0)\,(1-\tau) - c - d + \tau &= 0 & \alpha &= 0 \\
v_1' &= p_1\,(-v_1+1)/\tau & h(u_1(0), v_1(0)) &= 0 & s.m. & \\
p_1' &= 0 & g(u_1(1), v_1(1)) &= 0 & s.m. & \\
u_2' &= p_2\,(-u2) & u_1(1) - u_2(0) &= 0 & cty. & \\
v_2' &= p_2\,(-v2+1)/\tau & v_1(1) - v_2(0) &= 0 & cty. & \\
p_2' &= 0 & h(u_2(1), v_2(1)) &= 0 & s.m. & \\
u_3' &= p_3\,(-u_3) & u_3(1) - u_3(0) &= 0 & cty. & \\
v_3' &= p_3\,(-v_3)/\tau & v_3(1) - v_3(0) &= 0 & cty. & \\
p_3' &= 0 & g(u_3(1), v_3(1)) &= 0 & s.m. & \\
u_4' &= p_4\,(-u_4+1) & u_3(1) - u_4(0) &= 0 & cty. & \\
v_4' &= p_4\,(-v_4)/\tau & v_3(1) - v_4(0) &= 0 & cty. & \\
p_4' &= 0 & h(u_4(1), v_4(1)) &= 0 & s.m. & \\
u_5' &= p_5\,(-u_5+1) & u_4(1) - u_5(0) &= 0 & cty. & \\
v_5' &= p_5\,(-v_5+1)/\tau & v_4(1) - v_5(0) &= 0 & cty. & \\
p_5' &= 0 & g(u_5(1), v_5(1)) &= 0 & s.m. &
\end{aligned}
$$

Note that $\alpha = 0$ is equivalent to starting where the sliding mode ends and the trajectory goes into the region R_2. One could continue piecing solutions together, adding dimensions to the system, but this increases numerical solving time only to converge to smaller and smaller pieces contained in a neighborhood of the focal crossing.

C.2 FIGURE 26

To obtain the limit cycles found in Fig. 26, we solve a 12 dimensional boundary value problem: 8 equations for the four pieces (u_i, v_i), starting from R_1 and going counterclockwise to R_4; an additional 4 equations for the periods of each:

$$
\begin{aligned}
u_1' &= p_1\,(-u_1+1) & u_1(1)-u_2(0)) &= 0 \quad cty.\\
v_1' &= p_1\,(-v_1+1)/\tau & v_1(1)-v_2(0) &= 0 \quad cty.\\
u_2' &= p_2\,(-u2) & v_2(1)-v_3(0) &= 0 \quad cty.\\
v_2' &= p_2\,(-v2+1)/\tau & u_2(1)-u_3(0) &= 0 \quad cty.\\
p_2' &= 0 & g(u_2(1),v_2(1)) &= 0 \quad s.m.\\
u_3' &= p_3,(-u_3) & u_2(1)-u_3(0) &= 0 \quad cty.\\
v_3' &= p_3\,(-v_3)/\tau & v_2(1)-v_3(0) &= 0 \quad cty.\\
p_3' &= 0 & h(u_3(1),v_3(1)) &= 0 \quad s.m.\\
u_4' &= p_4\,(-u_4+1) & u_3(1)-u_4(0) &= 0 \quad cty.\\
v_4' &= p_4\,(-v_4)/\tau & v_3(1)-v_4(0) &= 0 \quad cty.\\
p_4' &= 0 & g(u_4(1),v_4(1)) &= 0 \quad s.m.
\end{aligned}
$$

C.3 FIGURE 27

The stable limit cycles found in Fig. 27 were obtained by solving the boundary value problem posed for the limit cycles found in Fig. 26 and letting $\tau = 0.595$ which is approximately the homoclinic bifurcation value for our usual parameters. The homoclinic, shown in Fig. 27A, is a continuation with respect to τ of the solution found using a BVP. There are three

pieces to be solved backward in time, starting from $(u_1(0), v_1(0)) \in \Sigma$ and numbering them *clockwise*. The initial condition is such that $g(u_1(0), v_1(0)) =$ and $\alpha = 0$ (which is when sliding ends and $f^{sl}_{1,4} = f_4$). The final condition is when the third piece hits the switching boundary, $h(u_3(1), v_3(1)) = 0$. We have a 9 dimensional system:

$$
\begin{aligned}
u_1' &= p_1\,(-u_1) & u_1(0) - a\,v_1(0)/\tau - 1 &= 0 & \alpha &= 0 \\
v_1' &= p_1\,(-v_1)/\tau & g(u_1(0), v_1(0)) &= 0 & s.m.& \\
p_1' &= 0 & h(u_1(1), v_1(1)) &= 0 & s.m.& \\
u_2' &= p_2\,(-u2) & u_1(1) - u_2(0) &= 0 & cty.& \\
v_2' &= p_2\,(-v2 + 1)/\tau & v_1(1) - v_2(0) &= 0 & cty.& \\
p_2' &= 0 & g(u_2(1), v_2(1)) &= 0 & s.m.& \\
u_3' &= p_3\,(-u_3 + 1) & u_2(1) - u_3(0) &= 0 & cty.& \\
v_3' &= p_3\,(-v_3 + 1)/\tau & v_2(1) - v_3(0) &= 0 & cty.& \\
p_3' &= 0 & h(u_3(1), v_3(1)) &= 0 & s.m.&
\end{aligned}
$$

To obtain the homoclinic, we follow the solution of this BVP with respect to τ till $(u_3, v_3(1))$ is close to $(d, 0)$. Hence the solution will go into the saddle point from the knee. Moreover, sliding is stable backward in time, so we fill in the sliding mode on the u-switching boundary.

Figure 27B shows the grazing solution evolving forward in time. The solution was obtained in two parts. We used the same BVP as above to obtain the curve from the knee to the grazing point. Then starting from the initial condition $(u, v) \in \Gamma$ such that $f^{sl}_{1,4}(u, v) = f_4(u, v)$, we numerically integrate forward in time, and "glue" this part to the solution of the BVP.

C.4 FIGURE 28

Figure 28A is the bifurcation diagram showing the behavior of the stable and unstable limit cycles. We solved three different boundary value problems in order to follow the maximal and minimal values of the limit cycle with respect to τ. The green curve was obtained

through numerical continuation of the BVP found in the Appendix (section C.2) . Similarly, the small light blue piece is a continuation of the unstable limit cycle found by solving the following BVP backward in time (Hence (u_i, v_i) run clockwise with increasing index):

$$
\begin{aligned}
u_1' &= p_1\,(-u_1) & u_1(0) - u_4(1) &= 0 \qquad cty.\\
v_1' &= p_1\,(-v_1)/\tau & v_1(0) - v_4(1) &= 0 \qquad cty.\\
p_1' &= 0 & h(u_1(1), v_1(1)) &= 0 \qquad s.m.\\
u_2' &= p_2\,(-u2) & u_1(1) - u_2(0) &= 0 \qquad cty.\\
v_2' &= p_2\,(-v2+1)/\tau & v_1(1) - v_2(0) &= 0 \qquad cty.\\
p_2' &= 0 & g(u_2(1), v_2(1)) &= 0 \qquad s.m.\\
u_3' &= p_3\,(-u_3+1) & u_2(1) - u_3(0) &= 0 \qquad cty.\\
v_3' &= p_3\,(-v_3+1)/\tau & v_2(1) - v_3(0) &= 0 \qquad cty.\\
p_3' &= 0 & h(u_3(1), v_3(1)) &= 0 \qquad s.m.\\
u_4' &= p_4\,(-u_4+1) & u_3(1) - u_4(0) &= 0 \qquad cty.\\
v_4' &= p_4\,(-v_4)/\tau & v_3(1) - v_4(0) &= 0 \qquad cty.\\
p_4' &= 0 & g(u_4(1), v_4(1)) &= 0 \qquad s.m.
\end{aligned}
$$

The dark blue line was obtained by continuing the unstable limit cycle with a sliding mode. The BVP is essentially the same except for the small sliding piece:

$$
\begin{aligned}
u_1' &= p_1\,(-u_1) & u_1(0) - u_5(1) &= 0 \qquad cty.\\
v_1 &= (u_1 - d)/c & v_1(0) - v_5(1) &= 0 \quad cty.\\
p_1' &= 0 & u_1(1) - a\,v_1(1)/\tau - 1 &= 0 \qquad \alpha = 0\\
u_2' &= p_2\,(-u2) & u_1(1) - u_2(0) &= 0 \qquad cty.\\
v_2' &= p_2\,(-v2+1)/\tau & v_1(1) - v_2(0) &= 0 \qquad cty.\\
p_2' &= 0 & g(u_2(1), v_2(1)) &= 0 \qquad s.m.\\
u_3' &= p_3\,(-u_3+1) & u_2(1) - u_3(0) &= 0 \qquad cty.\\
v_3' &= p_3\,(-v_3+1)/\tau & v_2(1) - v_3(0) &= 0 \qquad cty.
\end{aligned}
$$

$$
\begin{aligned}
p_3' &= 0 & h(u_3(1), v_3(1)) &= 0 \quad s.m. \\
u_4' &= p_4\,(-u_4 + 1) & u_3(1) - u_4(0) &= 0 \quad cty. \\
v_4' &= p_4\,(-v_4)/\tau & v_3(1) - v_4(0) &= 0 \quad cty. \\
p_4' &= 0 & g(u_4(1), v_4(1)) &= 0 \quad s.m. \\
u_5' &= p_5\,(-u_4 + 1) & u_4(1) - u_5(0) &= 0 \quad cty. \\
v_5' &= p_5\,(-v_4)/\tau & v_4(1) - v_5(0) &= 0 \quad cty. \\
p_5' &= 0 & g(u_5(1), v_5(1)) &= 0 \quad s.m.
\end{aligned}
$$

C.5 FIGURE 29

Figure 29 shows the saddle-node on an invariant circle (SNIC) bifurcation. To produce panel C, we solved the BVP found in Appendix C.2 for the stable limit cycle shown in blue. We followed the solution with respect to b, till b was close to zero. The corresponding solution gives us the trajectory found in Fig. 29B which is a good approximation for the SNIC bifurcation. Note that both pseudo heteroclinics found in Fig. 29A, have infinite periods. The one along $\{v = 0,\ 0 < u < b\}$ is invariant and decays to zero. The other was produced by numerical integration.

BIBLIOGRAPHY

[1] Amari, Shun-ichi. "Dynamics of pattern formation in lateral-inhibition type neural fields." Biological cybernetics 27.2 (1977): 77-87.

[2] Beer, Randall D. "On the dynamics of small continuous-time recurrent neural networks." Adaptive Behavior 3.4 (1995): 469-509.

[3] Bressloff, Paul C. "Waves in neural media." Lecture Notes on Mathematical Modelling in the Life Sciences (Springer, New York, 2014) (2014).

[4] Challenger, Joseph D., Raffaella Burioni, and Duccio Fanelli. "Turing-like instabilities from a limit cycle." Physical Review E 92.2 (2015): 022818.

[5] Chagnac-Amitai, Y., and B. W. Connors. "Horizontal spread of synchronized activity in neocortex and its control by GABA-mediated inhibition." Journal of Neurophysiology 61.4 (1989): 747-758.

[6] Chervin, R. D., P. A. Pierce, and B. W. Connors. "Periodicity and directionality in the propagation of epileptiform discharges across neocortex." Journal of Neurophysiology 60.5 (1988): 1695-1713.

[7] Coombes, Stephen, et al. Neural Fields. Springer Berlin Heidelberg, 2014.

[8] Coombes, Stephen, Ruediger Thul, and Kyle CA Wedgwood. "Nonsmooth dynamics in spiking neuron models." Physica D: Nonlinear Phenomena 241.22 (2012): 2042-2057.

[9] Coombes, Stephen. "Waves, bumps, and patterns in neural field theories." Biological cybernetics 93.2 (2005): 91-108.

[10] Coombes, S., and P. C. Bressloff. "Saltatory waves in the spike-diffuse-spike model of active dendritic spines." Physical review letters 91.2 (2003): 028102.

[11] Crawford, John David. "Normal forms for driven surface waves: boundary conditions, symmetry, and genericity." Physica D: Nonlinear Phenomena 52.2-3 (1991): 429-457.

[12] Cross, Mark C., and Pierre C. Hohenberg. "Pattern formation outside of equilibrium." Reviews of modern physics 65.3 (1993): 851.

[13] Di Bernardo, Mario, et al. "Bifurcations in nonsmooth dynamical systems." SIAM review 50.4 (2008): 629-701.

[14] Di Bernardo, Mario, et al. Piecewise-smooth dynamical systems: theory and applications. Vol. 163. Springer Science & Business Media, 2008.

[15] Di Bernardo, M., C. J. Budd, and A. R. Champneys. "Normal form maps for grazing bifurcations in n-dimensional piecewise-smooth dynamical systems." Physica D: Nonlinear Phenomena 160.3 (2001): 222-254.

[16] Donoghue, John P., et al. "Neural discharge and local field potential oscillations in primate motor cortex during voluntary movements." Journal of neurophysiology 79.1 (1998): 159-173.

[17] Ermentrout, G. Bard, and David H. Terman. Mathematical foundations of neuroscience. Vol. 35. Springer Science & Business Media, 2010.

[18] Ermentrout, Bard. Simulating, analyzing, and animating dynamical systems: a guide to XPPAUT for researchers and students. Society for Industrial and Applied Mathematics, 2002.

[19] Ermentrout, Bard. "Neural networks as spatio-temporal pattern-forming systems." Reports on progress in physics 61.4 (1998): 353.

[20] Ermentrout, G. B. "Asymptotic behavior of stationary homogeneous neuronal nets." Competition and cooperation in neural nets. Springer Berlin Heidelberg, 1982. 57-70.

[21] Ermentrout, G. Bard, and Jack D. Cowan. "A mathematical theory of visual hallucination patterns." Biological cybernetics 34.3 (1979): 137-150.

[22] Fife, Paul C., and J. Bryce McLeod. "The approach of solutions of nonlinear diffusion equations to travelling front solutions." Archive for Rational Mechanics and Analysis 65.4 (1977): 335-361.

[23] Aleksei Fedorovich Filippov and Felix Medland Arscott. Differential Equations with Discontinuous Righthand Sides: Control Systems, Vol. 18, Springer, 1988.

[24] FitzHugh, Richard. "Impulses and physiological states in theoretical models of nerve membrane." Biophysical journal 1.6 (1961): 445-466.

[25] Folias, Stefanos E. "Nonlinear analysis of breathing pulses in a synaptically coupled neural network." SIAM Journal on Applied Dynamical Systems 10.2 (2011): 744-787.

[26] Folias, Stefanos E., and Paul C. Bressloff. "Stimulus-locked traveling waves and breathers in an excitatory neural network." SIAM journal on Applied Mathematics 65.6 (2005): 2067-2092.

[27] Giannakopoulos, Fotios, and Karin Pliete. "Planar systems of piecewise linear differential equations with a line of discontinuity." Nonlinearity 14.6 (2001): 1611.

[28] Ginzburg, Iris, and Haim Sompolinsky. "Theory of correlations in stochastic neural networks." Physical review E 50.4 (1994): 3171.

[29] Golomb, David, and Yael Amitai. "Propagating neuronal discharges in neocortical slices: computational and experimental study." Journal of neurophysiology 78.3 (1997): 1199-1211.

[30] Golomb, David, and G. Bard Ermentrout. "Continuous and lurching traveling pulses in neuronal networks with delay and spatially decaying connectivity." Proceedings of the National Academy of Sciences 96.23 (1999): 13480-13485.

[31] Han, Maoan, and Weinian Zhang. "On Hopf bifurcation in non-smooth planar systems." Journal of Differential Equations 248.9 (2010): 2399-2416.

[32] Harris, Jeremy, Rehman Ali, and Bard Ermentrout. "Pattern formation in oscillatory media without lateral inhibition." Physical Review E 94.1 (2016): 012412.

[33] Harris, Jeremy, and Bard Ermentrout. "Bifurcations in the Wilson–Cowan equations with nonsmooth firing rate." SIAM Journal on Applied Dynamical Systems 14.1 (2015): 43-72.

[34] Heitmann, Stewart, Tjeerd Boonstra, and Michael Breakspear. "A dendritic mechanism for decoding traveling waves: principles and applications to motor cortex." PLoS Comput Biol 9.10 (2013): e1003260.

[35] Heitmann, Stewart, Pulin Gong, and Michael Breakspear. "A computational role for bistability and traveling waves in motor cortex." Frontiers in computational neuroscience 6 (2012): 67.

[36] Hopfield, John J. "Neurons with graded response have collective computational properties like those of two-state neurons." Proceedings of the national academy of sciences 81.10 (1984): 3088-3092.

[37] Hoyle, Rebecca B. Pattern formation: an introduction to methods. Cambridge University Press, 2006.

[38] Huang, Xiaoying, et al. "Spiral waves in disinhibited mammalian neocortex." Journal of Neuroscience 24.44 (2004): 9897-9902.

[39] Jeffrey, Mike R. "Hidden dynamics in models of discontinuity and switching." Physica D: Nonlinear Phenomena 273 (2014): 34-45.

[40] Jeffrey, Mike R., and S. J. Hogan. "The geometry of generic sliding bifurcations." SIAM review 53.3 (2011): 505-525.

[41] Keane, Adam, and Pulin Gong. "Propagating waves can explain irregular neural dynamics." Journal of Neuroscience 35.4 (2015): 1591-1605.

[42] Kleinfeld, D., et al. "Dynamics of propagating waves in the olfactory network of a terrestrial mollusk: an electrical and optical study." Journal of Neurophysiology 72.3 (1994): 1402-1419.

[43] Kramer, Mark A., and Sydney S. Cash. "Epilepsy as a disorder of cortical network organization." The Neuroscientist 18.4 (2012): 360-372.

[44] K*ü*pper, Tassilo. Generalized Hopf bifurcation for non-smooth planar dynamical systems: the corner case NORTHEAST. MATH. J, 17 (2001), pp. 379382.

[45] Kuramoto, Yoshiki. "Diffusion-induced chaos in reaction systems." Progress of Theoretical Physics Supplement 64 (1978): 346-367.

[46] Kuznetsov, Yu A., S. Rinaldi, and Alessandra Gragnani. "One-parameter bifurcations in planar Filippov systems." International Journal of Bifurcation and chaos 13.08 (2003): 2157-2188.

[47] Leine, Remco, and Henk Nijmeijer. Dynamics and bifurcations of non-smooth mechanical systems. Vol. 18. Springer Science & Business Media, 2013.

[48] Levy, Robert B., and Alex D. Reyes. "Spatial profile of excitatory and inhibitory synaptic connectivity in mouse primary auditory cortex." Journal of Neuroscience 32.16 (2012): 5609-5619.

[49] Luczak, Artur, et al. "Sequential structure of neocortical spontaneous activity in vivo." Proceedings of the National Academy of Sciences 104.1 (2007): 347-352.

[50] Mathewson, Kyle E., et al. "Making waves in the stream of consciousness: entraining oscillations in EEG alpha and fluctuations in visual awareness with rhythmic visual stimulation." Journal of cognitive neuroscience 24.12 (2012): 2321-2333.

[51] McKean, Henry P. "Nagumo's equation." Advances in mathematics 4.3 (1970): 209-223.

[52] Michalareas, Georgios, et al. "Alpha-beta and gamma rhythms subserve feedback and feedforward influences among human visual cortical areas." Neuron 89.2 (2016): 384-397.

[53] Muller, Lyle, et al. "Rotating waves during human sleep spindles organize global patterns of activity that repeat precisely through the night." eLife 5 (2016): e17267.

[54] Muller, Lyle, et al. "The stimulus-evoked population response in visual cortex of awake monkey is a propagating wave." Nature communications 5 (2014).

[55] Murray, James D. Mathematical Biology. II Spatial Models and Biomedical Applications Interdisciplinary Applied Mathematics V. 18. Springer-Verlag New York Incorporated, 2001.

[56] Nagumo, Jinichi, Suguru Arimoto, and Shuji Yoshizawa. "An active pulse transmission line simulating nerve axon." Proceedings of the IRE 50.10 (1962): 2061-2070.

[57] Ozeki, Hirofumi, et al. "Inhibitory stabilization of the cortical network underlies visual surround suppression." Neuron 62.4 (2009): 578-592.

[58] Pinto, David J., and G. Bard Ermentrout. "Spatially structured activity in synaptically coupled neuronal networks: I. Traveling fronts and pulses." SIAM journal on Applied Mathematics 62.1 (2001): 206-225.

[59] Pinto, David J., et al. "Initiation, propagation, and termination of epileptiform activity in rodent neocortex in vitro involve distinct mechanisms." Journal of Neuroscience 25.36 (2005): 8131-8140.

[60] Rotstein, Horacio G., Stephen Coombes, and Ana Maria Gheorghe. "Canard-like explosion of limit cycles in two-dimensional piecewise-linear models of FitzHughNagumo type." SIAM Journal on Applied Dynamical Systems 11.1 (2012): 135-180.

[61] Rubino, Doug, Kay A. Robbins, and Nicholas G. Hatsopoulos. "Propagating waves mediate information transfer in the motor cortex." Nature neuroscience 9.12 (2006): 1549-1557.

[62] Rubino, Doug, Kay A. Robbins, and Nicholas G. Hatsopoulos. "Propagating waves mediate information transfer in the motor cortex." Nature neuroscience 9.12 (2006): 1549-1557.

[63] Rule, Michael, Matthew Stoffregen, and Bard Ermentrout. "A model for the origin and properties of flicker-induced geometric phosphenes." PLoS Comput Biol 7.9 (2011): e1002158.

[64] Shu, Yousheng, Andrea Hasenstaub, and David A. McCormick. "Turning on and off recurrent balanced cortical activity." Nature 423.6937 (2003): 288-293.

[65] Silber, Mary, Chad M. Topaz, and Anne C. Skeldon. "Two-frequency forced Faraday waves: weakly damped modes and pattern selection." Physica D: nonlinear phenomena 143.1 (2000): 205-225.

[66] Silber, Mary, and Edgar Knobloch. "Hopf bifurcation on a square lattice." Nonlinearity 4.4 (1991): 1063.

[67] Steyn-Ross, Moira L., D. Alistair Steyn-Ross, and James W. Sleigh. "Interacting Turing-Hopf instabilities drive symmetry-breaking transitions in a mean-field model of the cortex: a mechanism for the slow oscillation." Physical Review X 3.2 (2013): 021005.

[68] Takahashi, Kazutaka, et al. "Propagating waves in human motor cortex." Frontiers in human neuroscience 5 (2011): 40.

[69] Tonnelier, Arnaud. "The McKean's Caricature of the Fitzhugh–Nagumo Model I. The Space-Clamped System." SIAM Journal on Applied Mathematics 63.2 (2003): 459-484.

[70] Tonnelier, Arnaud. "McKean caricature of the FitzHugh-Nagumo model: Traveling pulses in a discrete diffusive medium." Physical Review E 67.3 (2003): 036105.

[71] Traub, R. D., J. G. Jefferys, and Richard Miles. "Analysis of the propagation of disinhibition-induced after-discharges along the guinea-pig hippocampal slice in vitro." The Journal of Physiology 472 (1993): 267.

[72] Trevelyan, Andrew J., et al. "Modular propagation of epileptiform activity: evidence for an inhibitory veto in neocortex." Journal of Neuroscience 26.48 (2006): 12447-12455.

[73] Tsodyks, Misha V., and Terrance Sejnowski. "Rapid state switching in balanced cortical network models." Network: Computation in Neural Systems 6.2 (1995): 111-124.

[74] Tsodyks, Misha V., et al. "Paradoxical effects of external modulation of inhibitory interneurons." Journal of neuroscience 17.11 (1997): 4382-4388.

[75] Wilent, W. Bryan, and Diego Contreras. "Synaptic responses to whisker deflections in rat barrel cortex as a function of cortical layer and stimulus intensity." Journal of Neuroscience 24.16 (2004): 3985-3998.

[76] Wilson, Hugh R., and Jack D. Cowan. "Excitatory and inhibitory interactions in localized populations of model neurons." Biophysical journal 12.1 (1972): 1-24.

[77] Wu, Jian-Young, Xiaoying Huang, and Chuan Zhang. "Propagating waves of activity in the neocortex: what they are, what they do." The Neuroscientist 14.5 (2008): 487-502.

[78] Yang, Lingfa, Anatol M. Zhabotinsky, and Irving R. Epstein. "Stable squares and other oscillatory Turing patterns in a reaction-diffusion model." Physical review letters 92.19 (2004): 198303.

[79] Zanos, Theodoros P., et al. "A sensorimotor role for traveling waves in primate visual cortex." Neuron 85.3 (2015): 615-627.

[80] Zhu, J. Julius, and Barry W. Connors. "Intrinsic firing patterns and whisker-evoked synaptic responses of neurons in the rat barrel cortex." Journal of neurophysiology 81.3 (1999): 1171-1183.

[81] Zou, Yongkui, and Tassilo Küpper. "Generalized Hopf bifurcation emanated from a corner for piecewise smooth planar systems." Nonlinear Analysis: Theory, Methods & Applications 62.1 (2005): 1-17.